Electrostatically Induced Carbon Nanotube Alignment for Polymer Composite Applications

by

Wesley Aaron Chapkin

A dissertation submitted in partial fulfillment
of the requirements for the degree of
Doctor of Philosophy
(Materials Science and Engineering)
in the University of Michigan
2017

Doctoral Committee:

Professor Alan I. Taub, Chair
Professor John Kieffer
Professor Wei Lu
Professor Michael Thouless

DEDICATION

To My Family,
Who Give Me the Strength to Succeed
(Or More Accurately, to Fail and Try Again)

ACKNOWLEDGEMENTS

In terms of the people who were invaluable to this research during my time at the University of Michigan, there are several individuals and groups whom I would like to acknowledge and thank for their guidance, wisdom, and aid.

It of course starts at the top with Prof. Taub for even giving me the opportunity. From the months "in the library" before there was even a room labeled *Taub Group*, to soldering wires on the one lab bench we had, to defending the original research on which we co-conspired in front of a group of intellectual peers, Prof. Taub has been there to mentor me on every step of the way. To keeping me on track when all seemed lost and taking me down a few pegs when I thought I knew everything, I could never seem to get more than half a step ahead… if even that. His advice (if not always heeded) was instrumental in my reaching this point both in the research projects collated below as well as in my development as a researcher. (But perhaps what I'm the most thankful for… is that the Acknowledgements section doesn't need to be written like a manuscript.)

I am also grateful to my committee—Prof. John Kieffer, Prof. Wei Lu, and Prof. Michael Thouless—for their insight and direction. For the early polarized Raman work, I want to especially thank Prof. Kieffer for the use of their custom setup. I would also like to thank Prof. Joerg Lahann for the extensive use of the WITec Raman spectrometer. Without which, much of the next hundred or so pages would be blank.

For experimental assistance, I am indebted to Dr. Michael Aldridge (formerly of the Kieffer Group) for patiently toiling in the dark with me on samples that never seemed to work… until they finally did. Helpful initial discussions with Brian Rook (Drzal Group at Michigan State University) on epoxy systems and CNT dispersion got the project moving. Ryan Hall's (Larson Group) assistance in conducting the zero-shear viscosity measurements was much appreciated and super timesaving. Jill Wenderott (Green Group) was an AFM nonpareil on our always enjoyable nanotube hunting expeditions. I am obliged to Dr. Mahesh Ganesan and Nina Gasbarro (formerly and currently of the Solomon Group, respectively) for aiding in the dynamic

light scattering measurements that didn't quite come to fruition but that I believe are, with the right temperament, still possible for quantifying the state of CNT dispersion within an optically transparent polymer. I would like to thank Keith McIntyre for input on machined and 3D printed parts and for training me (sometimes more than once) on the Van Vlack equipment.

Within the Taub group, many thanks are owed to Dr. Dan "The Gurney" McNerny for tolerating all my lab shenanigans. Oh, and for other marginally helpful things like brainstorming ideas and troubleshooting experimental problems with me; proofreading thesis proposal documents, manuscripts, and conference and symposium abstracts; approving my brilliantly obnoxious order requests (with a smile); and for letting me have the stool. Occasionally. I have only praise for Avi Bregman for the visually resplendent COMSOL models seen in Chapter 5, especially the one I made him remake about three dozen times. And also for Queen Mondays. And Wednesdays. And Friday afternoons. And our widely popular, always superlative joke board. I need also thank Yipeng He for early collaboration that was instrumental in developing the real-time polarized Raman technique demonstrated in this thesis. I give thanks (even though she most graciously didn't want it) to Anita Luong for her least squares code that she generously allowed me to apply to the orientation parameter calculations (Chapter 2) as well as the length best-fits (Chapter 4). I owe a fair bit of gratitude to Connor Saukas and Alissa Recker for being wonderfully helpful and ingeniously imaginative undergraduate researchers. I look forward to reading their doctoral dissertations in about four years' time.

And to those misguided souls working on metals projects—Tasha Mangaldas, Erika Salem, Maya Nath, Caleb Reese, Dr. Xun Liu, Pritam Das, and Justin Eszlinger—I can only say it's never too late to switch over to the light. But until then, thank you all for the moral and emotional support so freely given that I required to overcome all those dark days… because sundown before five in the winters is just absurd. And finally, I absolutely need to express thanks to Ellen Kampf, the unsung hero of the group without whom nothing would have ever happened on time… or probably at all after LIFT got underway.

Thanks to all for making the work presented herein possible.

TABLE OF CONTENTS

LIST OF FIGURES

LIST OF TABLES

LIST OF ACRONYMS AND SYMBOLS

AFM = atomic force microscopy
CCM = concentric cylinder model
CFRP = carbon fiber reinforced plastic
CNT = carbon nanotube
D-band = "disordered" CNT spectral feature in Raman spectroscopy
DLS = dynamic light scattering
D_R = rotational diffusion coefficient
D_{SE} = translational diffusion coefficient for a particle exhibiting Stokes-Einstein behavior
d_T = mesh entanglement length
D_t = translational diffusion coefficient
G-band = "graphitic" CNT spectral feature in Raman spectroscopy
HH = horizontal (parallel) scattering geometry for polarized Raman spectroscopy
HWHM = half width at half maximum
I_{norm} = normalized polarized Raman intensity of the CNT G-band, Eq. (2.1)
k_B = Boltzmann constant ($\approx 1.39 \cdot 10^{-23}$ J/K)
m-SWCNT = metallic single-walled carbon nanotube
mPDA = *m*-Phenylenediamine
PBMA = poly(*n*-butyl methacrylate)
PDF = probability distribution function
PL = photoluminescence
PMMA = poly(methyl methacrylate)
RBM = radial breathing mode of CNTs in Raman spectroscopy
R_g = radius of gyration
S = Herman's orientation parameter, Eq. (2.7)
s-SWCNT = semiconducting single-walled carbon nanotube
SEM = scanning electron microscopy
TEM = transmission electron microscopy
T_g = glass transition temperature
U_E = electrostatic potential energy
VV = vertical (perpendicular) scattering geometry for polarized Raman spectroscopy
WAXD = wide-angle x-ray diffraction
XRD = x-ray diffraction
ζ_R = rotational friction coefficient
η_0 = (zero) shear (or dynamic) viscosity
η_L = local viscosity
τ_E = electrostatic-induced torque
Φ_c = percolation threshold

ABSTRACT

We have developed a non-invasive technique utilizing polarized Raman spectroscopy to measure changes in carbon nanotube (CNT) alignment *in situ* and in real time in a polymer matrix. With this technique, we have confirmed the prediction of faster alignment for CNTs in higher electric fields. Real-time polarized Raman spectroscopy also allows us to demonstrate the loss of CNT alignment that occurs after the electric field is removed, which reveals the need for fast polymerization steps or the continued application of the aligning force during polymerization to lock in CNT alignment.

Through a study on the effect of polymer viscosity on the rate of CNT alignment, we have determined that shear viscosity serves as the controlling mechanism for CNT rotation. This finding matches literature modeling of rigid rod mobility in a polymer melt and demonstrates that the rotational mobility of CNTs can be explained by a continuum model even though the diameters of single-walled CNTs are ~1–2 nm. The viscosity dependence indicates that the manipulation of temperature (and indirectly viscosity) will have a direct effect on the rate of CNT alignment, which could prove useful in expediting the manufacturing of CNT-reinforced composites cured at elevated temperatures.

Using real-time polarized Raman spectroscopy, we also demonstrate that electric fields of various strengths lead not only to different speeds of CNT rotation but also to different degrees of alignment. We hypothesize that this difference in achievable alignment results from discrete populations of nanotubes based on their length. The results are then explained by balancing the alignment energy for a given electric field strength with the randomizing thermal energy of the system. By studying the alignment dynamics of different CNT length distributions, we show that different degrees of alignment achieved as a function of the applied electric field strength are directly related to the square of the nanotube length. This finding matches an electrostatic potential energy model for CNT rotation.

Lastly, we investigate the effects of conductive carbon fibers on electrostatically induced alignment of CNTs within carbon fiber composites. The relative electric field strength throughout the composite is modeled using COMSOL Multiphysics. We show the ability to generate enhanced electric field gradients within the gaps between carbon fibers for various fiber orientations. Using polarized Raman spectroscopy, increased levels of CNT alignment are observed between carbon fiber tows, which is consistent with the modeled higher electric field strengths in these regions. These findings could potentially lead to the development of carbon fiber composites with CNT additions that selectively enhance the composite properties outside the carbon fiber interphase in the neat epoxy.

CHAPTER 1
MOTIVATION AND BACKGROUND

1.1 CNT Composite Property Variability

High-strength, low-weight composites continue to attract attention from a variety of industries that seek ever stronger and lighter products. Carbon fiber-reinforced polymer composites are an excellent alternative to traditional materials in this regard but often at increased cost [1,2]. A promising approach to improving the mechanical properties while limiting an increase in cost is the addition of nanoparticulate material to polymer composites. Due to the large theoretically predicted [3] and experimentally determined [4,5] elastic moduli of carbon nanotubes (CNTs), their incorporation into composite materials offers the potential for developing strong, lightweight alternatives to traditional materials. For example, small additions (< 1 wt%) of CNTs strongly affect the base mechanical properties of neat polymers [6–9]. Nevertheless, experimental results from different reports display a high degree of variability with respect to property enhancement [10], and this extends to systems of equivalent nanoparticle loading of CNTs produced by the same growth method. This variability is one factor limiting the applications of this material.

A variety of processing factors could conceivably contribute to the reported variability of CNT composite properties (Figure 1.1). Nanoparticle dispersion is one factor. Several studies have shown that the state of CNT dispersion will affect the resultant mechanical, electrical, and thermal properties of the composite [11,12]. The inhomogeneity of a poorly dispersed nanocomposite can adversely affect composite properties by forming stress concentration points [13], voids in the composite that form from the slippage of CNTs in micro-agglomerates [11], and by reducing the surface-area-to-volume ratio of the nanoparticle reinforcement. The high surface-area-to-volume ratio of well dispersed CNTs maximizes the total interfacial area. This is important to the resultant composite properties because the interface controls the load transfer from the matrix to the reinforcement.

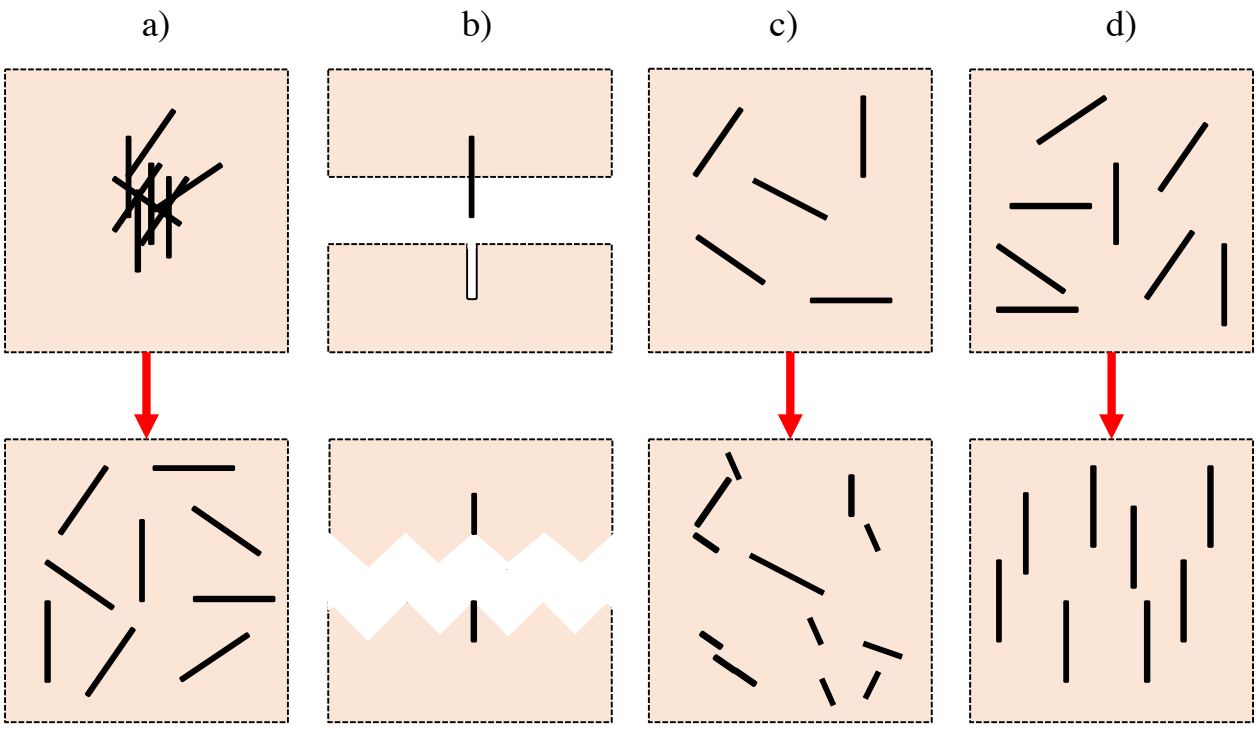

Figure 1.1 – Potential sources of composite property variability resulting from a) CNT dispersion, b) load transfer (CNT-matrix debonding and CNT fracture) c) CNT damage (length shortening from sonication) d) and CNT alignment.

The load transfer in composites is commonly analyzed by a shear lag model and extrapolated to macroscopic properties by a concentric cylinder model (CCM). Originally used for fiber composites, these models can also be applied to CNTs [14–17]. In shear lag, the stress is transferred from the matrix to a nanotube through a shear force at the interface. CCM depicts the matrix surrounding the nanotube as an interfacial zone (or interphase). The properties in the interphase are superior to the non-interacting polymer chains falling outside this zone [12] due to a decrease in polymer chain mobility [18,19]. The size of this interfacial region varies depending on the compatibility of the reinforcement with the matrix but may extend up to several hundred nanometers [20]. Ideally, CNTs are dispersed uniformly throughout the matrix at a concentration in which the CNT-polymer interfaces do not overlap but also in which none of the matrix exists outside this interfacial zone. In practical (and cost effective) terms, the elimination of overlap is achieved by reducing the CNT loading.

The load transfer at the CNT-polymer interface can also be altered by surface modification of CNTs. One example of this is through a process of polymer wrapping. Polymer wrapping typically uses amphiphilic molecules that adsorb onto the CNT surface, prevent flocculation of the nanotubes, and can increase the bonding between the CNTs and the matrix [21]. Although beneficial to the CNT-matrix interface, the adsorption of these molecules leads to insulating coatings that can adversely affect the composite electrical properties [22].

Another route for surface modification of CNTs is functionalizing the nanotube surface. Functionalization of CNTs can increase the bonding between the CNTs and the matrix and decrease the affinity between nanotubes, which prevents the reaggregation of CNTs and can lead to better dispersions. This results in increased load transfer between the polymer matrix and the nanoparticle reinforcement and can result in superior composite mechanical properties [23]. However, functionalization can damage the inherent strength of a CNT [24–26] as well as its intrinsic electronic structure [12,27,28] by disrupting the graphitic sp^2 carbon lattice of the CNT sidewalls. In fact, it has been demonstrated that as few as one to two vacancies in the CNT sidewall can reduce the observed failure stress of a nanotube up to ~26% [29].

The damage to the intrinsic structure of a CNT caused by surface modifications and other processing steps is an often-overlooked consequence in manufacturing composites. Dispersion processes such as extensive sonication have been shown to damage CNTs [30]. The average CNT length shortens with increasing sonication energy through a scission process (see Chapter 4). The length (aspect ratio) dependence of mechanical properties for fibers is well documented through the shear lag model. This dependence extends to CNTs where it has been shown that longer nanotubes result in superior properties [31–33]. As described by the shear lag model, the particle aspect ratio is important for the interfacial strength between the matrix and a CNT [34]. The strength of the interface determines the type of failure [17]; CNTs below a critical length lead to fiber pullout from interfacial debonding, and CNTs above this critical length will fracture.

Another potential source of variability in the mechanical properties of CNT-reinforced polymer composites may originate from the degree of nanotube alignment. Single-walled CNTs exhibit a large anisotropy in the longitudinal (typically hundreds of nanometers up to several centimeters) as compared to the radial direction (on the order of a few nanometers). As a result, the increase in properties of the composite occurs predominantly in the direction of the CNT longitudinal axis [35–37]. In systems without an external aligning force, a randomized CNT

direction is entropically favorable, and the increase in mechanical properties is diluted over all angles. In aligned specimens, every nanoparticle can contribute to the mechanical properties in the alignment direction. Layered polymer composites—in which thin, in-plane aligned layers can be stacked to macroscopic thicknesses—can therefore possess much greater strength and stiffness in one or two dimensions than their bulk, unaligned counterparts [38,39].

To create cost-effective, robust nanocomposites for load-bearing applications, an optimization of these factors is required at low nanoparticle loadings. This thesis focuses on the alignment process for CNTs and attempts to delineate the factors that control the degree and speed of CNT alignment within a polymer.

1.2 Methods for Effecting CNT Alignment in Polymers

The reorientation of CNTs in a polymer matrix can be induced by a number of methods including shear flow [40–48], magnetic fields [49–55], and electric fields [56–63]. The alignment of CNTs in a polymer by mechanical shearing methods has been demonstrated by the mechanical stretching of ductile thermoplastic films [40–43,48], melt spinning of CNT-polymer fibers [44,45], microtoming a CNT-resin composite into thin slices (thickness < 200 nm) [46], and inducing shear flow with a doktor blade [47]. The alignment of CNTs in polymer films, resins, and fibers via mechanical shear offers a wide range of uses in manufacturing. However, due to the rotational diffusivity of the particles, CNTs will unalign if the alignment force is not maintained as the composite structure sets [62]; this occurs during polymerization for a thermoset and cooling below the glass transition temperature (T_g) for a thermoplastic melt. For resins requiring thermal cures, this phenomenon represents a limitation for mechanical shear alignment methods such as extrusion.

The use of magnetic fields is another method that has been successfully employed to induce CNT alignment in a polymer. When placed in a magnetic field, CNTs will reorient into the magnetic field direction. This is due to the high anisotropy in their magnetic susceptibility [49]. Although alignment via magnetic fields has been demonstrated, it has proven impractical for pristine nanotubes due to their low magnetic susceptibility [64,65] and usually requires magnetic fields of ~10 T. Affixing ferromagnetic particles to the surface of CNTs has resulted in nanotube alignment at lower magnetic field strengths [53], but this method involves additional processing steps that can alter the nanotube surface and affect the interface with the matrix.

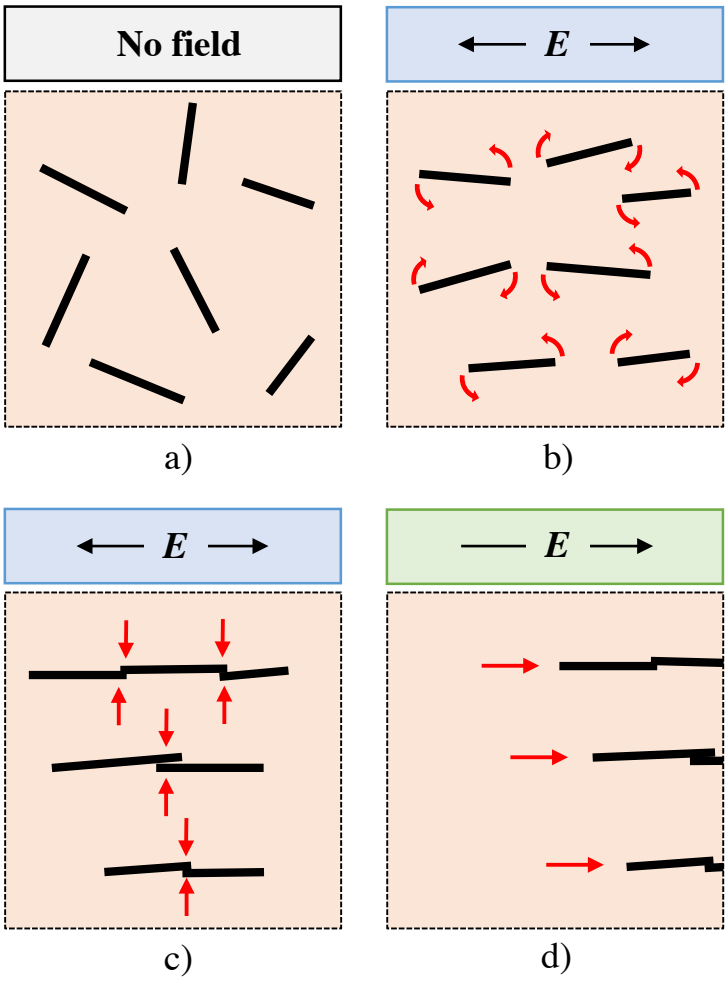

Figure 1.2 – Response of CNTs to an applied electric field. Starting from a) a dispersed and randomly oriented state, CNTs in an AC electric field will b) rotate to become parallel to the electric field direction and c) translate to create conductive networks. d) In a DC electric field, CNTs will then migrate toward the electrodes.

Electric fields have proven effective in aligning CNTs in both AC [56–62] and DC [60,61,63] and have the advantage of being applied continuously during a curing process. The response of a CNT to an applied electric field can be characterized by three concurrent events [66]: alignment, translation, and migration (shown in Figure 1.2). Alignment describes the orienting of a CNT with its long axis parallel to the electric field direction. This is due to the highly anisotropic electric polarizability of CNTs [61]. In response to an applied electric field, a shift in charge occurs on the tube surface that results in the formation of a dipole at the CNT ends. The electric field then induces a torque that forces the CNT to align parallel to the electric field direction [61,67]. For a CNT to reorient in response to an electric field, the alignment

energy (U_E) must exceed the thermal energy of the system ($U_E > 2k_BT$) [68–72]. This is validated by the observation of a minimum electric field strength for detectable alignment of both multi-walled (46.5 V/cm) [73] and single-walled CNTs (150–163 V/cm) [56,62].

As CNT alignment occurs in the applied electric field direction, Coulombic interaction between the nanotubes leads to simultaneous translation [66]. Translation describes the attraction of CNTs in a head-to-tail fashion to create dynamic percolation paths that bridge the electrodes. This process is commonly referred to as CNT networking, which creates conductive CNT filaments bridging an otherwise insulating matrix and has been observed at concentrations as low as 0.002 wt% [74]. The third phenomenon observed for CNTs in an applied electric field is migration, which is limited to DC fields. Migration describes the movement of CNTs to one or both electrodes depending on the overall charge of the tube. Due to the electrostatic forces and relative distances involved, alignment and translation have been predicted to occur on similar timescales while migration is at least one order of magnitude slower [63].

Precise control of nanotube alignment is an important factor in creating nanocomposites with enhanced electrical and mechanical properties. The study of CNT alignment induced by an electric field has been modeled [63,67] and experimentally analyzed [75,76] as a function of electric field strength and frequency. The work presented herein attempts to further explore electrostatically induced alignment of CNTs in a polymer for its application to the manufacturing of structural composites.

1.3 Techniques for Characterizing CNT Alignment

To more fully understand electric field-driven alignment, the development of non-destructive techniques for probing the alignment process of a CNT *in situ* within a polymer matrix is paramount. A variety of experimental techniques have been used to assess the state of CNT alignment. Microscopy—including optical microscopy [56], scanning electron microscopy (SEM) [70,77,78], transmission electron microscopy (TEM) [41,46], and atomic force microscopy (AFM) [70,79]—has been used extensively to study nanotube alignment. However, all these techniques have limitations in analyzing the alignment of CNTs imbedded in polymers. Because of the diffraction limit of visible light microscopes, the resolution using optical microscopy is on the order of hundreds of nanometers. This limits the study of CNTs with this

technique to nanotube bundles [56] that can result from poor dispersion or reagglomeration during the alignment process.

By using electrons instead of visible light, SEM techniques have increased resolution of nanostructures. Nonetheless, SEM is mostly a surface technique and analyses of CNT alignment have been limited to substrates [70,77] or fracture surfaces [78]. Furthermore, because many substrates and polymer thin films are electrically insulating, charging effects [77] can distort the dimensions of the imaged nanoparticles while sputter coating the surface with a conductive layer can blanket the desired features. AFM has a similar limitation as a mostly surface characterization technique, and atomically smooth substrates are typically required to resolve single-walled CNTs. However, newly developed subsurface imaging techniques [80] appear promising in studying CNTs imbedded in non-conductive materials.

Compared to SEM and AFM, TEM has the advantage of measuring diffracted electrons through thin, non-conductive specimens. With the capability of atomic-scale resolution, TEM imaging of the alignment of individual CNTs has been previously demonstrated [41,46]. With TEM, however, the uniformity of alignment throughout the sample comes into question based on the limitation in sample size. For the required nanoscale resolution to observe nanotube alignment, the scale of the images is small compared to the overall size of the sample. Thus, numerous images are required to ensure the findings are consistent, which can be a time-consuming process. Additionally, TEM sample prep may be destructive or misleading in terms of alignment as seen in the ability to induce post-processing reorientation of nanotubes in a polymer by microtoming thin TEM slices [46]. TEM itself is a destructive technique. Electron irradiation of sufficient energy ($\gtrsim$86 kV) has been shown to create defects in the walls of CNTs [81,82]. These defects resulting from knock-on collisions of the incident electrons can even lead to inter-wall bonding in multi-walled CNTs [83,84] and single-walled CNT bundles [85], altering the sp^2 lattice structure in the CNT walls. Extended exposure to high-energy electron beams can even amorphize CNT walls [81]. If care is taken to avoid the destructive effects of TEM and its sample prep, recently developed *in situ* techniques [86] may offer the possibility to image CNT alignment in real time.

Besides microscopy, x-ray diffraction (XRD) methods [41] including wide-angle x-ray diffraction (WAXD) [87,88] have been used to characterize CNT alignment. For a random orientational distribution of CNTs, a powder diffraction ring with uniform intensity with respect

to its azimuthal angle is expected; for aligned CNTs, the diffraction ring will show peak intensities at 0˚ and 180˚ degrees with respect to the alignment direction [41]. Because XRD measures the diffraction of x-rays from the (002) Bragg peak for the interlayer spacing of the graphitic walls [41], CNTs can be easily distinguished from amorphous polymers with these methods. This does, however, limit XRD analyses to multi-walled CNTs or single-walled CNT bundles [89].

In terms of studying the average alignment dynamics of CNTs within a polymer on statistically relevant scales, polarized spectroscopic techniques may prove the most useful. These techniques can be separated by the way the incident light interacts with the particles: emission, absorbance, or inelastic scattering. Light emission refers to particle fluorescence or photoluminescence (PL). By utilizing the anisotropy of CNT absorption and fluorescence, polarized PL spectroscopy has been used to characterize CNT alignment [77,90] on flat substrates. However, PL measurements are very sensitive to a nanotube's environment, and the signal intensity can be significantly reduced by a phenomenon called CNT quenching [91–93].

At the current level of technology, the bulk production of CNTs generates a mixture of metallic (m-SWCNT) and semiconducting (s-SWCNT) nanotubes, which are classified by the chiral angles of their roll-up vectors (Figure 1.3) and possess distinctive optical and electronic properties [94]. CNT quenching describes the absence of fluorescence in CNT bundles that is otherwise expected to occur in isolated semiconducting CNTs. For an isolated tube, incident light generates an exciton. The recombination of the electron-hole pair results in the emission of a photon. In the case of metallic nanotubes, holes generated from the incident light are filled by free electrons in a process of non-radiative recombination [94]. For small CNT agglomerates containing at least one metallic nanotube, the process of inter-tube exciton energy transfer occurs faster than recombination, and thus, the entire CNT bundle behaves like a metallic CNT in which the absence of a band gap precludes the production of excitons [92,95]. In addition to its sensitivity to bundling, the fluorescent intensity from CNTs can also be quenched by contact with a semiconducting substrate [90] or at a low pH where oxidation of the CNT walls can occur [96]. As a result, polarized PL spectroscopy is typically ineffective at characterizing CNT alignment except at low concentrations of well dispersed, non-interacting CNTs.

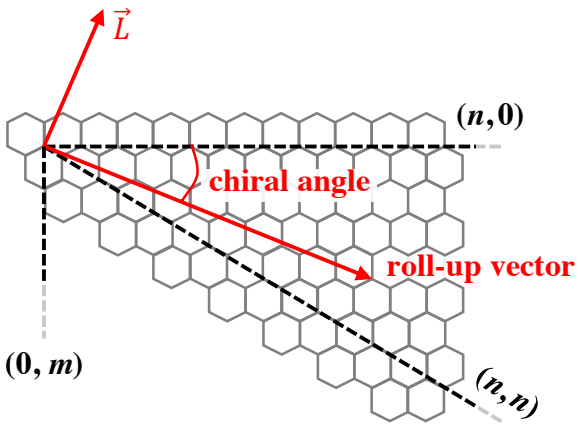

Figure 1.3 – CNT lattice designation from its (*n*, *m*) indices as determined by its chiral angle and roll-up vector. When *n*–*m* mod 3 = 0, the nanotube is metallic; otherwise, it will be semiconducting [97]. $\vec{L}$ denotes the length and direction of the nanotube's longitudinal axis. The length of the roll-up vector is the CNT circumference.

For all the disadvantages of the previously mentioned techniques, perhaps the greatest is that these measurements have heretofore been limited to end-state specimens, which we define as composites post-polymerization where (random or induced) CNT rotation has been arrested. In the search for a technique that can be used to assess CNT alignment dynamics, considerable information on the mechanism of electrostatically induced alignment is lost when measurements cannot be taken in real time. Therefore, it is imperative that a form of testing that meets the following requirements is used:

1. is non-destructive to the sample with no distortion to nanotube mobility,
2. has a CNT signal that is distinguishable from an insulating polymer matrix,
3. and has integration times for real-time measurements that are fast relative to the kinetics of alignment.

To determine the degree of alignment of CNTs in real time, several spectroscopic techniques have been successfully employed, including polarized absorbance (or transmittance) spectroscopy [76,98] and polarized Raman spectroscopy [40,44,45,50,51,56,99]. Similarly to PL measurements, polarized absorbance spectroscopy capitalizes on the anisotropy in absorbance (or linear dichroism) for a CNT, which is often considered a 1D material because of its high aspect ratio. The degree of light transmission has been demonstrated to increase as polarization is switched from parallel to perpendicular with respect to the CNT alignment direction in stretched films [40,42,48]. Using linear dichroism [98] and birefringence [75,76] measurements,

the electrostatically induced alignment of CNTs in solution has previously been measured *in situ* and in real time. These measurements give researchers insight into the timescale of CNT reorientation as the measured intensities taken parallel and perpendicular to the field direction show increases and decreases, respectively, during the application of an electric field. Despite its success in monitoring CNT reorientation in real time, absorbance spectroscopies are limited to highly transmitting media (water, organic solvents, etc.), which would therefore preclude these measurements in most structural polymers of interest.

1.4 Polarized Raman Spectroscopy of CNTs

A viable alternative to polarized absorbance spectroscopy, polarized Raman spectroscopy is often used to identify CNT alignment in polymer composites [40,44,45,50,51,56,99]. The signal strength of CNTs from Raman scattering is extraordinarily strong as seen in the ability to collect a spectrum from a single nanotube [100]. Because of this, Raman spectra collected from CNT-polymer composites show prominent CNT spectral features even at low CNT concentrations. In Raman spectroscopy, the inelastic scattering of light from phonons yields Raman shifts in energy. These Raman shifts are specific to chemical bonds and therefore give material information about a sample on the molecular scale. Commonly used to determine chemical composition, polarized Raman spectroscopy gives the added ability to take linear dichroic measurements while identifying the source of the scattering. This is a marked advantage over (non-resonant) absorbance measurements for which it is difficult to distinguish CNTs from other any other particles (such as impurities, polymer chains, etc.) exhibiting optical anisotropy. With polarized Raman spectroscopy, it can be said with certainty that specific spectral features originate solely from a CNT.

One example of this is the CNT G-band, which results from the in-plane oscillations of sp^2 carbon atoms and is observed in all graphitic structures. Although most characteristic CNT spectral features change proportionally with respect to the polarization angle (including the radial breathing mode (RBM) and disorder-induced D-band) [43], the G-band is most commonly used since it is typically the most prominent peak (Figure 1.4a). Using the ratio of orthogonally polarized incoming and scattered light (often denoted by G_{HH}/G_{VV} where H and V describe scattering geometries parallel and perpendicular to the alignment direction, respectively) [101–

103], the relative degree of alignment can be assessed via polarized Raman spectroscopy (Figure 1.4b).

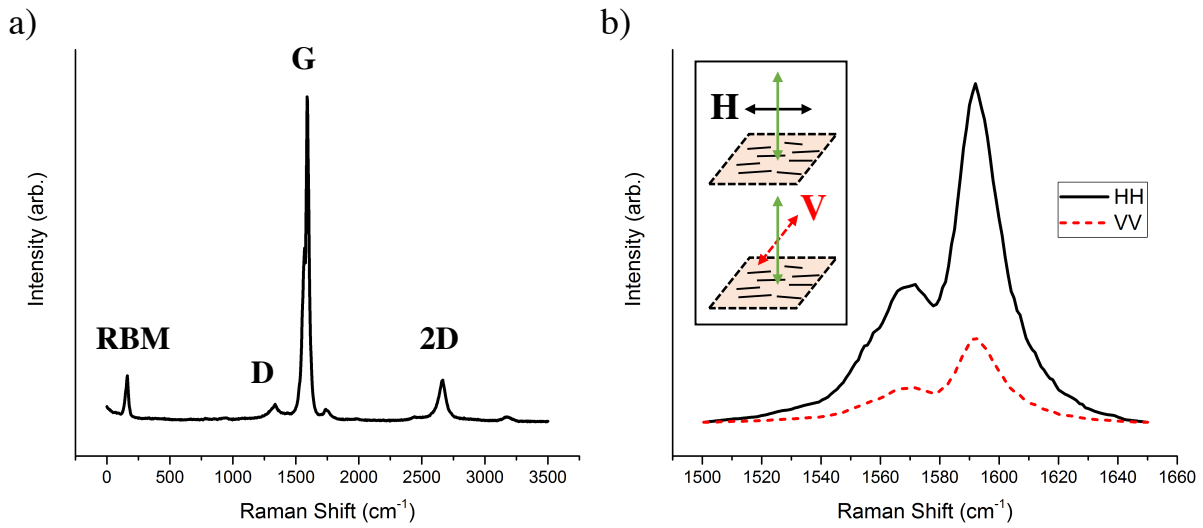

Figure 1.4 – a) A characteristic Raman spectrum for a carbon nanotube with several peaks of interest identified. b) The CNT G-band shown with polarizations parallel (HH) and perpendicular (VV) to the alignment direction. The ratio of the intensities of the G^+ peak (~1592 cm^{-1}) is used as an indication of the degree of CNT alignment. The inset shows the two polarization geometries with respect to the focal plane of the laser in the sample. The laser directions are denoted by the green arrows.

In addition to having the capacity to resolve CNT spectral features from the polymer matrix, Raman spectroscopy is also a non-destructive test capable of probing the CNT alignment process *in situ*. If localized heating from high laser powers focused on small excitation volumes is avoided as laid out by NIST guidelines [104], Raman scattering from the nanotubes will have a minimal effect on particle mobility. Furthermore, good signal-to-noise ratios for low concentrations of CNTs embedded in a polymer can be achieved for relatively short integration times (on the order of a few seconds) [62,105]. While this may not yet be fast enough to observe CNT rotation in low viscosity solutions [76,106], this technique should be well suited for the predicted timescales of alignment for CNTs in higher viscosity polymer mixtures [63]. Ergo, the work in this thesis sought to develop a polarized Raman spectroscopy technique that could be used to analyze the process of CNT alignment induced by an electric field in a thermoset polymer matrix.

1.5 Thesis Overview

Overall, the proposed study intends to investigate the alignment of carbon nanotubes within a polymer composite. Through real-time analyses of CNT-polymer systems under an imposed electric field, a more accurate understanding of the alignment process as well as the factors that affect it can be developed. This will also help to prevent potential misleading conclusions based on measurements of polymerized specimens that can obscure relevant information on the dynamics of alignment. These insights can then be applied to determine optimal processing conditions for CNT composites for engineering applications.

In Chapter 2, a technique of real-time polarized Raman spectroscopy capable of making CNT alignment measurements *in situ* within a polymer is introduced. The speed and degree of alignment is analyzed as a function of the applied electric field strength and compared to end-state measurements of CNT alignment from the literature. The loss of alignment resulting from Brownian motion upon removing the electric field is also shown. In Chapter 3, the viscosity dependence on the speed of CNT rotation is investigated. Results are compared to theoretical predictions of the rotational mobility of nanoscale rigid rods in polymers. In Chapter 4, the effects of CNT length on the degree and speed of alignment and randomization are investigated. Discrete levels of alignment are shown, and an electrostatic potential energy model is used to explain this as the alignment of different populations of CNTs based on their lengths. In Chapter 5, CNTs are electrostatically aligned within a carbon fiber composite. Using COMSOL modeling, gradients in the electric field strength near the conductive carbon fiber ends are expected. Within these regions of increased electric field strength, greater degrees of CNT alignment are shown. The implications of selectively aligning CNTs in specific regions of the composite for tailoring composite properties is discussed. A summary of the contributions of this thesis as well as ongoing work and potential future directions are laid out in Chapter 6.

CHAPTER 2
REAL-TIME, *IN SITU* POLARIZED RAMAN SPECTROSCOPY OF CARBON NANOTUBE ALIGNMENT

2.1 Chapter Synopsis

A technique has been developed utilizing polarized Raman spectroscopy to measure the alignment of carbon nanotubes *in situ* in a polymer matrix under an applied electric field. Previous studies of alignment have been restricted to optically transparent solvents or polymerized specimens that prevent accurate analyses of alignment dynamics in polymers. The effects of electric field strength on the degree of alignment and the time to achieve an aligned state are discussed. The use of *in situ*, real-time polarized Raman spectroscopy provides a non-invasive technique for assessing carbon nanotube alignment, which can assist in determining processing conditions to improve the mechanical and electrical properties of aligned nanocomposites.

2.2 Introduction

Due to the complex response of CNTs to an applied electric field, insights into the alignment process are limited by post-alignment characterization techniques. Information on the competing mechanisms of CNT rotation, translation, and migration as well as the effects of undergoing a thermally activated polymerization process (thermal gradients, increased particle mobility at elevated temperatures, etc.) is obscured in these end-state "snapshots". Therefore, the need to accurately probe these processes *in situ* and in real time is paramount. Polarized Raman spectroscopy appears to be a promising method for conducting these measurements non-destructively.

However, the characterization of CNT alignment in composites using polarized Raman spectroscopy measurements has heretofore been limited to specimens polymerized after alignment. The dearth of real-time data inhibits the development of an accurate model of the response of a CNT in a polymer to an electric field. To address these concerns, this chapter

describes the development of a polarized Raman spectroscopy technique to non-destructively observe the CNT alignment process *in situ* in structural polymers of commercial interest.

2.3 Experimental

2.3.1 Materials

Single-walled carbon nanotubes (AP-SWNT) (average diameter, d_{avg} = 1.4 nm and length, L = 1-5 μm) from Carbon Solutions, Inc. (Riverside, CA) were used throughout this thesis. The matrix was a difunctional bisphenol A/epichlorohydrin liquid epoxy resin (EPON 828) supplied by the Miller-Stephenson Chemical Company, Inc. and has a viscosity of 12000 cP at 25˚C. *m*-Phenylenediamine (mPDA) provided by the Sigma-Aldrich Corporation was used as the curing agent.

2.3.2 Sample Preparation

CNTs were weighed and added to 400 mL of EPON 828 at CNT concentrations of 0.005 wt% and 0.01 wt%. To disperse the CNTs, samples were sonicated for 20 min (125 kJ) using a QSonica Q700 horn sonicator with a 0.5-inch tip. For real-time Raman spectroscopy measurements, 2 mL of the mixture were transferred into poly(methyl methacrylate) (PMMA) cuvettes with an optical path length of 10 mm. For cured specimens, the CNT-EPON 828 mixture was hand mixed with mPDA at a ratio of 7:1 by weight. CNT alignment was induced by applying an electric field during an initial cure stage at 75˚C for 2 hours and then a post-cure stage at 125˚C for 2 hours.

2.3.3 Experimental Setup

An electrostatic potential was generated across two copper parallel plates (0.635 mm thickness) by an Agilent 33500B series waveform generator and a Trek model 2220 high voltage amplifier. All waveforms were sinusoidal with a frequency of 1 kHz unless stated otherwise. The effect of electric field strength on the time to align was systematically studied, and field strengths up to 5000 V/cm were chosen to generate CNT alignment on time scales of interest. These field strengths are consistent with those reported previously to induce CNT alignment within a polymer matrix [56]. Since Joule heating has been shown to be a disruptive factor in the alignment of CNTs [56,107], temperature control is an important aspect. However, for this

study, an electrically insulating matrix and low CNT concentrations were chosen to avoid this effect. The resulting current (on the order of a few μA) did not yield a discernable change in temperature during the experiments.

2.3.4 Real-time Polarized Raman Spectroscopy

Polarized Raman measurements were acquired during the application of an electric field on a CNT-EPON 828 mixture. The Raman scattering intensity is proportional to the number of CNTs falling within the excitation volume of the laser. However, higher concentrations of CNTs increase the likelihood of multiple scattering events as well as increasing the opacity of the mixture, which decreases the penetration depth of the laser. CNT concentrations of 0.005 wt% and 0.01 wt% were found to yield a suitable signal to noise ratio of the spectra. These low concentrations also resulted in an appropriate penetration depth of the laser to limit fringe effects. Electric field conditions were chosen so that the timescales of the observed alignment were large compared to the integration time per spectra.

The technique for *in situ* and real-time characterization of CNT alignment was developed using a Princeton Instruments Trivista TR777 Raman spectrometer and an optical beam path constructed by Aldridge [108] and denoted herein as Spectrometer 1 (Figure 2.1). A laser wavelength of 532 nm at a power of 10 mW was focused on the sample through the side of a PMMA cuvette. The polarizations of incoming and scattered light were controlled via a ½ wave plate and polarizer, respectively, and are denoted by HH or VV scattering geometries (where H is parallel to the electric field direction and V is perpendicular to it); the first letter denotes the polarization of the incoming light and the second letter corresponds to the polarization of the scattered light. Scattered light was collected via backscattering, and the integration time per spectrum was 30 seconds. Spectra were normalized to a PMMA peak at 1730 cm^{-1}, and Lorentzian fits were used to determine the peak heights of the G-bands. Alignment was analyzed by observing the change over time at a constant polarization (HH).

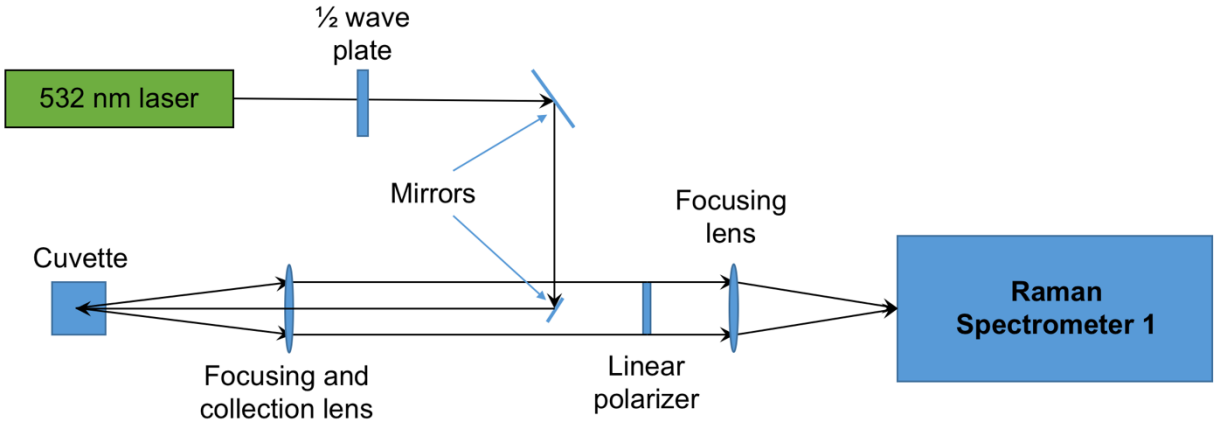

Figure 2.1 – Top down view of the optical setup for Raman Spectrometer 1 (reproduced with permission from M.F. Aldridge). The laser was focused through the sidewall and roughly in the center of the cuvette.

This technique was also demonstrated using a WITec alpha300 R Confocal Raman Microscope denoted herein as Spectrometer 2 (Figure 2.2). A 532-nm laser was focused through a 10x objective at a power of 2.55±0.05 mW and a depth of 400 µm from the surface of the sample. The polarizations of incoming and scattered light were controlled via two wave plates. Scattered light was collected via backscattering, and the integration time per spectrum was 10 seconds. Comparisons between samples were made by normalizing the CNT G-band (~1592 cm^{-1}) with an EPON 828 peak centered at 824 cm^{-1}, which remained approximately constant over the course of an experiment. The ratio of change over time is given by

$$(2.1) \quad I_{\text{norm}} = \frac{I(\text{CNT}_t^{1592})/I(\text{E}_t^{824})}{I(\text{CNT}_0^{1592})/I(\text{E}_0^{824})}$$

where $I(\text{CNT}_0^{1592})$ and $I(\text{E}_0^{824})$ are the initial intensities of the G-band at 1592 cm^{-1} and EPON 828 peak at 824 cm^{-1}, respectively, prior to the application of the electric field, and $I(\text{CNT}_t^{1592})$ and $I(\text{E}_t^{824})$ are the intensities of the G-band and EPON peak at any given time (t) during the experiment. Unless stated otherwise, all polarized Raman data were collected using Spectrometer 2.

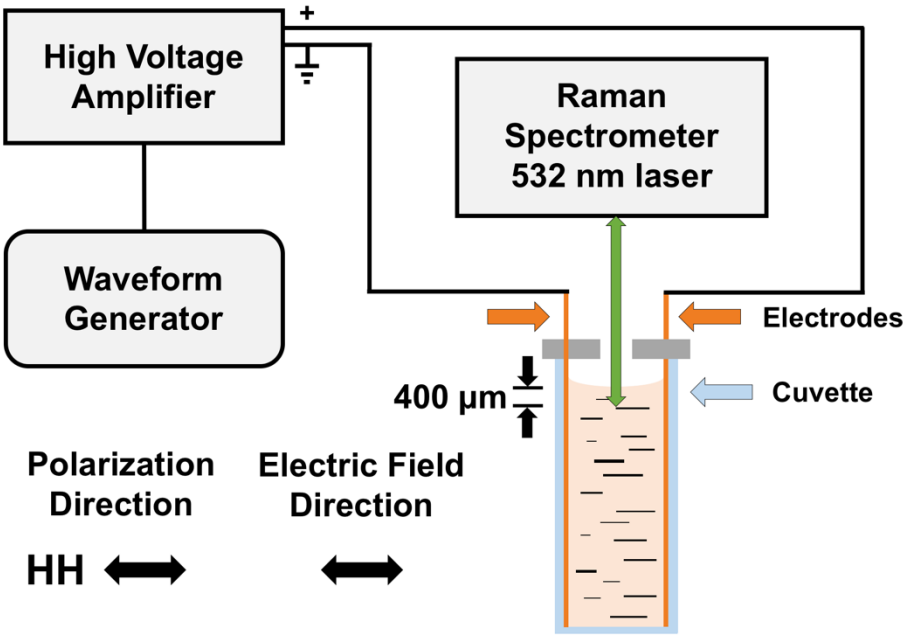

Figure 2.2 – Setup for all spectroscopic measurements on Spectrometer 2 including the power source, Raman spectrometer, and polarization directions. The laser was focused vertically 400 µm from the top of the sample.

Data were analyzed using both maximum intensities of spectral features and peak deconvolution to ensure consistency between the two methods. Raman spectral intensities were treated as the number of detected counts at a certain frequency after a linear background subtraction and normalized according to Eq. (2.1). The Raman spectra of the tested system have spectral features of both the single-walled carbon nanotubes and the EPON 828 epoxy matrix used in this study. These features overlap at various frequencies in the collected spectra. The need to deconvolute the two overlapping spectra was investigated.

In the region of interest, four distinct peaks have been identified. Two originate from the EPON 828 (with maxima near 1583 cm^{-1} and 1612 cm^{-1}), and two come from the CNTs (with maxima near 1570 cm^{-1} and 1592 cm^{-1}). The four peaks were fitted with Lorentzian functions using the program Fityk (Figure 2.3). The sum of the Lorentzian fits closely approximates the collected Raman data. The fitted intensity of the CNT peak at 1592 cm^{-1} was then normalized to the fitted EPON 828 peak at 1612 cm^{-1} as well as the maximum intensity at 824 cm^{-1} (not shown in the figure). Several of these points are shown in Figure 2.4 for a sample aligned with an electric field of 700 V/cm. The deconvoluted data are within ±5% of I_{norm}, which is within the margin of error of the best-fit exponential decay functions. Therefore, maximum intensities were used for the remainder of the study.

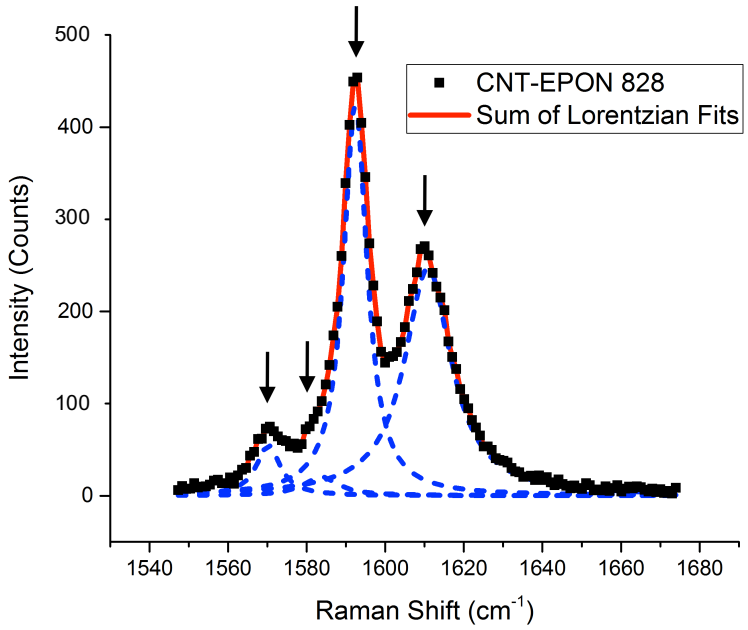

Figure 2.3 – Deconvolution of the overlapping spectral features of the CNT-EPON 828 mixture for an aligned sample at a CNT concentration of 0.01 wt%. Arrows indicate the CNT (1570 cm^{-1} and 1592 cm^{-1}) and EPON 828 (1583 cm^{-1} and 1612 cm^{-1}) spectral features in the chosen frequency range.

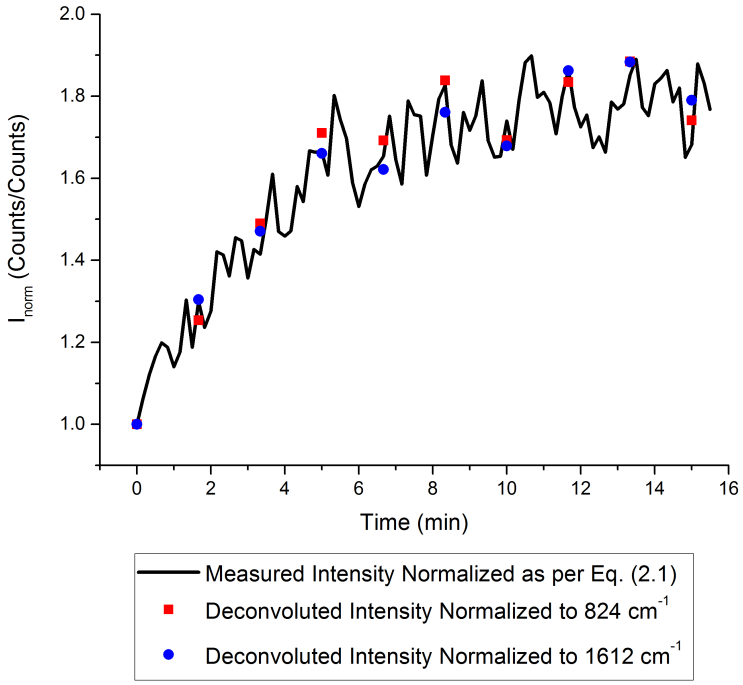

Figure 2.4 – Comparison of the normalized intensity used in the paper to the peak deconvolution data (normalized to EPON 828 peaks at 824 cm^{-1} and 1612 cm^{-1}) at several points during the alignment process. Discrepancies between the two methods were small and yielded no systemic differences.

2.4 Results

CNT alignment is commonly characterized by comparing the intensities of Raman spectra produced by orthogonally polarized incident light in specimens polymerized after alignment. An example of this is shown in Figure 2.5 for a specimen aligned at 300 V/cm. For an electrostatically aligned sample, the G-band intensity increases for a parallel polarization direction (HH) and decreases for a perpendicular one (VV) when compared to an unaligned specimen. The parallel-to-perpendicular ratio is a qualitative indicator of the degree of alignment in which a greater ratio corresponds to a greater degree of alignment. In an isotropic sample, the HH/VV ratio is ~1.

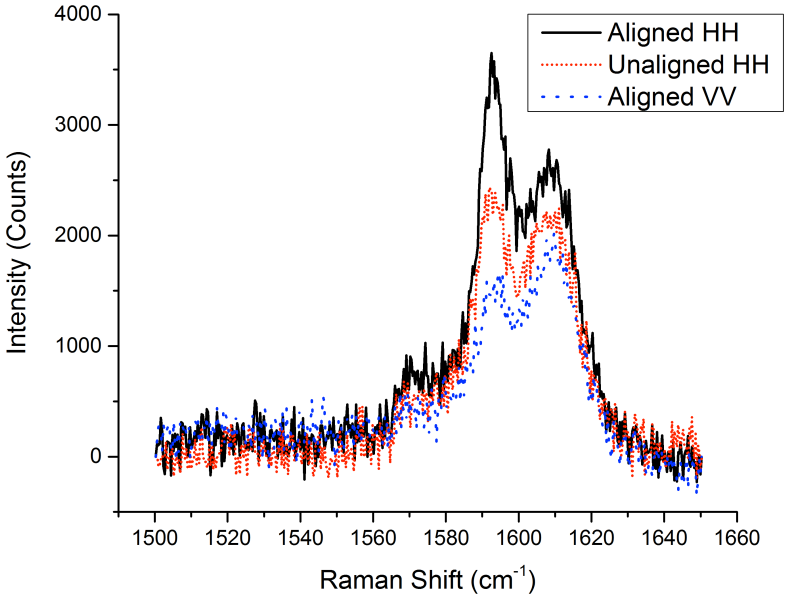

Figure 2.5 – Raman spectra for electrostatically aligned and unaligned polymerized CNT-EPON 828 samples at a CNT concentration of 0.01 wt%. The G-band increases in the HH polarization direction and decreases for the VV polarization direction in the aligned sample with respect to the unaligned sample. Collection times were 2 minutes using Spectrometer 1.

The real-time monitoring of CNT alignment via an electric field is shown in Figure 2.6. Upon applying an electric field of 500 V/cm, the intensities of the Raman peaks in the CNT spectrum begin to increase as the CNTs in the mixture begin to align to a greater extent in the electric field (and polarization) direction (HH). This increase in intensity is most easily observed

for the CNT G-band (Figure 2.6a). The peak values at 1592 cm^{-1} for the experiment in Figure 2.6a are plotted in Figure 2.6b over the time the electric field is applied. Within 10 minutes, the intensity of the G-band reaches 99% of its asymptotic value as determined by an exponential best-fit function:

(2.2) $y = A_1 e^{-x/\tau} + y_0$.

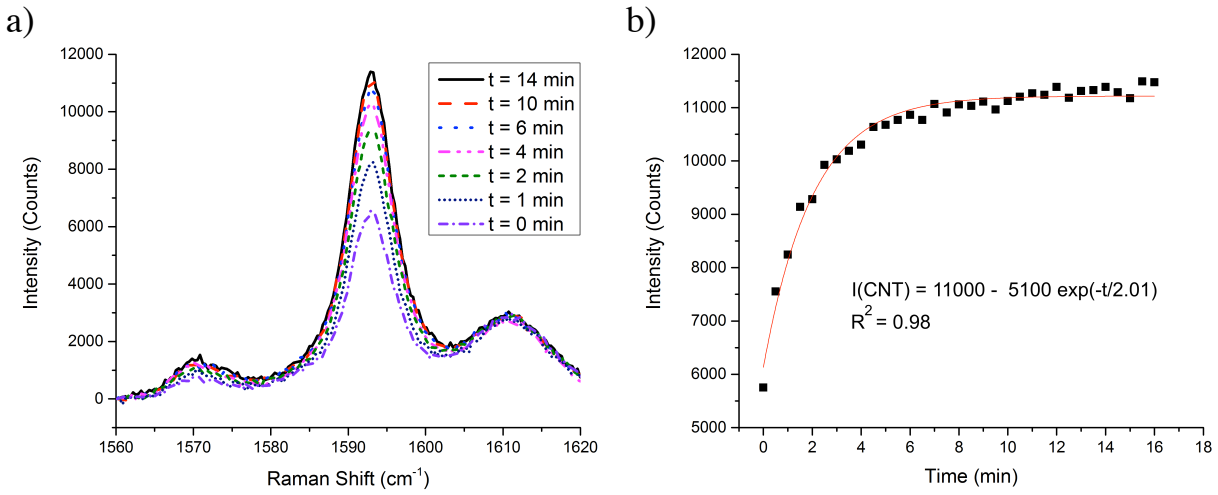

Figure 2.6 – Real-time alignment monitored by (a) the growth of the CNT G-band over time with HH polarization and (b) the G-band intensity plotted as a function of time to align (Spectrometer 1). The electric field (500 V/cm) was applied at t = 0 min. Counts are recorded at 1592 cm^{-1}.

In situ, polarized Raman spectroscopy also offers the ability to study the effects of the electric field strength on CNT alignment. A typical Raman spectrum for the CNT-EPON 828 system is shown in Figure 2.7a. Using the EPON 828 peak at 824 cm^{-1} to normalize the change of the G-band, a comparison of the change over time between samples is possible. As shown in Figure 2.7b, Raman spectra were collected for samples under electric fields of different strengths from 100 to 1100 V/cm. After 30 minutes of alignment induced by the electric field, VV measurements (not shown) were taken of the samples in Figure 2.7b. Using the asymptotic values of fitted curves for the data presented in Figure 2.7b as the HH values, the corresponding HH/VV ratios were calculated and are given in Figure 2.7c along with a data point taken from Park *et al.* [56].

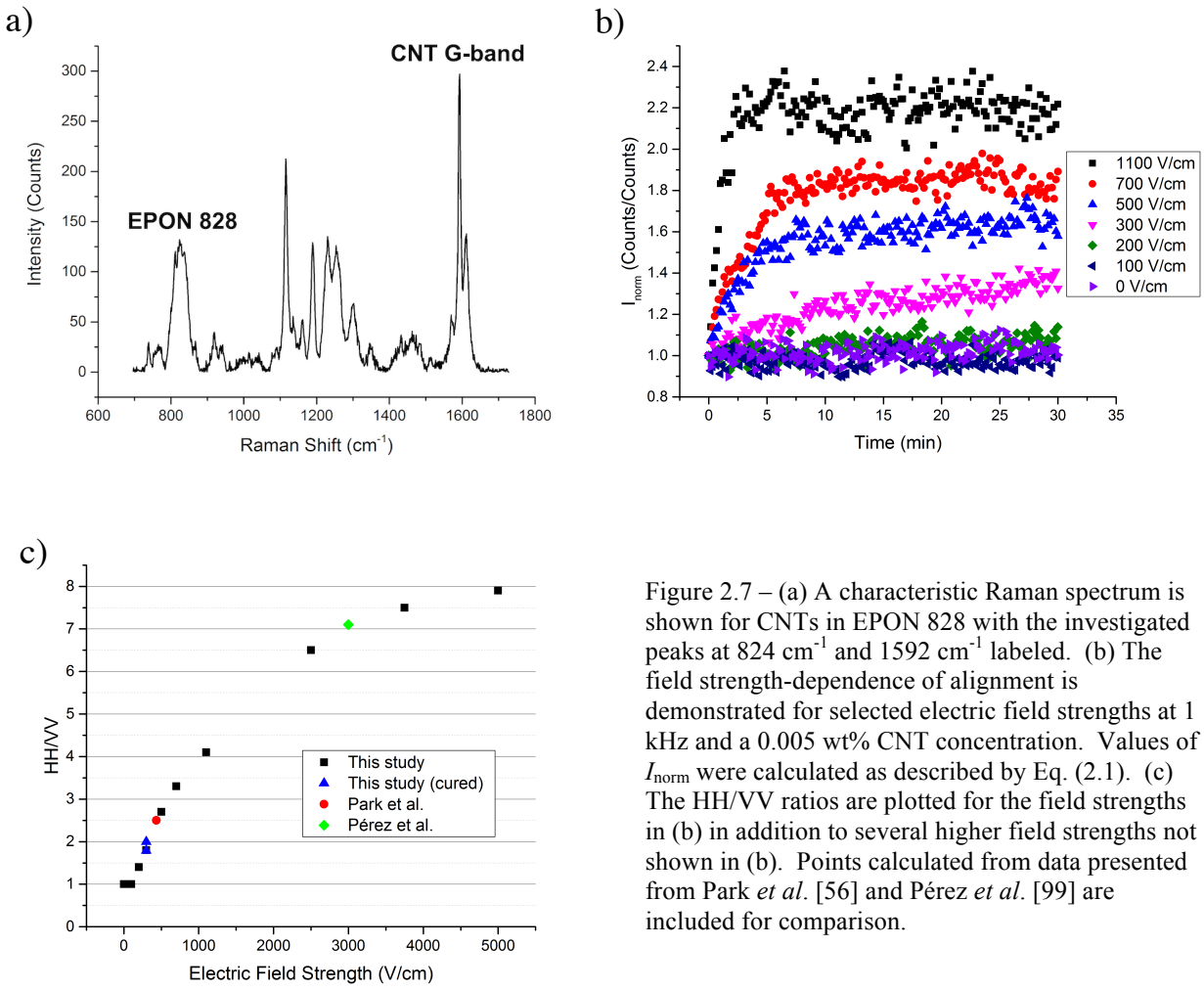

Figure 2.7 – (a) A characteristic Raman spectrum is shown for CNTs in EPON 828 with the investigated peaks at 824 cm^{-1} and 1592 cm^{-1} labeled. (b) The field strength-dependence of alignment is demonstrated for selected electric field strengths at 1 kHz and a 0.005 wt% CNT concentration. Values of I_{norm} were calculated as described by Eq. (2.1). (c) The HH/VV ratios are plotted for the field strengths in (b) in addition to several higher field strengths not shown in (b). Points calculated from data presented from Park *et al*. [56] and Pérez *et al*. [99] are included for comparison.

This technique also allows for *in situ* measurements of the loss of CNT alignment when the electric field is removed (Figure 2.8). The first few minutes after the electric field (500 V/cm) is switched off show a considerable drop in the normalized G-band intensity compared to the asymptotic value of an exponential best-fit curve (Figure 2.8a). After 30 minutes without the electric field, the G-band intensity approaches (but does not reach) the initial measured intensity prior to the application of the electric field.

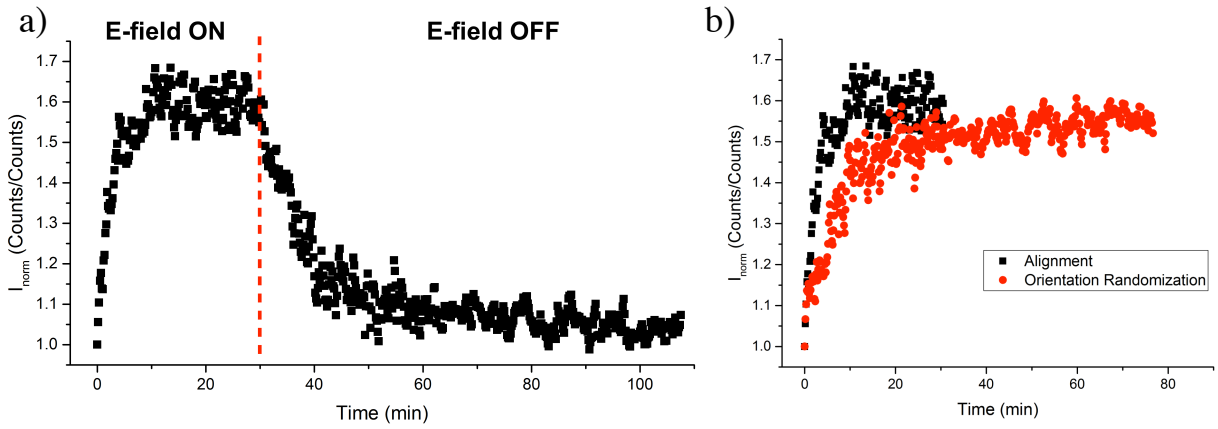

Figure 2.8 – (a) Relaxation time of electrostatically aligned (500 V/cm) CNTs demonstrated by *in situ* polarized Raman spectroscopy. The applied electric field was turned off at t = 30 min. (b) Change in the normalized G-band intensity due to CNT alignment and relaxation seen in (a). Relaxation data were taken as the difference between the value of I_{norm} at t = 30 min and the points from t = 30 min onward with respect to the intensity at t = 0 min.

2.5 Discussion

2.5.1 CNT Alignment as a Function of Electric Field Strength

The *in situ* polarized Raman spectroscopy measurements used in this study demonstrate the ability to measure the change in CNT alignment in real time under an applied electric field (Figure 2.6). Faster alignment has been predicted for CNTs under electric fields of greater frequency and applied potential [67] and observed at higher field strengths via absorbance measurements that take advantage of the linear dichroic nature of CNTs [76,98,106]. CNT alignment measurements under various electric field strengths using real-time Raman spectroscopy (Figure 2.7b) confirm this. The observed timescales of alignment are comparable to those modeled in viscous systems [59,63] and match those reported for electrostatically aligned, cured composites [56,107]. Furthermore, there appears to be a minimum field strength for which alignment is detected, which has been shown previously [56,73].

For higher electric field strengths, a monotonic increase in the HH/VV ratios is observed (Figure 2.7c). The magnitude of alignment determined by this ratio is consistent with the aligned cured composite shown in Figure 2.5 and a previous study by Park *et al*. in a UV-cured epoxy system [56]. This implies that a greater degree of alignment can be achieved by increasing the electric field strength. For a comparison of the degree of alignment achieved in this study against those reported previously [43,44,49–51,56,65,109–115], HH/VV values for single-walled CNTs aligned by various methods are compiled in Table 2.1. The maximum ratio attained in this

study (HH/VV = 7.9) is on the higher end of those generated by electric and magnetic fields but less than those observed for other alignment techniques. These results imply that greater alignment can be obtained with mechanical shearing methods.

Table 2.1 – Single-walled CNT alignment assessed via polarized Raman spectroscopy.

Alignment Method	Maximum Field Strength	Alignment Time	Polymer Matrix	Maximum HH/VV	Reference
Magnetic field	1 T	1-2 days	Aqueous sodium dodecyl sulfate-decanol nematic liquid crystal	2.5	[109]
Magnetic field	8.5 T	10 min	Poly(ethyleneimine)	3	[51]
Magnetic field	9 T	45 min	N-isopropyl acrylamide gel	2	[65]
Magnetic field	9.4 T		Polyethylene terephthalate	3.5	[110]
Magnetic field	25 T		None (buckypaper)	7	[49]
Magnetic field	26 T		None (buckypaper)	4	[50]
Electric field	300 V/cm, 1 kHz	120 min	EPON 828 (cured)	2	This study
Electric field	435 V/cm, 10 Hz	10 min	Urethane dimethacrylate/1,6-hexanediol dimethacrylate blend	2.5	[56]
Electric field	3000 V/cm, 1 kHz	30 min	Urethane dimethacrylate/1,6-hexanediol dimethacrylate blend	7.1	[99]
Electric field	5000 V/cm, 1 kHz	30 sec	EPON 828 (uncured)	7.9	This study
Aligned growth				4	[111]
Drawn fibers			None (CNT fiber)	5	[112]
Drawn fibers			None (CNT fiber)	7.6	[113]
Extruded fibers			None (CNT fiber)	10	[114]
Mechanical stretching			Polyacrylic acid	12	[43]
Extruded fibers (melt spinning)			PMMA	20	[44]
Extruded fibers			None (CNT fiber)	28	[115]

2.5.2 Quantifying CNT Alignment from Polarized Raman Spectroscopy

By determining a distribution function of the aligned CNTs, the degree of alignment can be quantified. The polarized Raman intensity of the CNT G-band can be expressed by

$$(2.3) \quad I_G = \int_{-\pi/2}^{\pi/2} a\, F(\theta)\, cos^2\, \theta\, d\theta$$

where a is a normalization coefficient, $F(\theta)$ is the angular distribution function, and θ is the angle between a nanotube and the orientation axis. The $cos^2\, \theta$ term arises from the dependence of the Raman scattering intensity on the polarization angle [102,116–119] and more closely matches our data than a $cos^4\, \theta$ dependence described elsewhere [43,120]. Using the ratio of orthogonally polarized incoming and scattered light,

$$(2.4) \quad \frac{HH}{VV} = \frac{I_G^{0^\circ}}{I_G^{90^\circ}} = \frac{\int_{-\pi/2}^{\pi/2} F(\theta)\ \cos^2 \theta\, d\theta}{\int_{-\pi/2}^{\pi/2} F(\theta)\ \cos^2\left(\theta - {}^{\pi}/_{2}\right) d\theta}\ .$$

Table 2.2 – Calculated CNT angular distributions and values for Herman's orientation parameter for the various studied electric field strengths.

Electric Field (V/cm)	HH/VV	σ (°)	HWHM (°)	S
200	1.4	68	80	0.03
300	1.8	50	59	0.14
500	2.7	37	43	0.32
700	3.3	32	38	0.40
1100	4.1	29	34	0.49
2500	6.5	23	26	0.64
3750	7.5	21	25	0.68
5000	7.9	20	24	0.69

The angular distribution of aligned CNTs is often assumed to be Gaussian [35,50,103,119]. As such,

$$(2.5) \quad F(\theta) = \frac{1}{\sigma\sqrt{2\pi}} e^{-\theta^2/2\sigma^2}$$

where σ is the standard deviation of the distribution. From experimentally determined intensity ratios, standard deviations of the angular distributions for various applied electric field strengths are calculated and shown in Table 2.2. The standard deviation can be related to a peak half width at half maximum (HWHM) according to

$$HWHM = \sigma\sqrt{2\ln 2}\,. \tag{2.6}$$

These values are included in Table 2.2.

The degree of alignment can also be assessed through an orientation parameter. Herman's orientation parameter (S) is a common example is given by

$$S = \frac{3\langle\cos^2\theta\rangle - 1}{2} \tag{2.7}$$

where

$$\langle\cos^2\theta\rangle = \frac{\int_0^\pi F(\theta)\cos^2\theta\sin\theta\,d\theta}{\int_0^\pi F(\theta)\sin\theta\,d\theta}\,. \tag{2.8}$$

The orientation parameter equals 1 for perfect alignment and 0 for a random distribution. Using the Gaussian distribution functions determined previously, values of S are computed for the studied electric field strengths and collected in Table 2.2. These values are compared with other published orientation parameters for aligned single-walled carbon nanotubes in Table 2.3. Alignment generated via electric field as quantified by the orientation parameter falls between that reported for magnetic fields and various mechanical shear methods. The highest degrees of alignment appear to be achieved through CNT fiber drawing [121] and dry-jet wet spinning processes [122].

Table 2.3 – Orientation parameters (maximum values) for aligned single-walled carbon nanotubes determined using polarized Raman spectroscopy.

Alignment method	S	Reference
Magnetic field	0.37	[121]
Spun CNT fibers	0.42	[123]
Electric field	0.45	[99]
Electric field	0.69	This study
Drawn fibers	0.7	[35]
Stretched films	0.85	[43]
Drawn fibers	0.89	[121]
Spun polyacrylonitrile-CNT fibers	0.94	[122]

2.5.3 Orientation Randomization of CNTs

The loss of CNT alignment once the electric field is removed is shown in Figure 2.8a. Without the impetus to align, the G-band intensity immediately begins to decrease. This decrease in intensity, corresponding to a loss of CNT alignment, appears to approach the initial (pre-alignment) value of I_{norm} but at a slower rate than the electric field-driven alignment (Figure 2.8b). A rapid loss of CNT alignment on the order of tens of milliseconds has been observed previously in low viscosity systems [75,76]. The data presented herein indicate a loss of alignment also occurs in a high viscosity thermoset.

It is important to recognize that a loss of alignment does not correspond to a complete randomization of the system. The decrease in the measured spectral intensity in Figure 2.8b likely results from off-axis deviations from the polarization direction caused by thermal fluctuations in the polymer that dominate upon the removal of the electric field. The timescale of this loss in alignment appears to agree with expected rotational relaxation times [124,125] for the analyzed system and is inversely proportional to the melt viscosity, which agrees with the rotational diffusion of long, rigid rods in polymer melts [126] (see Chapter 3). This phenomenon demonstrates the need for fast polymerization steps or the continued application of the field (or other aligning force) during polymerization to lock in CNT alignment even in the case of viscous polymers.

2.6 Conclusions

Through novel *in situ*, real-time polarized Raman spectroscopy measurements, we have demonstrated the capability of monitoring CNT alignment under an applied electric field as a dynamic system. Whereas previous work has been limited to post-polymerization analyses or absorbance measurements in optically transparent solvents, this technique can be applied as a diagnostic tool to characterize CNT alignment in real time in structural polymer matrices of interest. With these measurements, we demonstrate the capability of analyzing the effects of several material parameters such as composite viscosity (Chapter 3) and CNT length (Chapter 4) on the degree and speed of alignment induced by an electric field. These analyses are imperative in developing a better understanding of the alignment process, which is crucial in efficiently creating aligned polymer nanocomposites with enhanced mechanical and electrical properties.

CHAPTER 3
ROTATIONAL FRICTION OF CARBON NANOTUBES IN A POLYMER

3.1 Chapter Synopsis

Carbon nanotube rotation induced by an electric field is analyzed using *in situ*, real-time polarized Raman spectroscopy. This technique for monitoring a dynamic system enables a measurement of the change in carbon nanotube alignment for various field strengths and temperatures as a function of time after the field is applied. The calculated activation energy of carbon nanotube rotation is similar to that of the viscous flow of the thermoset polymer matrix, and the speed of rotation is shown to be inversely proportional to the composite viscosity as described by a continuum model. The experimental results are compared to theoretical work from the literature concerning the diffusion of rigid rods in polymer melts, which indicate a shear viscosity controlling mechanism for carbon nanotube rotation.

3.2 Introduction

The speed of rotation of a CNT is proportional to the rotational energy over the resistance to rotation. With no externally applied fields, the thermal energy is the dominant mechanism of the system. Above 0 K, the thermal energy results in the rotational diffusion of the particles, which causes them to rotate randomly ad infinitum (Figure 3.1). For an applied electric field of sufficient magnitude, the electrostatic potential energy U_E exceeds the thermal energy:

(3.1) $U_E > 2k_BT$.

As a result, the electric field-induced torque forces the CNTs to align in the direction of the electric field as long as it is applied (Figure 3.1).

For both thermally and electrostatically driven rotation of particles, the resistance force is accurately described by the rotational friction, assuming no covalent bonding exists between the particles and the matrix. On a macro- or microscale, the rotational friction is related simply to the shear viscosity of the system.

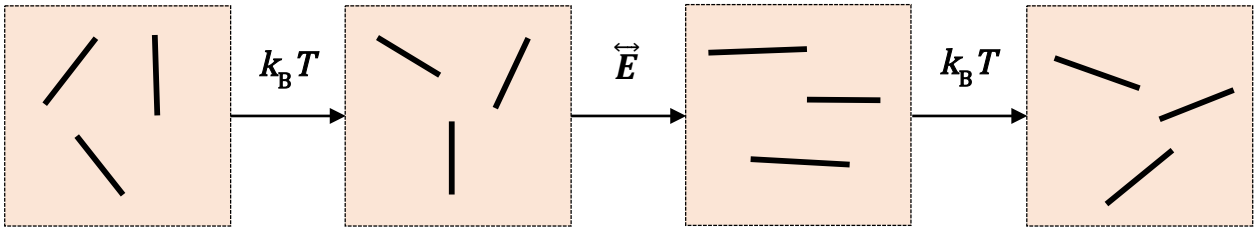

Figure 3.1 – A schematic demonstrating CNT rotation that results from thermal and electric field energies. Random rotation of CNTs (rotational diffusivity) results from the thermal energy of the system. Forced rotation of CNTs into the electric field direction occurs upon the application of an electric field of sufficient magnitude. When the electric field is removed, CNTs reassume a random orientational distribution.

Viscosity results from the average friction arising from the viscous flow of polymer chains [127] and can be accurately described by a continuum model. However, inconsistencies emerge when using shear viscosity (η_0) to describe particle mobility in a polymer melt as the size of the particle decreases to the nanoscale. Measurements of nanoparticle translational diffusion constants (D_t) [128–130] and theoretical analyses of nanoparticle-polymer chain dynamics [131–133] point toward a local viscosity (η_L) mechanism for small, spherical particles where $\eta_L << \eta_0$.

Polymer chain length plays an important role in the mobility of nanoparticles and can be divided into two groups: long chain and short chain. For a spherical nanoparticle in a long chain (entangled) polymer melt, the critical dimensions for particle mobility are the diameter of the nanoparticle (d_P) and the mesh entanglement length of the polymer [134] (d_T ~ 3-9 nm) [135]. For a short chain (unentangled) polymer melt, the critical dimensions are the nanoparticle diameter and the radius of gyration (R_g) of the polymer coil [134]. Particles for which $d_P >> d_T$ in entangled polymers and $d_P >> R_g$ in unentangled polymers behave according to Stokes-Einstein diffusion (D_{SE}) [136]. Faster diffusion is predicted for extremely small particles ($d_P \leq d_T$ for entangled polymers and $d_P \leq R_g$ for unentangled polymers) [131,132]. The point at which Stokes-Einstein diffusion is expected to recover is when $d_P \sim 10 \cdot d_T$ in entangled polymers and $d_P \sim 3 \cdot R_g$ in unentangled polymers [131].

These predictions have been confirmed through x-ray photon correlation spectroscopy [128] and fluorescence correlation spectroscopy [129] measurements in which Stokes-Einstein diffusion underestimates experimentally determined diffusion constants for $d_P \sim d_T$ in an entangled melt. Grabowski *et al.* also demonstrated the importance of chain entanglement on

nanoparticle diffusion by experimentally showing that $D_t \sim 250 \cdot D_{SE}$ for high molecular weight (entangled) poly(*n*-butyl methacrylate) (PBMA) in which $d_P \sim d_T$; Stokes-Einstein diffusion was recovered for low molecular weight (unentangled) PBMA where $d_P > R_g$ [130].

However, for CNTs in which the radius is measured in nanometers and the length is typically on the order of microns, a comparison to nanoscale spheres may not be appropriate. A CNT may instead be thought of as a long, rigid rod up to lengths of 10 μm [137]. For CNT alignment, rotation (rather than translation) is the motion of interest (Figure 3.2). The rotational diffusion constant (D_r) of long, thin rods is predicted to be proportional to shear viscosity [126] and shows an experimentally determined length dependence ($D_r \sim 1/L^3$) [134,138]. Both of these relationships are consistent with the continuum model.

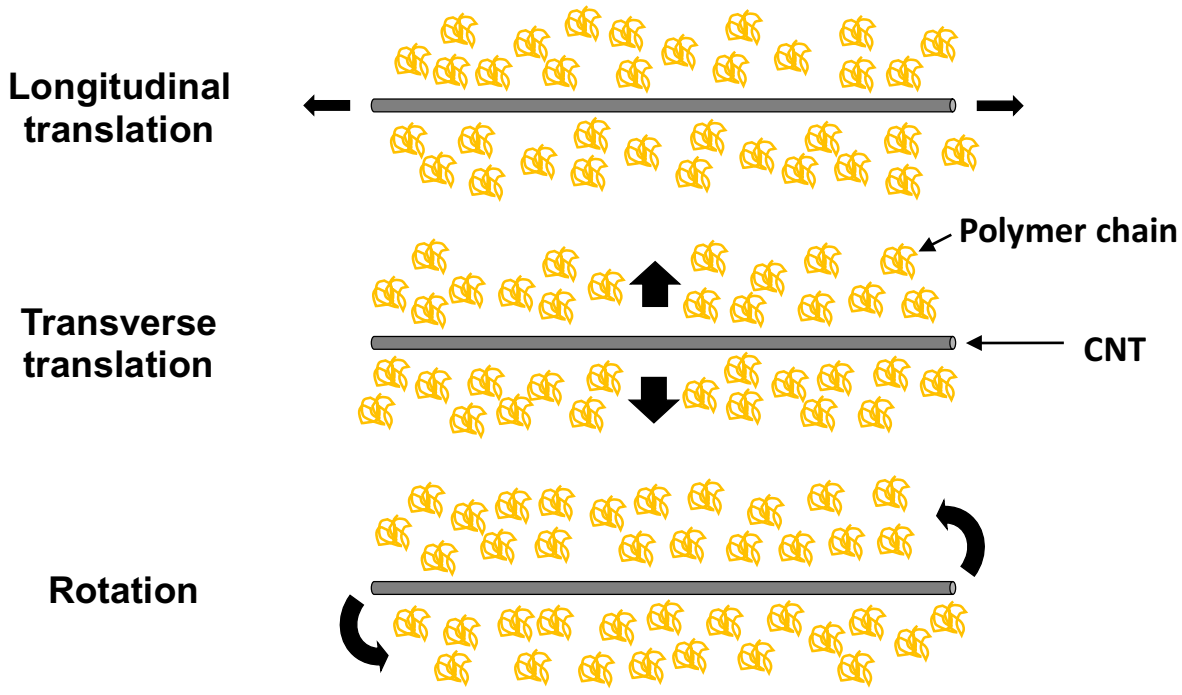

Figure 3.2 – Different forms of motion for a nanotube through a polymer.

In this chapter, electric field-induced rotation of CNTs in a polymer is analyzed and compared with predictions of long, rigid rods [126] and observations from other nanoscale rod-like molecules in solution [138,139]. Polarized Raman spectroscopy has proven to be an

effective diagnostic tool for assessing the degree of CNT alignment in polymer composites. We previously demonstrated the ability to make real-time polarized Raman measurements *in situ* to monitor the reorientation of CNTs under an applied electric field [62] (see Chapter 2). From these measurements, activation energies of the rates of CNT rotation at various electric field strengths are determined and compared to that of the viscous flow of the unentangled polymer used in this study.

3.3 Experimental

The materials, sample preparation, method of electrostatically inducing CNT alignment, and real-time polarized Raman spectroscopy measurements were conducted as described in Chapter 2. A CNT concentration of 0.005 wt% was used for this Chapter. Temperature measurements were taken with a Fluke 179 True-RMS multimeter. A custom-built temperature stage was used to control the sample temperature during experiments. Each sample was brought to and held at a predetermined temperature at which point the electric field was activated and polarized Raman measurements were taken.

All rheological measurements were made using an ARES LS (Rheometric Scientific) with a 50-mm diameter parallel plate geometry and a 1-mm gap. Zero-shear viscosity (η_0) was recorded as the viscosity of the sample as the shear rate approached 0 (i.e. the Newtonian regime). Viscosities were determined for neat EPON 828 as well as EPON 828 with 0.005 wt% CNT additions at various temperatures from 20–50˚C. Discrepancies between the measured viscosities and those provided by the manufacturer [140] were small (< 5%) at all studied temperatures.

3.4 Results

3.4.1 Activation Energy of the Viscous Flow of EPON 828

It was determined experimentally that the small additions of CNTs (0.005 wt%) had a minimal effect on the measured viscosity of EPON 828 (Figure 3.3a). An Arrhenius model—

$$\ln \eta_0 = \left({E_a}/{RT}\right) + \ln A \tag{3.2}$$

where E_a is the activation energy of the viscous flow of the polymer, R is the universal gas constant, T is the temperature of the sample, and A is an exponential coefficient—is applied over the temperature range of interest. Since an Arrhenius model becomes increasingly inaccurate in

describing changes in viscosity for amorphous materials as the temperature range increases, the temperature range studied was divided into three smaller ranges over which ln k vs $1/T$ was determined to be roughly linear (Figure 3.3b). From these smaller temperature divisions, an activation energy range of 67–85 kJ/mol was calculated as per Eq. (3.2).

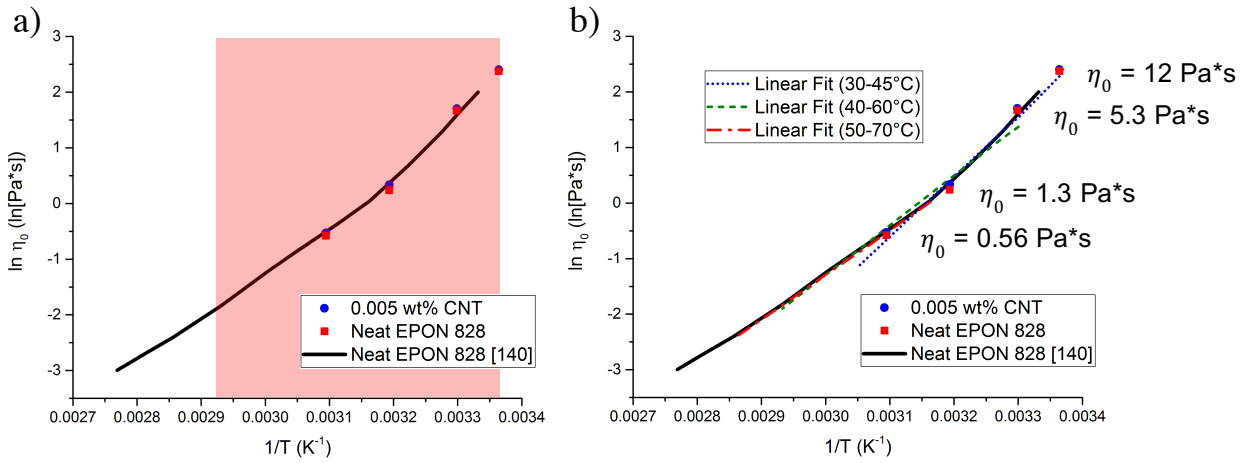

Figure 3.3 – a) Zero-shear viscosity for the 0.005 wt% CNT mixture compared to neat EPON 828. The data points are the measured viscosities and solid line is from the manufacturer [140]. The shaded region denotes the studied temperature range. b) The temperature dependence of viscosity was examined by using linear fits over three narrow temperature ranges. Activation energies are computed from the linear best-fits using Eq. (3.2).

3.4.2 Activation Energy of CNT Rotation

Alignment experiments were performed at various electric field strengths and temperatures. An example of one of these experiments at 300 V/cm is given for select temperatures in Figure 3.4. Exponential decay functions are fitted to the intensity-time data according to Eq. (2.2). As seen in Figure 3.4b, the initial rate of change of the G-band intensities (normalized to $t = 0$) increases with temperature. This corresponds to decreasing time constants as temperature is increased: $\tau(22^{\circ}C) > \tau(33^{\circ}C) > \tau(51^{\circ}C)$. However, the data appear to approach a similar asymptotic value regardless of temperature, i.e. $A_1(22^{\circ}C) \approx A_1(33^{\circ}C) \approx A_1(51^{\circ}C)$.

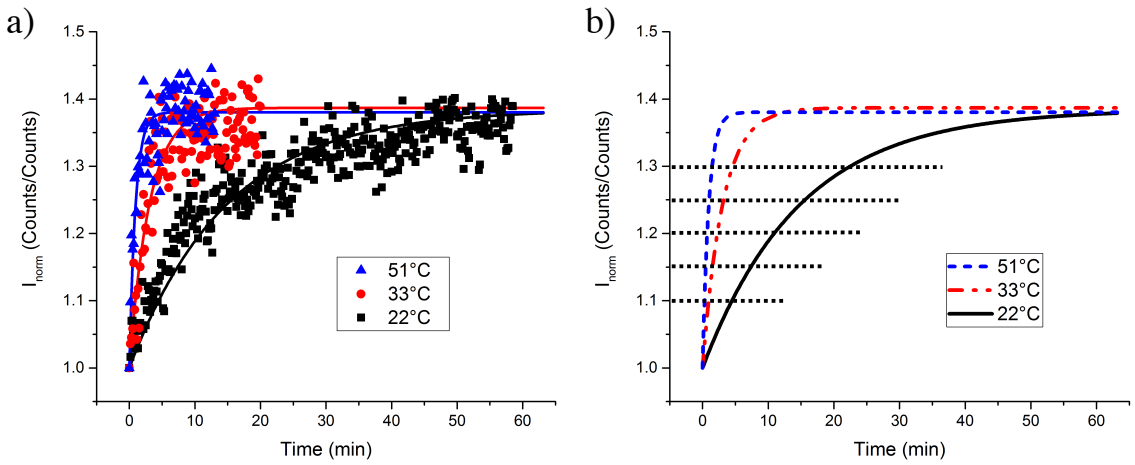

Figure 3.4 – a) Change in the CNT G-band intensity (normalized to $t = 0$) over time at select temperatures. The electric field strength was 300 V/cm for all samples. b) Exponential decay functions have been fitted to the data at each temperature. The intersections of the best-fits with each dotted line represent equivalent points of alignment across the samples.

To compare data from different samples, rate constants k are compared at equivalent values of I_{norm} (i.e. where the dotted lines intersect the best-fit functions in Figure 3.4b). Rate constants are determined from the slopes of the best-fit functions for a given I_{norm} at the various temperatures according to

$$k = \frac{dI_{\text{norm}}(t)}{dt} \tag{3.3}$$

where $I_{\text{norm}}(t)$ is the normalized intensity at a certain time t during the alignment process. These rate constants are related to temperature by the Arrhenius equation

$$\ln k = \left({}^{-E_a}/_{RT}\right) + \ln A \,, \tag{3.4}$$

and the results are shown in Figure 3.5. Each plotted dataset corresponds to a normalized intensity value and represents an equivalent point during the alignment process across all studied temperatures.

Activation energies are computed from the slopes of the linear best-fits. The process was repeated for a range of electric field strengths (200-700 V/cm), and the results are collected in Figure 3.6. The activation energy range determined for the viscous flow of the polymer is also shown.

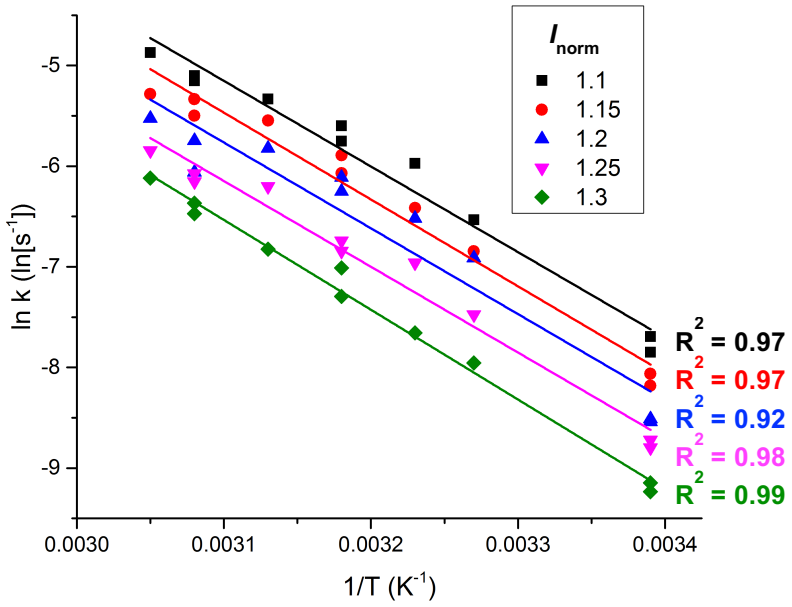

Figure 3.5 – Rate constants determined at several normalized intensities (indicated in the inset by the dotted lines) for all 300 V/cm experiments. The slopes of the linear best-fits are related to the activation energy through Eq. (3.4).

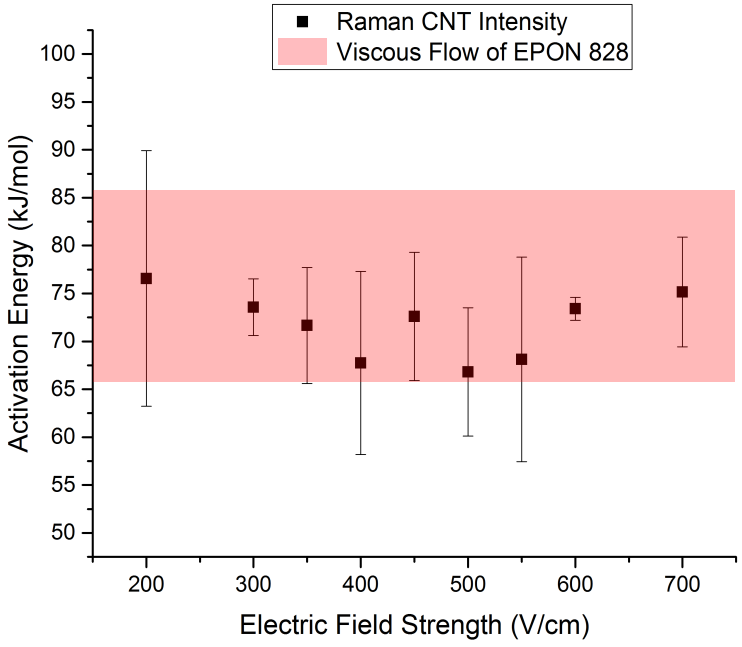

Figure 3.6 – Activation energy of the change in Raman CNT intensity for the studied electric field strengths. The activation energy of the viscous flow of EPON 828 is plotted for comparison. Error bars denote three sigma confidence intervals.

3.4.3 Shear Viscosity Dependence of CNT Rotation

Due to the change in free volume of the polymer coils with temperature, an Arrhenius model assuming a constant activation energy becomes increasingly inaccurate over larger temperature ranges. To describe the change in viscosity with respect to temperature, a Vogel-Fulcher model given by [141]

$$\log\eta = -A + {}^{B}/_{(T - T_0)} \quad (3.5)$$

is commonly used. However, this approach, although reducing the margin of error, still indirectly relates the speed of CNT rotation to the composite viscosity through temperature. Instead of the indirect comparison through temperature, a more straightforward analysis would be to compare the speed of CNT rotation directly to the composite viscosity.

The speed of CNT rotation can be determined by relating the electrostatic-induced torque τ_E to the rotational friction coefficient ζ_R by [75]

$$\vec{\omega} = \frac{\overrightarrow{\tau_E}}{\zeta_R}, \quad (3.6)$$

where ω is the angular velocity of a CNT. For a continuum model, the rotational friction coefficient for a CNT can be related to that of a thin rod [124,142] according to

$$\zeta_R = \frac{\pi\eta L^3}{3\left[\ln\left(\frac{L}{r} - \gamma\right)\right]} \quad (3.7)$$

where r is the radius of the rod and γ is a correction factor. Combining Eqs. (3.6) and (3.7) shows that the magnitude of the speed of rotation will be inversely proportional to the shear viscosity:

$$\omega = \frac{3\tau_E}{\pi\eta L^3}\left[\ln\left(\frac{L}{r} - \gamma\right)\right] \propto \frac{1}{\eta}. \quad (3.8)$$

Since ω can be described by the rate of change in the polarized Raman intensity through the rate constant k, an inverse relationship between k and η is expected. This is confirmed in Figure 3.7a. Taking the natural log of each side of the equation results in a linear relationship between ln k and –ln η_0 as shown in Figure 3.7b.

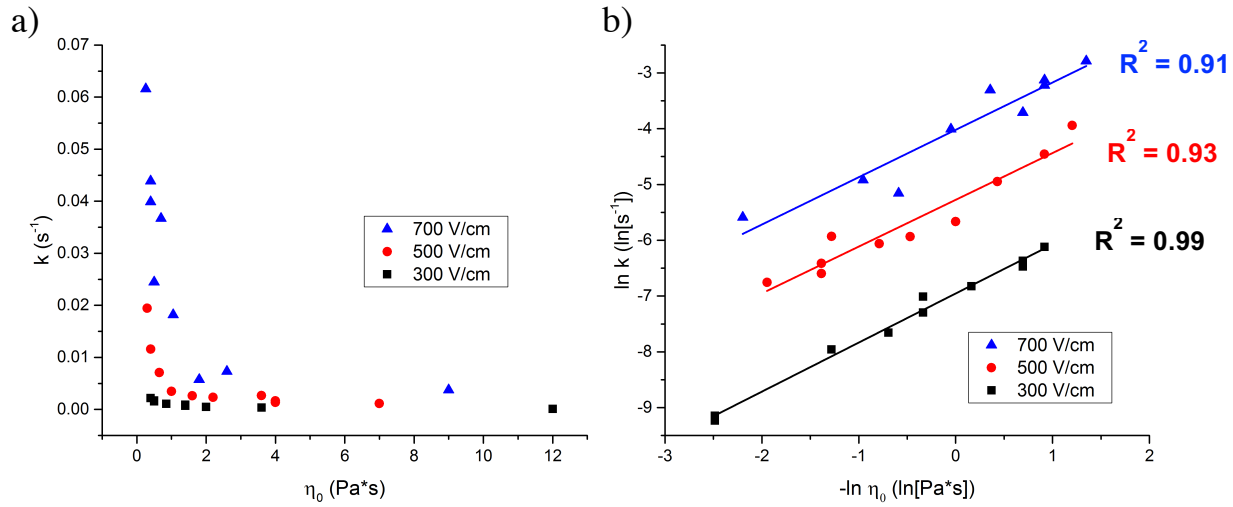

Figure 3.7 – A comparison of the rate constant k against the zero-shear viscosity of the mixture for the selected electric field strengths. Data points were taken at an I_{norm} of 1.3.

3.5 Discussion

The activation energy for the change in the polarized Raman CNT intensity induced by an electric field appears to fall within the bounds of the activation energy range determined for the viscous flow of EPON 828 (Figure 3.6). This change in intensity is interpreted as the average CNT rotation that occurs in response to an applied electric field. Furthermore, a direct comparison of the speed of CNT rotation to the viscosity of the mixture (Figure 3.7) showed an inverse relationship predicted by a continuum model. These results suggest that shear viscosity serves as the controlling mechanism for CNT rotation, which is consistent with Stokes-Einstein diffusion.

Using neutron scattering, a correlation between molecular weight and R_g for DGEBA resins has been determined [143]. The EPON 828 used in this study had a molecular weight of 380 g/mol, which yields an expected $R_g \sim 0.6$ nm. The average diameter of the CNTs used in this study was $d_{avg} = 1.4$ nm, which corresponds to $d_{avg} \sim 2.5 \cdot R_g$. Based on this work and previous theoretical and experimental analyses [126,131,138,139], it would therefore seem feasible to apply the macroscopic phenomenon of shear viscosity to describe the primary resistive force acting against electric field-induced rotation of CNTs. This finding indicates that the manipulation of temperature (and indirectly the viscosity of the matrix) will have a direct

effect on the rate of CNT alignment, which could prove useful in expediting the manufacturing of CNT-reinforced composites cured at elevated temperatures.

Future work will attempt to analyze the effects of increasing polymer size relative to d_{CNT} in order to corroborate predicted [127] and experimentally determined [144] deviations from Stokes-Einstein diffusion of nanoscale rods in which $d_P < d_T$.

3.6 Conclusions

Using a newly developed polarized Raman spectroscopy technique for analyzing CNT reorientation in real time, information regarding the speed of CNT rotation at various temperatures was interpreted from the collected data. From this, an activation energy of CNT rotation was calculated and compared with that of the viscous flow of EPON 828. Equivalent activation energies imply a controlling mechanism of shear viscosity for CNT rotation, which was confirmed through a comparison of the speed of CNT rotation to the composite viscosity. This conclusion was explained by theoretical studies on the motion of rigid rods in polymer melts. Knowledge of the controlling mechanism of CNT rotation may prove useful in the manufacturing of aligned CNT composites with enhanced properties.

CHAPTER 4
LENGTH DEPENDENCE OF ELECTROSTATICALLY INDUCED CARBON NANOTUBE ALIGNMENT

4.1 Chapter Synopsis

In situ, real-time polarized Raman spectroscopy was used to measure electrostatically induced carbon nanotube alignment in a polymer matrix. Discrete and reversible asymptotes of carbon nanotube G-band intensity were observed as a function of the applied electric field strength. It is proposed that as the electric field is increased, certain populations of carbon nanotubes attain sufficient alignment energy to overcome the randomizing thermal energy of the system. This is due to the alignment energy being a function of nanotube length. The effects of processing parameters such as sonication on the degree of achievable alignment as well as its implications are discussed.

4.2 Introduction

The ability to manipulate nanoparticles to tailor composite properties is a growing area of interest [37,56,61,74,145,146]. The use of external electric fields is one method for controlling carbon nanotubes (CNTs) in solution or in a polymer. Both AC and DC electric fields can result in CNT alignment and in some cases network formation [61]. Network formation, which creates conductive CNT filaments in an insulating polymer matrix, has been observed at concentrations as low as 0.002 wt% [74]. Applications for the manipulation of CNTs with electric fields are not limited solely to electrical properties. Due to the high anisotropy of nanotubes, electric field-induced rotation can lead to aligned arrays of CNTs [56] that lead to improvements in composite mechanical properties [37].

The study of CNT alignment induced by an electric field has been modeled [63,67] and experimentally analyzed [75,76] as a function of electric field strength and frequency. In response to an electric field, a dipole is created on the CNT surface. Nanotube rotation results from the electrostatic torque exerted on this dipole. For a CNT to orient in response to an

electric field, the alignment energy must exceed the thermal energy of the system ($U_E > 2k_BT$) [68–72]. This is validated by the observation of a minimum electric field strength for detectable alignment of both multi-walled (46.5 V/cm) [73] and single-walled CNTs (150–163 V/cm) [56,62].

The alignment energy is denoted as

$$U_E = \int \tau_E \, d\theta \tag{4.1}$$

where τ_E is the electrostatically induced torque on the CNT and θ is the angle between the electric field direction and the long axis of the CNT (Figure 4.1). The torque can be expressed as

$$\overrightarrow{\tau_E} = \vec{p} \times \vec{E} = \left(\alpha_{zz} \cdot \vec{E}\right) \times \vec{E} = \alpha_{zz} E^2 \sin\theta \cos\theta \tag{4.2}$$

where $\vec{p}$ is the CNT dipole in response to the electric field, $\vec{E}$ is the magnitude and direction of the applied electric field, and α_{zz} is the polarizability along the length of the CNT. Combining Eqs. (4.1) and (4.2) results in [68]

$$U_E = -\frac{1}{2}\alpha_{zz} E^2 \cos^2\theta \, . \tag{4.3}$$

It has been shown that the polarizabilities of dielectric rods have an L^2 dependence [147,148]; this L^2 proportionality is predicted to extend to CNTs [72,98,149]. Therefore, the alignment energy of a CNT will also depend on L^2.

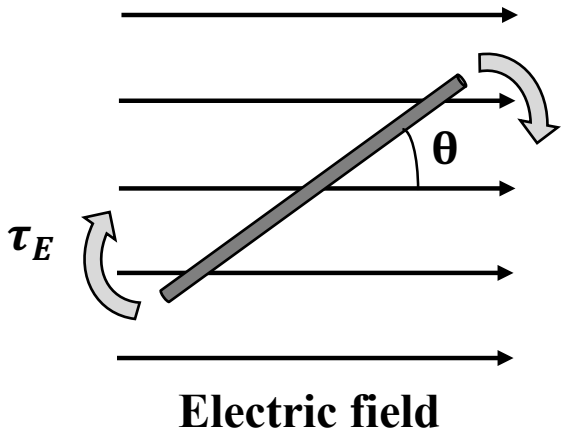

Figure 4.1 – A CNT initially oriented at an angle θ with respect to the electric field direction. The electric field induces a torque τ_E on the CNT.

Current scalable CNT growth processes result in tubes that are length-polydisperse [125]. Within a single batch, individual CNTs will therefore have different alignment energies for the same applied electric field strength. Correspondingly, electric fields of different strengths result in different populations of nanotubes with enough alignment energy to overcome thermal agitations. Different degrees of CNT alignment as a function of electric field strength have been previously demonstrated in solution [76] and within a polymer [62] using real-time measurements.

The length distribution of a batch of CNTs is one parameter that affects the degree of alignment at a constant electric field strength. This length dependence has been shown experimentally for multi-walled CNTs with transmission electron microscopy [150]. In addition to the length-polydispersity that results from CNT growth, violent dispersion processing such as sonication has been shown to shorten tube length through a scission process [151,152]. Sonication preferentially shortens smaller diameter [151,153] and longer tubes [151] down to a critical length of ~120 nm [154]. The relation between the sonication energy and the resultant average CNT length can be described by a power law [154]. CNT lengths follow a log-normal distribution both before and after sonication [151]; increased sonication narrows the distribution and shifts the mean to a shorter length. However, sonication does not significantly affect the electronic structure of the nanotube outside of the CNT ends [155], which makes spectroscopic techniques such as Raman spectroscopy viable tools for post-sonication analyses.

In creating aligned CNT composites for electrical and mechanical applications, CNT length is an important variable that has a direct effect on the degree of achievable alignment. Since CNT length distributions are affected by composite processing steps, the magnitude of alignment will depend on the dispersion steps used. As a result, optimization of dispersion processing and alignment needs to be considered together when making aligned nanocomposites with enhanced properties. The aim of this study is to investigate the degree of electrostatically induced alignment as a function of CNT length distributions.

4.3 Experimental

4.3.1 Sample Preparation

The materials, sample preparation, method of electrostatically inducing CNT alignment, and real-time polarized Raman spectroscopy measurements were conducted as described in

Chapter 2. A CNT concentration of 0.005 wt% was used for this chapter. The effect of sonication energy (100-360 kJ) on nanotube length and the degree of alignment was analyzed.

4.3.2 Characterization

Polarized Raman spectra were collected using a WITec alpha300 R Confocal Raman Microscope. A 532-nm laser was focused through 10x objective at a laser power of 2 mW. Specifics of real-time polarized Raman spectroscopy are detailed in Chapter 2.
Samples were prepared for atomic force microscopy (AFM) by sonicating CNTs (0.005 wt%) in an aqueous solution of sodium dodecyl sulfate (0.05 wt%) for selected sonication energies. 10 μL of solution were drop cast onto silicon substrates and then rinsed with deionized H_2O. AFM images were collected on an Asylum Research MFP-3D AFM operated under ambient conditions at room temperature. This study used silicon tapping mode tips (Aspire CT300) with a resonant frequency of 300 kHz, a spring constant of 40 N/m, and a radius of curvature of 8 nm. 5x5 μm scans were taken at a scan rate of 0.5 to 1.5 Hz. CNT lengths were computed by using the scientific image analysis program ImageJ. Sampling sizes consisted of 300–400 CNTs at each sonication energy.

4.4 Results

The degree of alignment as a function of electric field strength was investigated. Specimens were electrostatically aligned at a constant electric field strength. Normalized CNT intensity was calculated as per Eq. (2.1). The I_{norm} versus time plots (Figure 4.2a) were fitted with exponential decay functions as detailed in Chapter 2. The asymptotes of these best-fit functions are plotted with respect to the applied electric field strength in Figure 4.2b. No change in CNT intensity measured with polarized Raman spectroscopy was observed at the lowest tested electric field strength (100 V/cm). For electric fields above this minimum threshold, the asymptote of I_{norm} increases monotonically up to the highest studied electric field of 5000 V/cm.

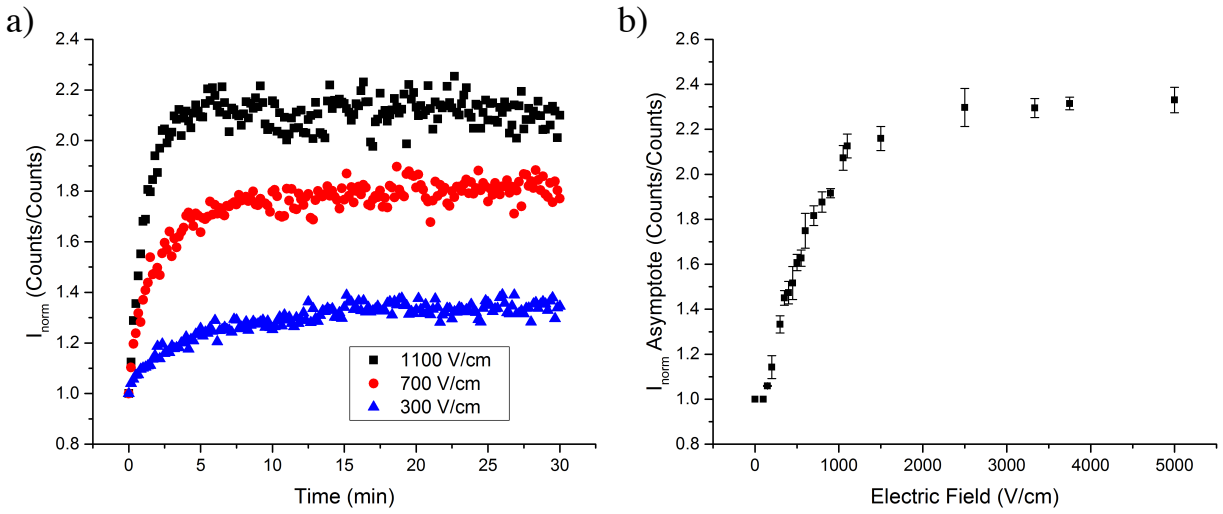

Figure 4.2 – a) The change in I_{norm} over time for selected electric field strengths. b) Asymptotic values of I_{norm} achieved at a constant electric field strength for the electric fields shown. Asymptotes increase monotonically with respect to the applied field. Error bars denote one standard deviation.

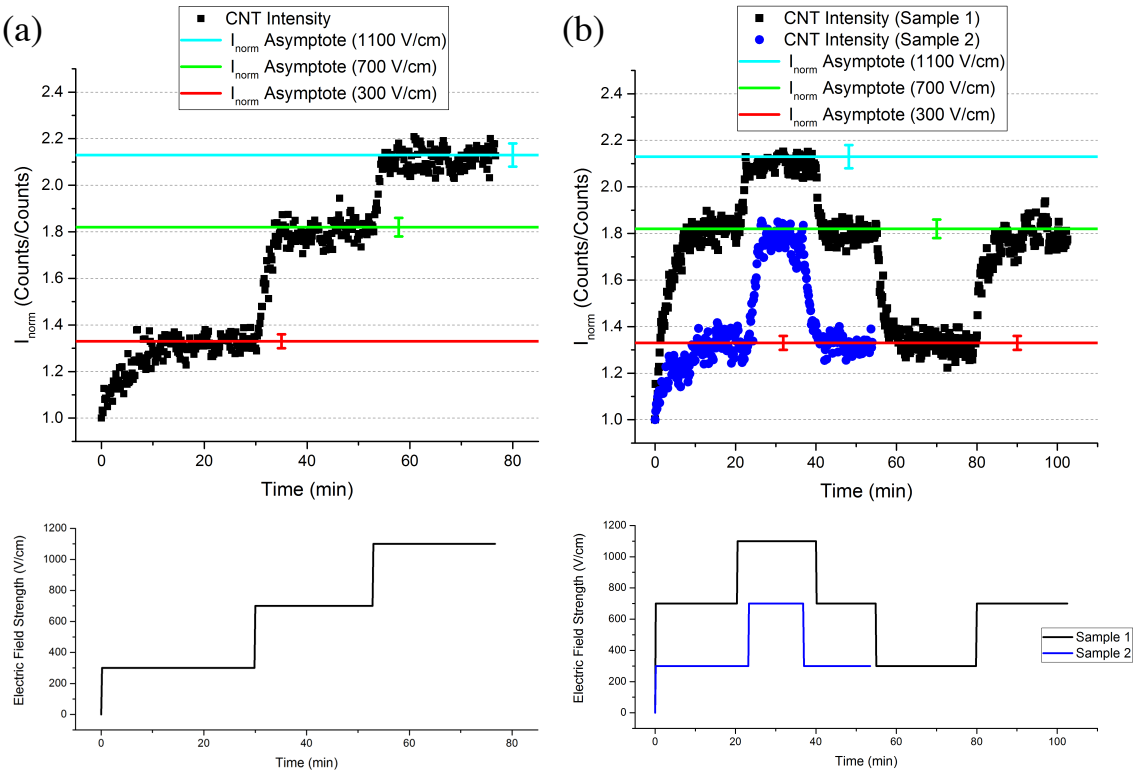

Figure 4.3 – (a) The electric field strength was increased as a step function, and the corresponding changes in polarized Raman CNT intensity are shown. (b) An electric field was varied between the electric field strengths shown. The solid lines are the average values of the asymptotes with one standard deviation error bars of all the iso-electric field experiments conducted. Depending on the applied electric field, reproducible values of I_{norm} are generated.

The reversibility of I_{norm} was also investigated by varying the applied electric field strengths for a single specimen (Figure 4.3). In Figure 4.3a, the electric field was increased as a step function (from 300 V/cm to 700 V/cm to 1100 V/cm), and the corresponding changes of I_{norm} in response are plotted. Figure 4.3b shows two experiments in which the electric fields were varied between selected electric field strengths (300 V/cm, 700 V/cm, and 1100 V/cm). The same I_{norm} asymptotes were observed for a given applied electric field independent of the prior electric field strength. The process of switching the electric field strength (from 300 V/cm to 700 V/cm) was further explored over multiple cycles in Figure 4.4. The discrete values of I_{norm} as a function of the applied field are reproducibly attained through nine cycles at the field strengths tested.

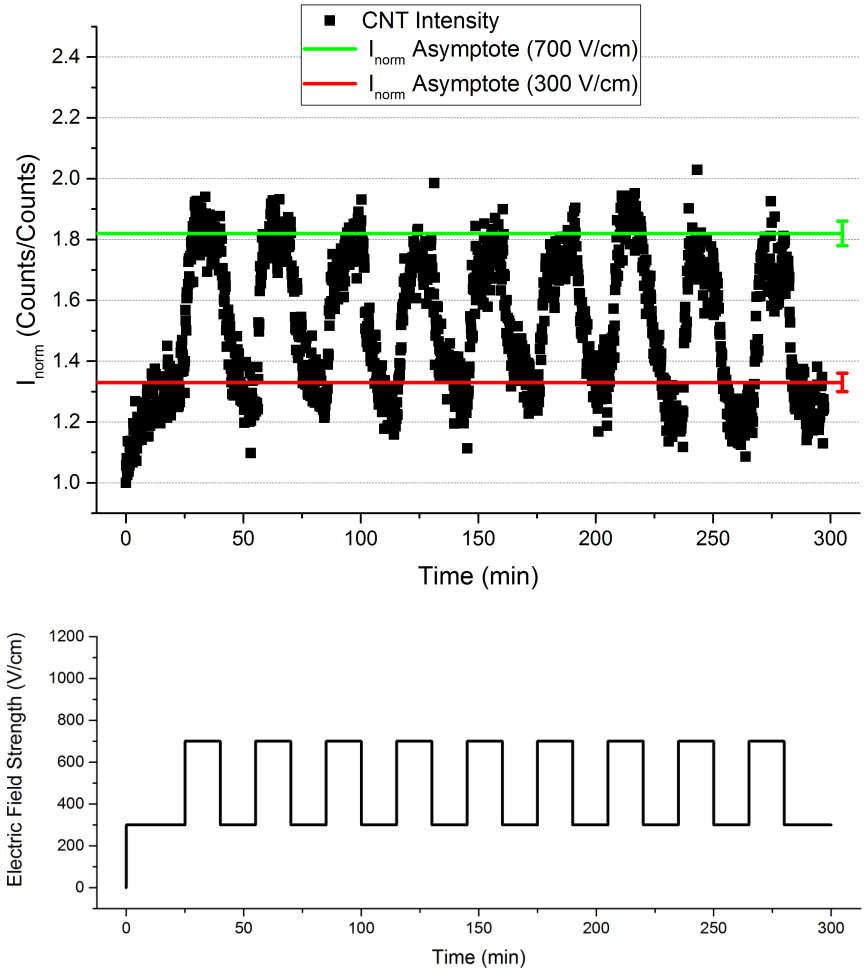

Figure 4.4 – The electric field was cycled between 300 V/cm and 700 V/cm as shown. I_{norm} values reproducibly reach the average asymptotes given by the solid lines with no obvious hysteresis.

AFM was conducted to determine the length distributions of the studied CNTs as a function of sonication energy. To take these measurements, CNTs were affixed to silicon substrates after the sonication process by drop casting. The CNT concentration (0.005 wt%) was low enough to avoid artificially creating bundles from CNT stacking during the evaporation process. A typical AFM image is shown in Figure 4.5 for a sonication energy of 100 kJ. Since CNTs lie flat along their lengths to maximize contact with the substrate, AFM height profiles correspond to the combined diameter of the CNT and any surfactant wrapped around its exterior. Surfactant wrapping will have a minimal effect on the overall length of the nanotube. Height profiles were between 1–2 nm, which match the diameter range of the manufacturer. The resultant CNT length distributions were fitted with log-normal functions (Figure 4.6). As sonication energy increases, the log-normal distributions narrow, and the average nanotube length decreases.

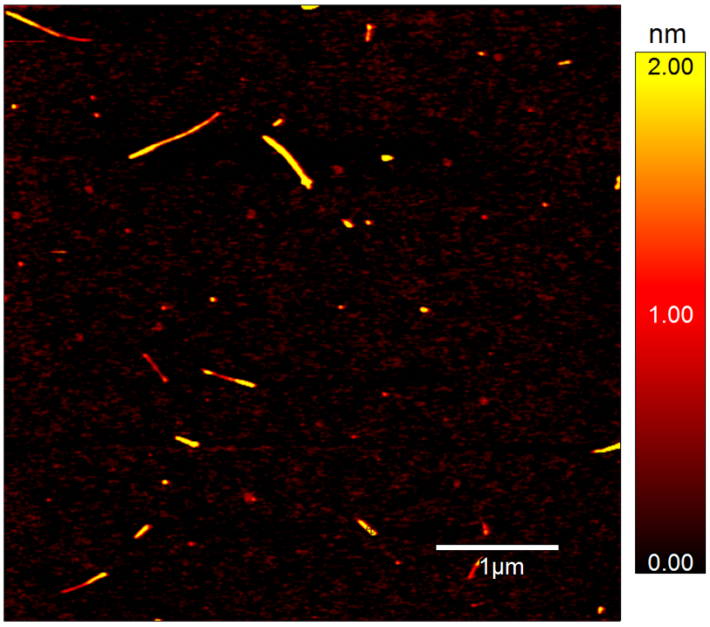

Figure 4.5 – AFM image of CNTs exposed to 100 kJ of sonication energy.

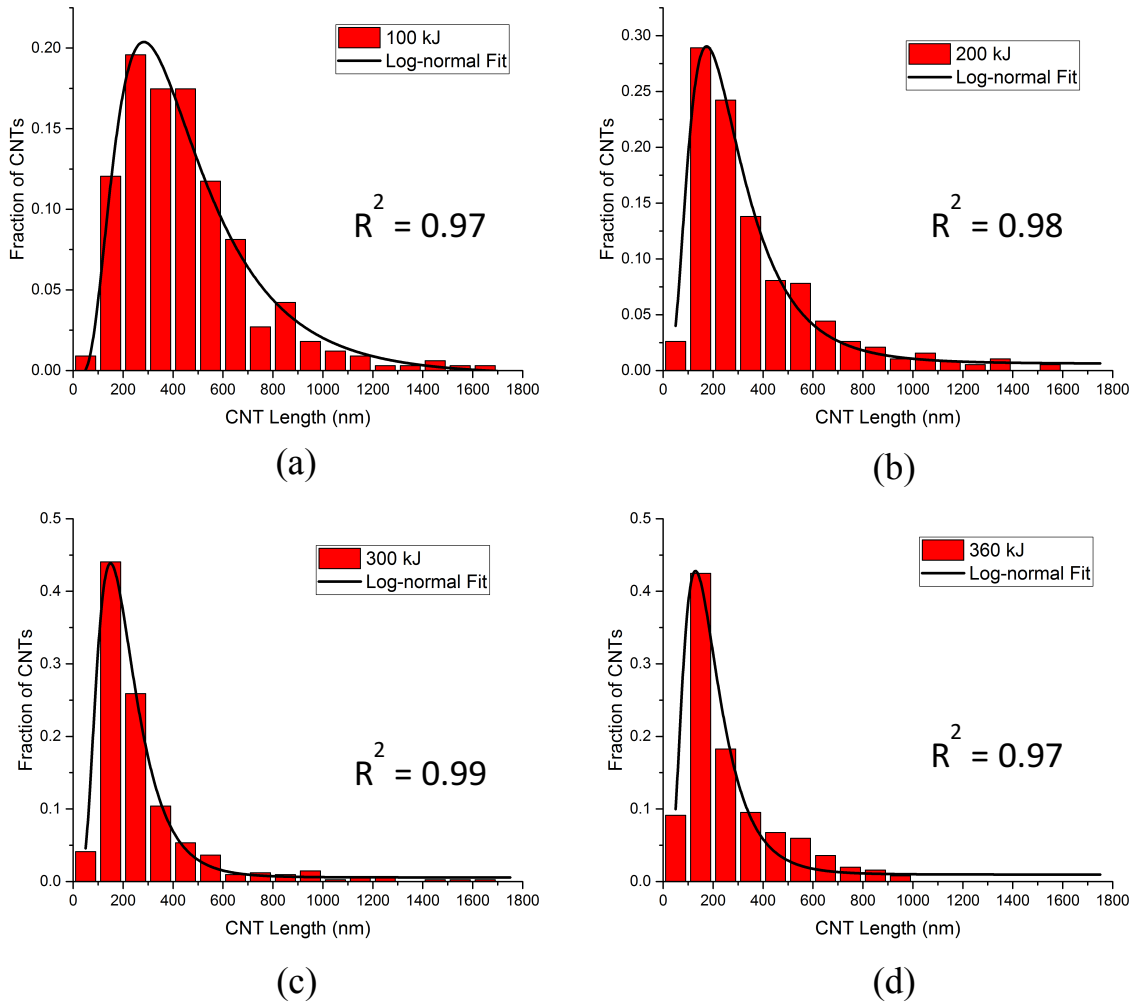

Figure 4.6 – CNT length distributions as determined by AFM for sonication energies of (a) 100 kJ, (b) 200 kJ, (c) 300 kJ, and (d) 360 kJ with R^2 values for the best-fit log-normal functions.

The effect of sonication energy on the asymptote of I_{norm} is presented in Figure 4.7. With increasing sonication energy, which corresponds to decreasing CNT length, the onset of a change in the measured G-band intensity shifts to higher electric field strengths. For the four sonication energies studied, the asymptotes of I_{norm} appear to converge for the higher electric field strengths ($E \geq 2500$ V/cm).

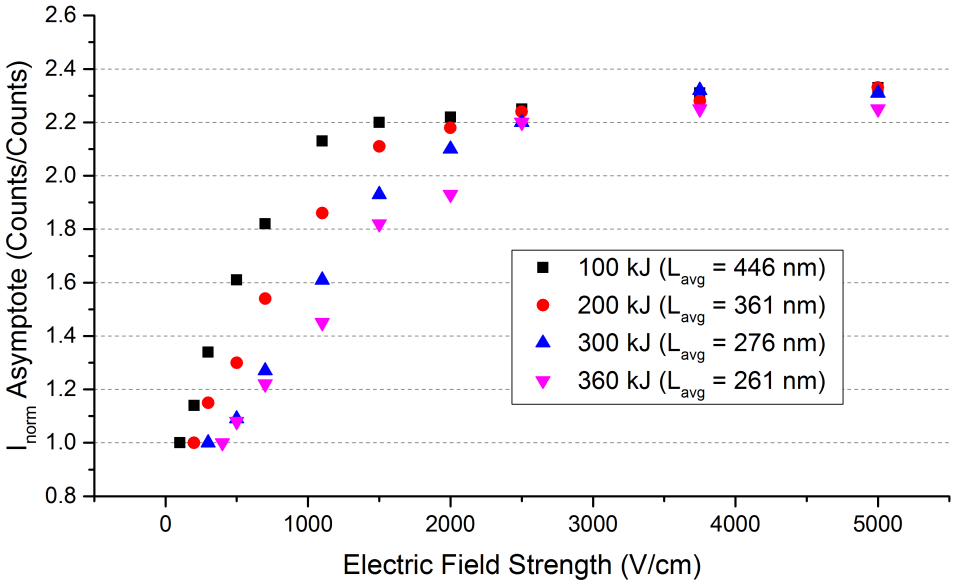

Figure 4.7 – The asymptote of I_{norm} as a function of electric field strength for different sonication energies.

4.5 Discussion

4.5.1 Length Dependence of CNT Alignment

Using polarized Raman spectroscopy, the intensity of characteristic CNT spectral features is shown to increase with electric field strength (Figure 4.2). The different asymptotic values are interpreted as discrete levels of alignment for different electric field strengths. The existence of discrete levels of alignment is further demonstrated in Figure 4.3. For the applied electric fields studied, a corresponding asymptote of I_{norm} is reproducibly achieved regardless of the previously applied field. The asymptote independence of the electric field history is further demonstrated in Figure 4.4, which shows no discernible hysteresis through nine cycles of electric field switching for the electric field strengths investigated. It is important to note that these trends may not apply to higher electric field strengths in which greater degrees of CNT translation may affect the degree of alignment.

To relate the discrete asymptotes of I_{norm} to different populations of CNTs aligning as a function of electric field strength, an electrostatic potential energy model is employed. The

electrostatic potential energy of a CNT is expected to demonstrate a length and electric field dependence according to

(4.4) $U_E \propto L^2 E^2$.

Thus, depending on the applied field strength, nanotubes of different lengths will possess the alignment energy necessary to overcome the thermal fluctuations of the system and induce alignment. As E increases, additional subsets of CNTs with shorter lengths will cross over the energy threshold necessary to generate alignment.

To test this hypothesis, samples with different CNT length distributions were created by applying different amounts of sonication energy during the dispersion process. The effect of sonication energy on distribution of CNT lengths was analyzed via AFM. As shown in Figure 4.6, the distributions narrow and shift to shorter average lengths with increasing sonication energy. The mean lengths determined from AFM follow a power law with respect to sonication energy with a power exponent of $m = 0.43$, which falls within the expected range ($0.4 \leq m \leq 0.5$) for short CNTs ($L < 1$ μm) [154]. Furthermore, the ratio of the D-band to G-band intensities—a qualitative indication of the degree of CNT damage [156]—remained roughly constant for the sonication energies studied.

The effects of CNT length on the observed alignment are shown in Figure 4.7. As sonication energy is increased, the average CNT length decreases. In accordance with the electrostatic potential energy model, the electric field threshold required to induce alignment shifts to higher field strengths as CNT length decreases. However, the values for the asymptotes of I_{norm} begin to converge at higher electric field strengths although the trend of decreasing alignment with increasing sonication remains. This observation is potentially explained through the length distributions generated from sonication. The larger fraction of shorter CNTs in the more highly sonicated samples require higher electric field strengths to align. Nonetheless, the similar levels of alignment at the higher values of E suggest most of the shortest CNTs produced from sonication still align at sufficiently high field strengths, and the less sonicated samples demonstrate diminishing returns in the measured CNT alignment at lower electric field strengths.

4.5.2 Electrostatic Potential Energy Best Fits

To relate the changes in the observed asymptotes for I_{norm} in Figure 4.7 to CNT length, a relationship between L and E was derived based on the electrostatic potential energy model. The

intensity of the CNT Raman signal as a function of electric field strength will be proportional to the sum of all CNT lengths for which $U_E > 2k_BT$, which can be written as

$$(4.5) \quad I(E) = A \int_{L_0}^{\infty} LP(L)dL$$

where L_0 is the minimum length for which a CNT will align, $P(L)$ is the probability distribution function (PDF) of CNT length for a given sonication energy, and A is a coefficient that depends on the number of CNTs within the excitation volume and the laser power. The PDFs of length (determined in Figure 4.6) are described by a log-normal distribution:

$$(4.6) \quad P(L) = \frac{B}{\sqrt{2\pi}\sigma L} e^{-\left(\ln\left(L/L_c\right)^2 / 2\sigma^2\right)},$$

where B is a coefficient, σ is the standard deviation of the function, and L_c is a parameter related to the peak center. The lower bound where the electric field alignment energy U_E is sufficient to overcome thermal randomization is determined by

$$(4.7) \quad U_E = \alpha L^2 E^2 \geq 2k_B T .$$

Thus, the minimum length necessary to induce alignment at a constant E is

$$(4.8) \quad L_0 = \frac{2}{E}\sqrt{\frac{k_B T}{\alpha}} .$$

Combining Eqs. (4.5), (4.6), and (4.8) results in

$$(4.9) \quad I(E) = C \int_{\frac{2}{E}\sqrt{\frac{k_B T}{\alpha}}}^{\infty} e^{-\left(\ln\left(L/L_c\right)^2 / 2\sigma^2\right)} dL ,$$

where C is a normalization coefficient that is dependent on the Raman intensity coefficient A as well as the length distribution function coefficient B and standard deviation σ.

Using Eq. (4.9), the change in I_{norm} as a function of electric field strength for the length distribution functions (as determined in Figure 4.6) is fit to the polarized Raman data in Figure 4.7, and the results are shown in Figure 4.8. The parameters C and α were fit to minimize the least squares difference between the experimental model and the calculated intensity from Eq. (4.9). The fitted polarizabilities α for each sonication energy were between 1.7–2.1·10^{-31} F·m^2,

which falls within the range determined for single-walled CNTs (10^{-28}–10^{-32} F·m^2) [70,71,75,98,106,157].

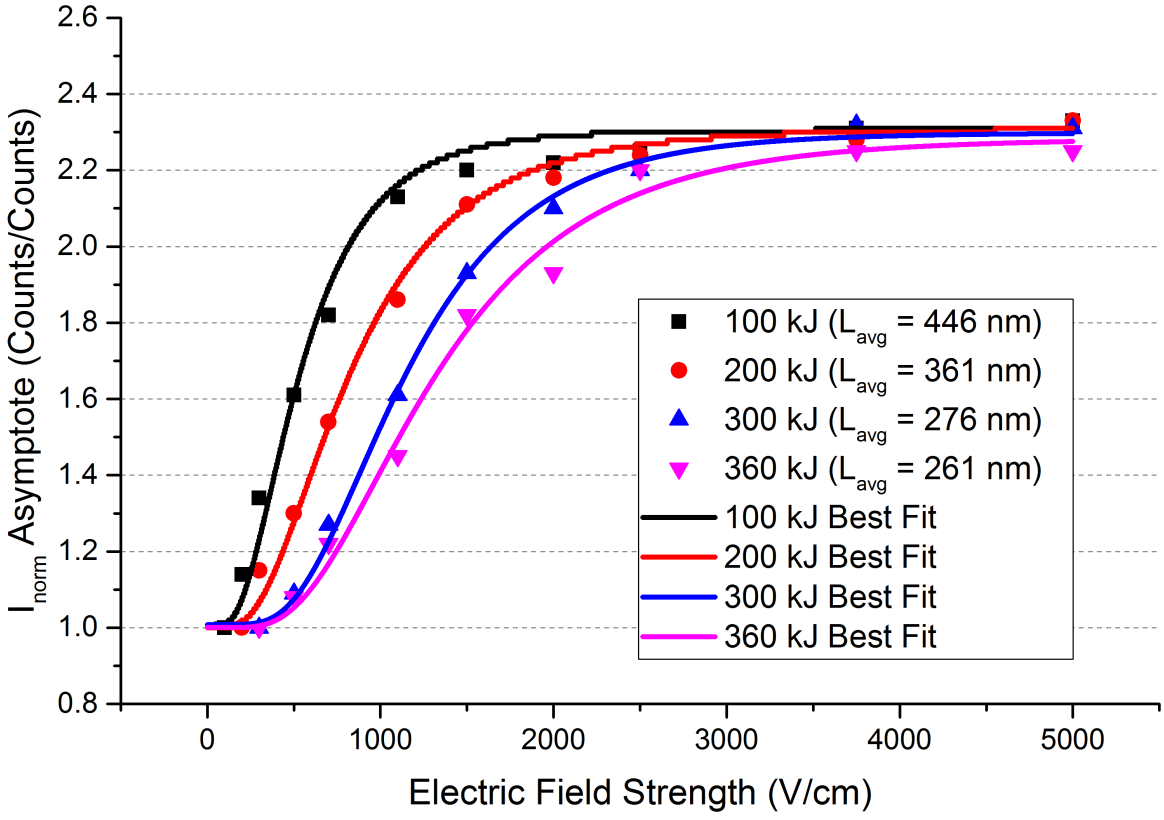

Figure 4.8 – Best fits for the experimental data in Figure 4.7 as calculated from Eq. (4.9). Fits were created using the log-normal length distribution functions determined in Figure 4.6.

The length dependence of CNT alignment induced by an electric field has important implications in the creation of aligned CNT composites and demonstrates the interconnected nature of the various processing steps for producing aligned composites. Dispersion processes such as sonication are necessary for the homogenous distribution of CNTs throughout the matrix. Higher sonication energy yields increased dispersion but also progressively shortens the CNTs. This in turn has a direct effect on the degree of electrostatically induced CNT alignment as shown herein. It is therefore imperative that the various processing steps be considered together during the manufacturing of nanocomposites.

4.5.3 Length Dependence on Speed of CNT Rotation

In addition to the length dependence of the degree of alignment, the speed of nanotube rotation will also depend on its length. It has been shown that the rotational friction (ζ_R) experienced by a CNT undergoing forced rotation in EPON 828 can be described by a continuum model [105] (see Chapter 3). Therefore, the rotational friction coefficient can be related to that of a thin rod [124,142] according to Eq. (3.7). At high aspect ratios, the rotational friction collapses to an L^3 dependence.

Based on the length dependence of the resistance, it follows that shorter tubes will rotate faster than longer ones. This prediction is verified by the data presented in Figure 4.3b. From the alignment energy model used here, progressively longer CNTs will unalign as the electric field strength is decreased. Thus, the nanotubes for which $U_E < 2k_BT$ as the electric field is reduced from 1100 V/cm to 700 V/cm will be shorter in length than those from 700 V/cm to 300 V/cm ($L|_{700\ \mathrm{V/cm}}^{1100\ \mathrm{V/cm}} < L|_{300\ \mathrm{V/cm}}^{700\ \mathrm{V/cm}}$). The time it takes I_{norm} to approach an asymptote (as determined by E) increases as E decreases, which corresponds to the slower rotational diffusivity of longer nanotubes.

4.6 Conclusions

From real-time, *in situ* polarized Raman spectroscopy measurements, the degree of electrostatically induced alignment of CNTs was shown to be a function of the applied electric field strength. It was theorized that the discrete levels of alignment achieved at different field strengths result from the length distributions of processed CNTs. This was confirmed in the observations of reduced degrees of alignment for more highly sonicated (shorter) CNTs. A mathematical description of the electric field-dependence of CNT polarized Raman intensity for different length distributions was created. Based on an electrostatic potential energy model, the best fits to experimental data yielded a polarizability of the studied single-walled CNTs on the order of 10^{-31} F·m^2, which agrees with reported literature values. The demonstrated length dependence of alignment has important implications in the creation of aligned structures. Due to the effects of growth and dispersion processes on nanotube length, all three steps need to be considered in parallel when producing aligned composites.

CHAPTER 5
ELECTROSTATIC ALIGNMENT OF CARBON NANOTUBES WITHIN CARBON FIBER COMPOSITES

5.1 Chapter Synopsis

Nanoparticle additions to carbon fiber reinforced plastics (CFRPs) are a growing area of polymer composite research. Controlling carbon nanotube alignment within the composite structure has the potential to take greater advantage of nanotube toughening and strengthening mechanisms. With applied electric fields, we show the ability to generate localized areas of increased electric field strength within the gaps between carbon fiber tows, which lead to increased levels of CNT alignment in those areas. These measurements have been correlated with COMSOL modeling. This finding could potentially lead to the development of CFRPs with CNT additions that selectively enhance the composite properties in the polymer matrix.

5.2 Introduction

A growing area of interest in nanotechnology is the control of nanoparticulate material to improve polymer composite mechanical and electrical properties [37,56,61,74,145,146]. One commonly employed method for manipulating carbon nanotubes in a polymer is with an applied electric field. By taking advantage of the anisotropy in their electric polarizability, it becomes possible to induce nanotube reorientation to create aligned arrays of CNTs [56]. Precise control of nanotube alignment is an important factor in creating nanocomposites with enhanced electrical and mechanical properties. Nevertheless, as composite research shifts toward the inclusion of nanoparticulate material, the industrial applications are limited outside a few niche products such as sporting goods and wind turbine blades [158]. The added material and processing costs [159] as well as the variability in the resulting composite properties [10] have prevented wide-spread, scaled-up manufacturing of CNT-polymer composites for structural applications.

Carbon fiber composites are replacing traditional materials in a variety of applications in the sports equipment, aerospace, and automotive industries. Small additions of CNTs to carbon

fiber reinforced plastics have been shown to improve toughening of the matrix by hindering the formation of cracks at the carbon fiber/matrix interface [160]. Furthermore, nanotube reinforcement aids in the resistance to delamination from crack propagation through a crack bridging mechanism of fiber pullout [161,162]. Although several reports find little to no benefit to the composite modulus from the addition of CNTs [160,162,163], the use of functionalized CNTs has been shown to improve the modulus of CFRPs [164]. Several reports also demonstrate that the inclusion of CNTs has a similar ameliorative effect on the toughness and modulus in glass fiber reinforced composites [28,165].

Due to their anisotropy, CNT orientation is an important factor in the resultant properties—such as interlaminar shear strength [166]—of hybrid composites. However, generating CNT alignment within a CFRP may prove difficult. Due to the rotational diffusivity of the particles, CNTs will unalign if the alignment force is not maintained during the curing process [62]. For resins requiring thermal cures, this phenomenon represents a limitation for mechanical shear alignment methods such as extrusion. Furthermore, alignment via magnetic fields has proven impractical for pristine nanotubes due to their low magnetic susceptibility [64,65]. Affixing ferromagnetic particles to the surface of CNTs has resulted in nanotube alignment at lower magnetic field strengths [53]. However, this method involves additional processing steps that affect the nanoparticle-matrix interface.

Electric fields have proven effective in aligning CNTs at electric potential gradients greater than ~100 V/cm [62] and have the advantage of being applied continuously during a curing process. Within a carbon fiber composite, an otherwise uniform electric field between two parallel plates is distorted near the conductive carbon fibers. This is due to the high conductivity of carbon fiber for which the potential drop across the fiber is essentially zero. Capitalizing on this phenomenon, this work demonstrates the ability to electrostatically align CNTs to different degrees within a carbon fiber composite, which offers the possibility of selectively enhancing specific parts of the composite structure.

5.3 Experimental

5.3.1 Materials

The materials, sample preparation, method of electrostatically inducing CNT alignment, and real-time polarized Raman spectroscopy measurements were conducted as described in

Chapter 2. A CNT concentration of 0.01 wt% was used for this chapter. Carbon fiber (HexTow AS4, 12,000 filament) was provided by the Hexcel Corporation. For the specimens created using carbon fiber, the unsized, untwisted tows were partitioned in half (~6,000 filaments) and cut into 10 mm segments. For the fiberglass composites, 5 wt% of chopped E-glass fibers (d = 13 μm, L = 6.4 mm) with silane sizing from Fibre Glast was added to the CNT-EPON 828 mixture and randomly dispersed by hand.

To create the polymerized specimens, the CNT-EPON 828 mixture was hand mixed with mPDA at a ratio of 7:1 by weight, cured at 75˚C for 2 hours, and post-cured at 125˚C for 2 hours. CNT alignment was induced with electric fields generated by an Agilent 33500B series waveform generator and a Trek model 2220 high voltage amplifier. All waveforms were sinusoidal with a frequency of 1 kHz. An electric potential of 900 V generated on parallel-plate aluminum electrodes with a 30-mm spacing was maintained throughout the cure and post-cure steps. Polymerized samples were ground to the carbon fiber tow mid-plane and polished to a 1200 grit finish.

5.3.2 COMSOL Modeling

Modeling was performed with COMSOL Multiphysics version 5.2a. Copper electrodes were modeled with a spacing of 30 mm. The length of the electrodes was made sufficiently long (greater than 10 times the electrode gap) so as to eliminate edge effects [167]. The electrodes were submerged in a dielectric medium with the material properties (viscosity, permittivity, and density) of EPON 828. Carbon fiber tows were approximated as cylinders with a length of 10 mm and a diameter of 1 mm; its material properties were provided by COMSOL. The carbon fiber tows were positioned halfway into the polymer, which had a height of 10 mm.

The electrostatics module was used to model the electric field throughout the EPON 828. A potential of 900 V was applied across the electrodes. An extremely fine mesh was used to divide the modeled components into 4,248,680 finite elements. From the computed results, mid-plane slices of electric field strength in the x-direction were taken. The relative electric field strength was computed by normalizing the calculated electric field at a given point to $E_0 = V/d_0$, where V is the applied potential on the parallel plates and d_0 is the distance of separation between them.

5.3.3 Characterization

Raman spectra were collected using a WITec alpha300 R Confocal Raman Microscope. A 532-nm laser was focused through a 10x objective at a power of 2 mW. The polarizations of incoming and scattered light were controlled via two wave plates and are denoted by HH or VV scattering geometries (where H is parallel to the electric field direction and V is perpendicular to it). In this notation, the first letter denotes the polarization of the incoming light and the second letter corresponds to the polarization of the scattered light. The ratio of the scattering intensities of orthogonally polarized light (denoted as the HH/VV ratio) is a metric often used to qualitatively assess the degree of CNT alignment with polarized Raman spectroscopy [115]. Scattered light was collected via backscattering, and the integration time per spectrum was 30 seconds. The prominent spectral features of the CNT-EPON 828 mixture from 1550–1650 cm^{-1} were fitted with Lorentzian functions as described previously [62]. The height of the Lorentzian centered at 1592 cm^{-1} was used as the G-band intensity. To compare spots tested at various points across the specimen, this value was normalized with respect to an EPON 828 spectral feature located at 824 cm^{-1} according to

$$\text{HH/VV} = \frac{I_{HH}^{1592}/I_{HH}^{824}}{I_{VV}^{1592}/I_{VV}^{824}} \tag{5.1}$$

where I_{xx}^{1592} is the intensity of the CNT G-band determined by the fitted Lorentzian height and I_{xx}^{824} is the intensity of the EPON spectral feature centered at 824 cm^{-1}; the polarization directions are denoted in the subscripts.

5.4 Results

5.4.1 COMSOL Maps

The relative electric field strength around conductive carbon fibers in an insulting polymer matrix was modeled using COMSOL, and the results are shown in Figure 5.1. For fiber tows oriented parallel to the electric field direction (Figures 5.1a–c), the COMSOL models predict regions of increased electric field strength near the fiber ends and decreased electric field strength along the length of the tows. The electric field strength within the conductive tows approaches zero. When the carbon fiber tows are oriented perpendicularly to the electric field direction (Figure 5.1d), small regions of increased electric field strength are expected along the lengths of the tows with small regions of decreased electric field strength at the tow ends.

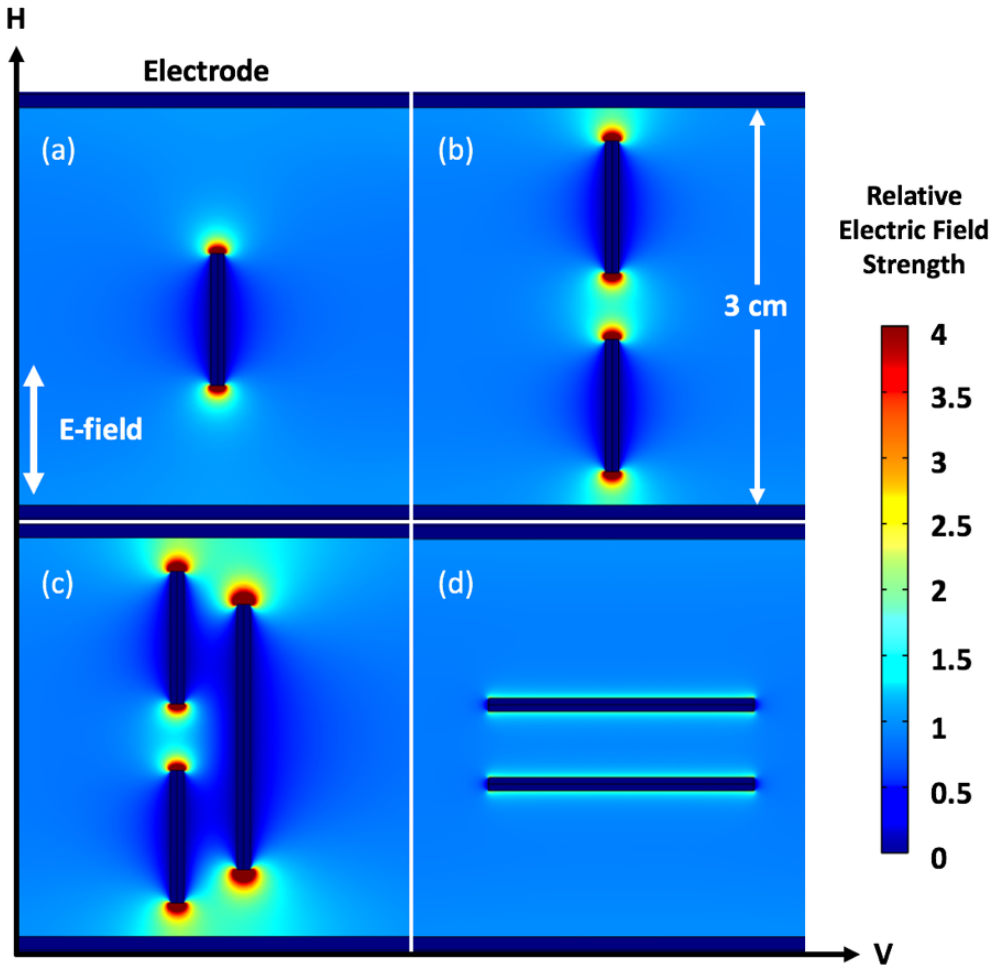

Figure 5.1 – COMSOL models for the expected relative electric field strengths around the various configurations of carbon fiber tows between two parallel-plate electrodes. The polarization directions for the Raman measurements (H and V) are noted.

5.4.2 Polarized Raman Spectroscopy

The degree of CNT alignment has been shown to be a function of electric field strength [62,168]. Polarized Raman measurements of an electrostatically aligned, polymerized CNT-EPON 828 specimen (without carbon fiber), yielded an average HH/VV ratio of 1.79 (standard deviation of 0.09), which is consistent with prior findings [62]. Although some scatter exists for these values, no obvious systemic trends in the HH/VV ratio based on location were observed (Figure 5.2) as is expected for a roughly uniform field between two parallel-plate electrodes. Similar results were observed for the tested polymerized plaques when E-glass fibers were incorporated into the matrix. This demonstrates that the non-conductive fibers had little impact on the degree of CNT alignment induced by an electric field.

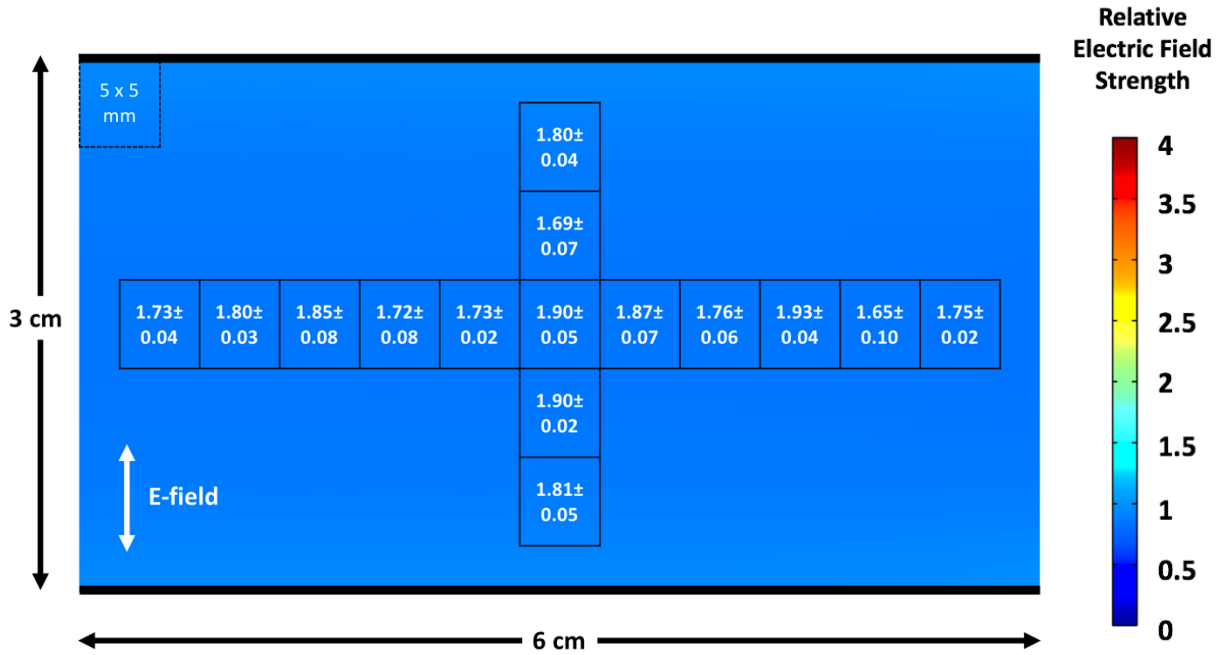

Figure 5.2 – HH/VV values calculated from the polarized Raman data overlaid with the COMSOL model of the relative electric field strength between the two parallel plate electrodes.

Aligned, cured composite plaques with carbon fiber tows were subsequently created. The COMSOL models shown in Figure 5.1 were generated to approximate the geometry of these plaques. Polarized Raman spectroscopy measurements made on the cured plaques are overlaid with the COMSOL models and presented in Figure 5.3. For a single carbon fiber tow (Figure 5.3a), HH/VV ratios increase near the end of the tow. Near the midpoint of the fiber tow, the HH/VV ratios are ~1. Moving away from the tow perpendicularly to its long axis, the HH/VV values approach the average ratio of 1.70 (standard deviation 0.06) for the plaque. For the two-tow system with a gap between them shown in Figure 5.3b, similar trends in the HH/VV ratios are seen. Larger increases in the HH/VV ratios are demonstrated in the tow gap than for the one-tow system in Figure 5.3a. Similar trends are observed in the three-tow system shown in Figure 5.3c. Increased HH/VV values are demonstrated in the tow gap near the fiber ends, and the regions between the two shorter tows and the longer parallel tow (but outside the tow gap) yield HH/VV values close to 1.

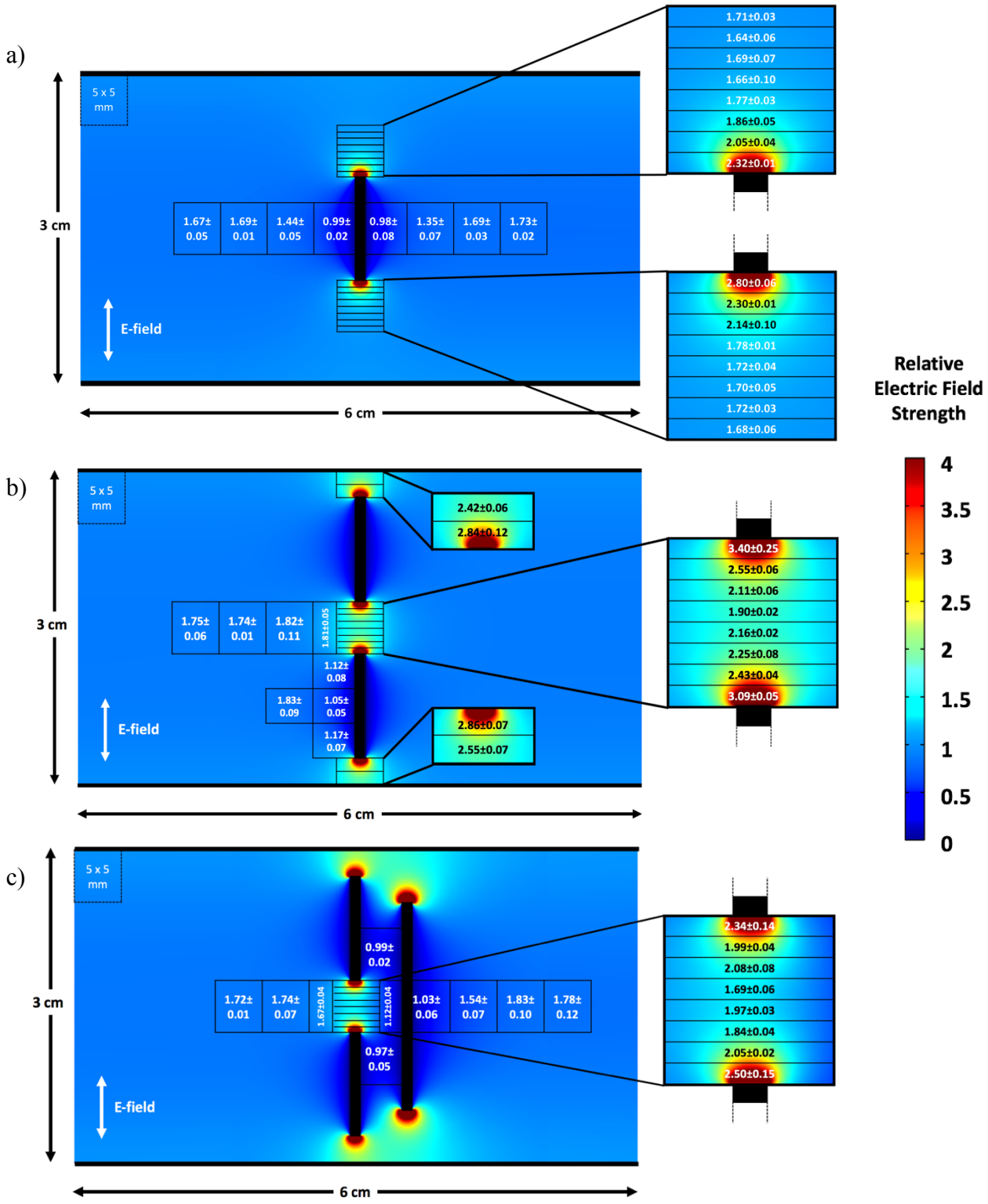

Figure 5.3 – COMSOL models for carbon fiber tows oriented parallel to the electric field direction overlaid with HH/VV values calculated from the polarized Raman data. Regions of interest near the tow ends are magnified on the right.

In Figure 5.4, two carbon fiber tows were oriented perpendicularly to the electric field direction. The regions of increased electric field strength are smaller and weaker than for the parallel systems shown in Figure 5.3. The polarized Raman data imply small increases in alignment in the vicinity of the fiber tows. HH/VV values for points midway between the parallel tows approximate those located away from the fibers where $E_0 = V/d_0$.

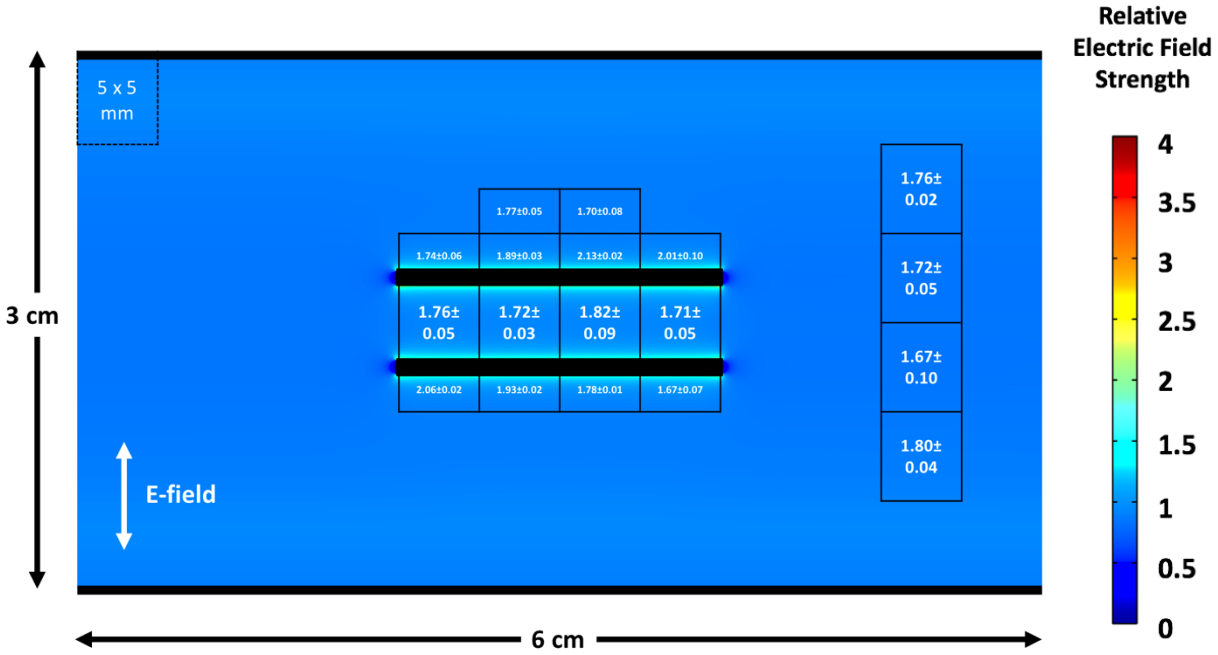

Figure 5.4 – COMSOL model for carbon fiber tows oriented perpendicularly to the electric field direction overlaid with HH/VV values calculated from the polarized Raman data. The polarized Raman spectra were collected for excitation volumes within 100 μm of the carbon fiber tows.

5.5 Discussion

The average degree of CNT alignment measured with polarized Raman spectroscopy on the polymerized plaques without carbon fibers matches that previously reported for alignment measurements made in real time in a polymer melt [62]. For the plaques that incorporate carbon fiber tows, the average HH/VV values for the regions where the electric field is negligibly influenced by the conductive fibers also closely match that for the systems without carbon fibers (Table 5.1). Furthermore, a similar level of alignment was also shown for CNT composites with randomly dispersed and oriented E-glass fibers. Due to their low electrical conductivity, the glass fibers did not significantly affect the electric field and the resulting electrostatically induced alignment of the nanotubes. It would therefore appear feasible to create electrostatically

aligned CNT/glass fiber polymer composites that take advantage of the strengthening and toughening effects of both types of reinforcement.

Table 5.1 – Average HH/VV values for the points sampled outside the regions when the electric field is influenced by the carbon fiber tows.

Specimen	Average HH/VV	Standard Deviation
No fibers	1.79	0.08
Glass fibers	1.79	0.10
One tow – parallel (Figure 5.3a)	1.70	0.06
Two tows – parallel (Figure 5.3b)	1.79	0.09
Three tows – parallel (Figure 5.3c)	1.74	0.10
Two tows – perpendicular (Figure 5.4)	1.74	0.07

For CNT/carbon fiber composites, spatial variations in the electric field strength exist. In response to the applied electric field, electrons redistribute within the conductive carbon fiber. This results in a buildup of charge on the fiber surface that cancels out the electric field within the fiber (i.e. $E = 0$) [169]. Local charge accumulations proportional to the number of free electrons that shift in response to the strength of the applied field lead to a differential electric field. Assuming a surface distribution of charge on the carbon fiber, the differential electric field is denoted by [169]

$$d\boldsymbol{E} = \widehat{\boldsymbol{R}}\frac{\rho_s}{4\pi\varepsilon_0 R^2}ds' \tag{5.2}$$

where $\widehat{\boldsymbol{R}}$ is the vector normal to the differential surface ds', ρ_s is the surface charge density, ε_0 is the permittivity of free space, and R is the distance from the surface s' (Figure 5.5). Integrating over the surface gives the total electric field strength at a distance R away from the surface according to

$$E = \frac{1}{4\pi\varepsilon_0}\int_{s'}\frac{\rho_s}{R^2}ds' \,. \tag{5.3}$$

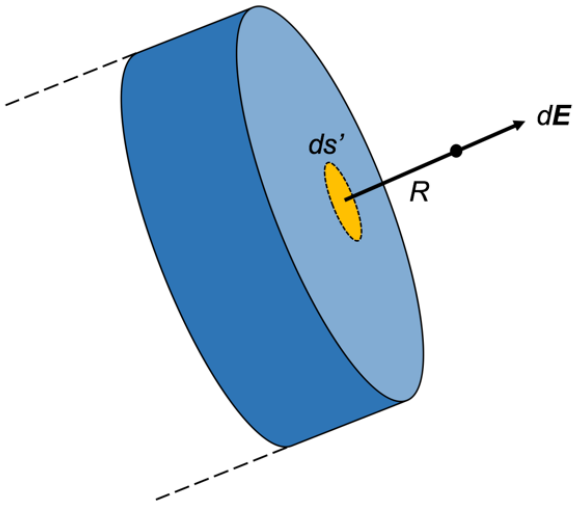

Figure 5.5 – Schematic detailing the differential electric field $d\boldsymbol{E}$ resulting from the differential surface *ds'* at a point a distance of *R* from the carbon fiber surface.

This results in localized regions of increased electric field strength near the tow ends for fibers parallel to the electric field direction (as seen in Figure 5.1a). These predictions are confirmed with polarized Raman data (Figure 5.3a) that demonstrate increased levels of alignment near the tow ends that decrease with distance to the alignment values expected for $E_0 = V/d_0$. Although the degree of CNT alignment in the vicinity of the tow ends is increased, it is lower than the alignment expected for the predicted electric field strengths as determined previously [62]. This could potentially result from the long electric field exposure times at elevated temperatures during the curing process. In addition to aligning, CNTs translate to form conductive networks in response to an applied electric field of sufficient magnitude [61], a phenomenon that would be exacerbated by the decreased composite viscosity. Furthermore, because of the spatially non-uniform electric field around the carbon fibers, the dielectrophoretic force will cause the CNTs to move to regions of higher or lower electric field strength depending on their polarizability [170,171]. These competing phenomena may explain the discrepancies between the expected alignment using the COMSOL model and that calculated from the polarized Raman measurements. Additional work may help to elucidate the observed discrepancies between these two measurements.

Carbon fiber-assisted CNT alignment in the gaps of discontinuous fibers (Figure 5.3b) may prove to be beneficial to the mechanical properties of the composite. In a CFRP, these

regions of the matrix are areas of load transfer in the polymer between fibers. CNTs aligned within these regions due to the enhanced local electric fields could selectively strengthen the polymer matrix where the carbon fibers do not reach. One potentially problematic issue with this idea could arise from the parallel, neighboring tows in a carbon fiber weave (Figure 5.3c). In this scenario, the regions of increased field strength near the tow ends and decreased field strength along the tow lengths are intersecting. However, increased alignment is still observed near the tow ends for the studied system in Figure 5.3c. Furthermore, the regions of increased field strength are still predicted to exist by COMSOL modeling for distances of separation between neighboring fibers down to the smallest modeled gaps of 0.2 tow diameters. This has not yet been experimentally verified.

Carbon fiber-assisted CNT alignment may also prove advantageous for nanotube orientations perpendicular to the tow direction. Selective alignment of CNTs between and perpendicular to carbon fibers may further enhance the toughening of the composite. "Stitching" these regions of the matrix with aligned CNTs may aid in resisting crack propagation more fully than for a random distribution. Another potential application for electrostatically aligned CNTs may be as interlaminar reinforcement. The interlaminar alignment of graphene nanoplatelets has been demonstrated by using conductive carbon fiber/epoxy laminae as electrodes [172]. Using this type of setup, it may be feasible to selectively induce CNT alignment normal to the carbon fiber laminae. Based on previous studies in hierarchical composites [173,174], CNT alignment in this direction is anticipated to resist delamination in a similar manner to z-pinning. These hypotheses all require experimental validation.

5.6 Conclusion

The effects of glass and carbon fibers on CNT alignment in a thermosetting epoxy resin via an electric field were studied. Glass fibers were determined to have no effect on the predicted and measured alignment of CNTs. For carbon fibers, regions of non-uniform electric field strength were modeled using COMSOL for various orientations of the conductive carbon fiber tows. Electrostatically induced CNT alignment within a cured epoxy plaque calculated from polarized Raman spectroscopy corroborated the models showing regions of increased and decreased electric field strength. In the development of hierarchical composites, selectively

aligning CNTs in certain locations within CFRPs offers a potential way to enhance specific mechanical properties.

Mechanical testing planned as future work will explore the potential improvements to the composite properties from the electrostatic alignment of CNTs. Microhardness testing is being used to probe the hardness of the composite based on the sample location relative to a carbon fiber tow. The feasibility of additional testing using ultrasound or Brillouin scattering is being investigated as methods to determine the composite modulus in these regions of interest.

Ultimately, the mechanical property enhancements achieved from the alignment of CNTs may be difficult to assess at the concentrations used in this study. Even with perfect CNT alignment and load transfer, the predicted increases in the composite modulus in the alignment direction from 0.01 wt% CNT additions (as used in this chapter) are ~3% as calculated from the rule of mixtures. Imperfect alignment will clearly decrease this expected value. Furthermore, due to the poor load transfer between non-functionalized CNTs and many polymer matrices, carbon fiber/CNT composites in several studies have shown little to no impact on the composite modulus from the inclusion of pristine CNT additions [160,162]. Since the functionalization of CNTs disrupts their electronic structure [12,27,28], pristine CNTs are required for alignment via electric fields.

For electrostatically induced alignment, the CNT concentration is limited from the low percolation threshold of rods. The percolation threshold (Φ_c) is roughly related to a rod's aspect ratio by $\Phi_c \sim d/L$ [175], and this relation has been extended to CNTs [176]. When applying an electric field, Φ_c decreases to even lower values due to the alignment and translations of CNT [177]. This process is often described as dynamic or kinetic percolation and restricts the CNT concentration to ~0.1% for CNTs where d is ~1 nm and L is ~1 μm. Above the percolation threshold, conductive CNT networks exist within the insulating polymer matrix. These networks hinder the application of electric fields with a parallel plate setup by freely conducting current through the material.

CHAPTER 6
CONCLUSIONS AND FUTURE WORK

Due to large anisotropy of high aspect ratio carbon nanotubes, the mechanical and electrical properties of CNT-polymer composites will depend in part on the degree and direction of CNT alignment. With the lack of data on CNT alignment dynamics in polymers taken in real time, this thesis sought to develop a real-time technique for assessing CNT alignment in a polymer for composite applications. It was determined that polarized Raman spectroscopy was well suited for these measurements because spectra can be taken *in situ* and non-destructively during the alignment process, distinguish CNT spectral features at low concentrations from the polymer matrix, and have integration times relevant to the kinetics of nanotube alignment.

With this real-time, *in situ* polarized Raman spectroscopy technique, analyses can be made of the many factors affecting the degree and speed of electrostatically induced alignment in a polymer. Predictions of faster alignment at higher field strengths (due to an increased electrostatic torque) were confirmed with real-time measurements. As another advantage of this technique, measurements were taken on aligned samples after the removal of the applied electric field. The decrease in the polarized CNT signal was interpreted as the loss of alignment from the rotational diffusion of the nanoparticles. It is therefore imperative that CNT alignment be fixed in place (through a polymerization process in a thermoset, by dropping below the T_g in a thermoplastic melt, etc.) before removing the aligning force. This notion extends to other methods of alignment including magnetic fields and mechanical shear.

The effects of polymer viscosity were also investigated, and it was found that the rotational mobility of the CNTs in this study followed a continuum model (i.e. the rotational friction is directly proportional to the composite melt viscosity). Consequently, with knowledge of the temperature dependence of the melt viscosity, the speed of the alignment process can be controlled through the temperature of the mixture. This information is potentially beneficial when the alignment process is the rate-dependent step.

CNT length was determined to be another important parameter in the degree and speed of electrostatically induced alignment. The discovery of different asymptotes in the polarized Raman intensity of CNT spectral features as a function of the applied electric field strength was interpreted as discrete levels of CNT alignment. Using an electrostatic potential energy model, distinct and reproducible asymptotes were shown to be a result of the length distributions of the dispersed CNTs. The implications of this finding demonstrate the importance of considering all processing conditions when creating aligned CNT-polymer composites with enhanced properties. Ongoing work also intends to study the effects of the intrinsic polarizability of a nanotube on its alignment under an applied electric field.

CNT alignment within a carbon fiber composite was also considered. Based on COMSOL modeling, regions of increased relative electric field strength were predicted to exist near the conductive carbon fibers depending on their orientation with respect to the electric field direction. These predictions were corroborated with polarized Raman spectroscopy measurements that showed trends in the observed alignment consistent with the models. The advantages of selectively aligning CNTs based on their location relative to carbon fibers was discussed in terms of their toughening and strengthening mechanisms. Ongoing work seeks to determine the impact of this alignment on the resultant composite mechanical properties.

Based on the findings presented in this thesis and in related works [56,61,74,145], it appears that the alignment of CNTs with electric fields may prove more beneficial for electrical applications. The ability to manipulate CNTs into higher order structures and separate them based on chirality by using their dielectrophoretic mobility seem particularly useful for the electronics and semiconductor industries. Because of the deleterious effects of functionalization on the electronic structure of a CNT, electrostatically induced alignment of functionalized CNTs is extremely limited. This requires the use of pristine nanotubes for alignment under applied electric fields. Since pristine CNTs typically bond weakly with most polymer matrices, this requirement sacrifices the matrix-CNT interface. The load transfer through the interface is crucial to most mechanical properties and will therefore restrict the use of electric fields in the creation of aligned CNT-polymer composites for structural applications. However, ongoing work performed by colleagues is currently analyzing CNT alignment dynamics using magnetic fields and mechanical shear, which do not necessarily preclude nanotube functionalization.

Nonetheless, mechanical testing is presently being performed to test the effects of increased CNT alignment near carbon fiber tows. To further investigate the feasibility of applying this technique to CFRPs, woven carbon fiber laminates with electrostatically aligned CNTs will need to be created. Testing for potential improvements to composite toughness or interlaminar shear strength should indicate the impact of selectively aligning CNTs in these regions. Brillouin scattering may also be an effective tool for these analyses since it has been used previously to measure the modulus of carbon fiber-reinforced polymer composites [108]. The experimental setup of Brillouin spectroscopy also shares many of the same advantages of Raman spectroscopy in non-destructively testing specimens with high spot size resolution.

For assessing the compatibility of the reinforcing CNTs with the polymer matrix, Raman spectroscopy has proven to be a viable technique. By monitoring shifts in the spectral center of the CNT 2D-band (Figure 1.4a), load transfer between the matrix and the CNTs can be quantified. It has been shown that straining the lattice of CNTs either in tension or compression results in a frequency shift of the 2D-band [178–182]. A comparison of this shift to the known strain of the material can thus give an indication of the degree of load transfer.

Expanding on the work in Chapter 3, valuable insight could be gained concerning the mobility of CNTs dispersed in larger polymers where $R_g > d_{CNT}$. In these systems, CNTs may show deviations from microscale diffusion behavior similar to other studied nanorods [144,183]. While the longitudinal translational mobility of CNTs (Figure 3.2) may be expected to show these deviations, we believe that CNT rotation may be more akin to its transverse translation in which the length is the dimension of import. At this scale, a continuum model would accurately describe CNT rotation in most polymers, and the speed of rotation would be inversely proportional to the composite viscosity. Additional experiments are needed to test and confirm this hypothesis.

One advantage of Raman spectroscopy that was not explored in this thesis is the capability of resolving nanotube chirality based on the excitation source. The resonant Raman scattering from CNTs—which occurs when the excitation energy is near an optical transition of an individual nanotube—depends on the chosen laser wavelength [184–188]. Since resonance scattering is significantly stronger than the non-resonant contributions [104,188] (determined to magnify the intensity by a factor of $\sim 10^3$ [189]), the resulting spectral profile will depend heavily on the wavelength of light used.

This phenomenon is proving potentially useful in current work that is aimed at investigating the effects of nanotube polarizability on the degree and speed of electrostatically induced alignment. By testing samples with high purity s-SWCNTs, the alignment of semiconducting CNTs appears to match that reported for the as-produced (2 s-SWCNT:1 m-SWCNT) CNTs used in this thesis. The ability to align s-SWCNTs at the studied field strengths seems to contradict several previous reports that either assume [75], predict [171], or observe [70,190] weak to no alignment of s-SWCNTs as compared to m-SWCNTs under applied electric fields. The similarities between the time-intensity Raman data (i.e. Figure 2.7b) for the bulk CNTs and high purity s-SWCNTs lead to the working hypothesis that the resonant contributions from s-SWCNTs are dominant for this system at a 532-nm excitation wavelength.

For high purity m-SWCNT samples, a wavelength of 785 nm appears to be in resonance with the M_{11} bandgap [185], the first optical transition for m-SWCNTs, for the diameter range of the studied CNTs [191] based on the shape of the observed G-bands [192]. Initial results from real-time polarized Raman spectroscopy measurements appear to show m-SWCNT alignment at electric fields at least an order of magnitude lower in strength. Since the polarizabilities of metallic CNTs are predicted to be several orders of magnitude greater than those of semiconducting CNTs of similar lengths [70,71], this finding would seem to be consistent with the electrostatic potential energy model used for this thesis. Additional work is required to confirm these observations.

Outside the numerous possibilities provided by polarized Raman spectroscopy, a variety of other techniques offer novel approaches to studying CNT processing for composite applications. *In situ* TEM of CNT alignment in a solution or a polymer melt is one example. As electron transparent, hermetically sealed liquid cells for TEM analyses grow in popularity, researchers now possess a tool for conducting thermal and electrical testing *in situ* with potentially sub-nanometer resolution [193]. Several studies on nanoparticle mobility [194] and assembly [195,196] in solution as well as observations from applied electric biasing [197] have already been conducted. Similar to previous studies of electrostatically induced nanowire rotation with optical microscopy [198–201], the real-time observation of CNT alignment in solution or in a polymer melt under an applied electric field using TEM now appears feasible.

However, future work in this direction would need to address several issues. The dimensions of the liquid cell compared to the nanotubes is one example. The thickness of the

liquid cell is limited by the electron transparency of the suspending medium. Gold nanoparticles have been imaged through ~3.3 μm of water [202], but for particles dispersed in polymers, sample thickness is typically closer to ~100–200 nm. Furthermore, the resolution decreases as the thickness of the material increases due to the scattering of electrons. Another limitation arising from the dimensions of the liquid cell is the preponderance of fringe effects. As sample volume decreases, the behavior of a larger percentage of the material depends on its interactions with the interface. These interactions have been shown to impact the rates of nanoparticle diffusion [193] and nanorod motion from local convective flow and capillary forces [194]. The electron beam itself can also affect the sample. Bubble formation has been observed in solution [203], and the effects of local heating in polymers from focused electron beams [32] could also potentially distort measurements of nanoparticle mobility. These problems would need to be resolved before accurate data could be collected on CNT alignment with *in situ* TEM measurements.

Dynamic AFM methods also appear promising for capturing imbedded nanotube alignment with nanoscale resolution. Sub-surface imaging of CNTs has been demonstrated in polymer films with a thickness of ~30 μm [80]. Due to the difference between the dielectric constant of the nanotubes and the polymer matrix, spatial variations of the capacitance gradient exist and can be used to image imbedded single-walled CNTs with amplitude modulated AFM [80]. With this technique, it may also be possible to differentiate s-SWCNTs and m-SWCNTs based on their different electrical properties. If successful, these measurements could be used to explore the differences in electrostatically induced alignment of CNTs based on chirality.

Nanotube dispersion was another source of variability that was explored but not expanded on in this thesis. Several techniques exist for qualitatively assessing the state of CNT dispersion including small angle neutron scattering [204,205], rheological measurements [125,206], the PL intensity from isolated CNTs [91–93], and the Raman "roping" peak [207–209]. Excluding extensive TEM work, dynamic light scattering (DLS) may be one of the few ways to quantitatively characterize the nanoscale dispersion of CNTs in a polymer. By modeling CNTs as rigid rods, depolarized DLS has been used to non-destructively determine the mean length and diameter of individually dispersed single-walled CNTs in solution based on the calculated rotational and translational diffusion coefficients determined from autocorrelation functions of the experimentally produced speckle patterns [210,211]. These findings were reproduced but not

investigated extensively for the system used in this thesis. To avoid multiple scattering events, there is a limitation on the CNT concentration (0.0005 wt% was found to work well in solution and in EPON 828). Furthermore, because these light scattering measurements are sensitive to CNT agglomerates, it is important to confirm the existence of isolated nanotubes with a complimentary technique such as TEM. Since many polymers are optically transparent at certain wavelengths of light, DLS may prove to be an effective tool for investigating nanoparticle dispersion within these systems. Ultimately, all factors of composite property variability will need to be considered to create CNT-polymer composites with enhanced properties.

BIBLIOGRAPHY

[1] C. Soutis, Carbon fiber reinforced plastics in aircraft construction, Mater. Sci. Eng. A. 412 (2005) 171–6. doi:10.1016/j.msea.2005.08.064.

[2] T. Windhorst, G. Blount, Carbon-carbon composites: a summary of recent developments and applications, Mater. Des. 18 (1997) 11–5. doi:10.1016/S0261-3069(97)00024-1.

[3] R. Rafiee, M. Heidarhaei, Investigation of chirality and diameter effects on the Young's modulus of carbon nanotubes using non-linear potentials, Compos. Struct. 94 (2012) 2460–2464. doi:10.1016/j.compstruct.2012.03.010.

[4] A. Krishnan, E. Dujardin, T.W. Ebbesen, P.N. Yianilos, M.M.J. Treacy, Young's modulus of single-walled nanotubes, Phys. Rev. B. 58 (1998) 14013–14019.

[5] T.W. Tombler, C. Zhou, L. Alexseyev, J. Kong, H. Dai, L. Liu, et al., Reversible electromechanical characteristics of carbon nanotubes under local-probe manipulation, Nature. 405 (2000) 769–772.

[6] T. Chatterjee, C.A. Mitchell, V.G. Hadjiev, R. Krishnamoorti, Hierarchical Polymer–Nanotube Composites, Adv. Mater. 19 (2007) 3850–3. doi:10.1002/adma.200700765.

[7] S.H. Jin, Y.-B. Park, K.H. Yoon, Rheological and mechanical properties of surface modified multi-walled carbon nanotube-filled PET composite, Compos. Sci. Technol. 67 (2007) 3434–41. doi:10.1016/j.compscitech.2007.03.013.

[8] H. Xia, M. Song, Preparation and characterisation of polyurethane grafted single-walled carbon nanotubes and derived polyurethane nanocomposites, J. Mater. Chem. 16 (2006) 1843–51. doi:10.1039/b601152g.

[9] F. Gojny, M. Wichmann, B. Fiedler, K. Schulte, Influence of different carbon nanotubes on the mechanical properties of epoxy matrix composites – A comparative study, Compos. Sci. Technol. 65 (2005) 2300–13. doi:10.1016/j.compscitech.2005.04.021.

[10] Z. Spitalsky, D. Tasis, K. Papagelis, C. Galiotis, Carbon nanotube–polymer composites: Chemistry, processing, mechanical and electrical properties, Prog. Polym. Sci. 35 (2010) 357–401. doi:10.1016/j.progpolymsci.2009.09.003.

[11] Y.S. Song, J.R. Youn, Influence of dispersion states of carbon nanotubes on physical properties of epoxy nanocomposites, Carbon N. Y. 43 (2005) 1378–85. doi:10.1016/j.carbon.2005.01.007.

[12] P.-C. Ma, N.A. Siddiqui, G. Marom, J.-K. Kim, Dispersion and functionalization of carbon nanotubes for polymer-based nanocomposites: A review, Compos. Part A. 41 (2010) 1345–1367. doi:10.1016/j.compositesa.2010.07.003.

[13] L. Liu, H.D. Wagner, Rubbery and glassy epoxy resins reinforced with carbon nanotubes, Compos. Sci. Technol. 65 (2005) 1861–1868. doi:10.1016/j.compscitech.2005.04.002.

[14] X.-L. Gao, K. Li, A shear-lag model for carbon nanotube-reinforced polymer composites, Int. J. Solids Struct. 42 (2005) 1649–1667. doi:10.1016/j.ijsolstr.2004.08.020.

[15] K. Lau, Interfacial bonding characteristics of nanotube/polymer composites, Chem. Phys. Lett. 370 (2003) 399–405. doi:10.1016/S0009-2614(03)00100-3.

[16] Y. Liu, X. Chen, Evaluations of the effective material properties of carbon nanotube-based composites using a nanoscale representative volume element, Mech. Mater. 35 (2003) 69–81. doi:10.1016/S0167-6636(02)00200-4.

[17] Y.L. Chen, B. Liu, X.Q. He, Y. Huang, K.C. Hwang, Failure analysis and the optimal toughness design of carbon nanotube-reinforced composites, Compos. Sci. Technol. 70 (2010) 1360–1367. doi:10.1016/j.compscitech.2010.04.015.

[18] Z. Yao, N. Braidy, G.A. Botton, A. Adronov, Polymerization from the surface of single-walled carbon nanotubes - preparation and characterization of nanocomposites., J. Am. Chem. Soc. 125 (2003) 16015–24. doi:10.1021/ja037564y.
[19] T. Ramanathan, S. Stankovich, D.A. Dikin, H. Liu, H. Shen, S.T. Nguyen, et al., Graphitic nanofillers in PMMA nanocomposites—An investigation of particle size and dispersion and their influence on nanocomposite properties, J. Polym. Sci. Part B Polym. Phys. 45 (2007) 2097–2112. doi:10.1002/polb.21187.
[20] P. Rittigstein, R.D. Priestley, L.J. Broadbelt, J.M. Torkelson, Model polymer nanocomposites provide an understanding of confinement effects in real nanocomposites., Nat. Mater. 6 (2007) 278–82. doi:10.1038/nmat1870.
[21] C. Richard, F. Balavoine, P. Schultz, T.W. Ebbesen, C. Mioskowski, Supramolecular Self-Assembly of Lipid Derivatives on Carbon Nanotubes, Science. 300 (2003) 775–8. doi:10.1126/science.1080848.
[22] P.C. Ma, J.-K. Kim, B.Z. Tang, Effects of silane functionalization on the properties of carbon nanotube/epoxy nanocomposites, Compos. Sci. Technol. 67 (2007) 2965–2972. doi:10.1016/j.compscitech.2007.05.006.
[23] S. Wang, R. Liang, B. Wang, C. Zhang, Load-transfer in functionalized carbon nanotubes/polymer composites, Chem. Phys. Lett. 457 (2008) 371–375. doi:10.1016/j.cplett.2008.04.037.
[24] A. Garg, S.B. Sinnott, Effect of chemical functionalization on the mechanical properties of carbon nanotubes, Chem. Phys. Lett. 295 (1998) 273–278.
[25] C.C. Ling, Q.Z. Xue, X.Y. Zhou, Mechanical properties of functionalized carbon nanotube as reinforcements, Adv. Compos. Mater. Manuf. Eng. 583 (2012) 22–26. doi:DOI 10.4028/www.scientific.net/AMR.583.22.
[26] G. Yamamoto, J.W. Suk, J. An, R.D. Piner, T. Hashida, T. Takagi, et al., The influence of nanoscale defects on the fracture of multi-walled carbon nanotubes under tensile loading, Diam. Relat. Mater. 19 (2010) 748–751. doi:10.1016/j.diamond.2010.01.045.
[27] S. Wang, Functionalization of carbon nanotubes: Characterization, modeling and composite applications, Florida State University, 2006. http://diginole.lib.fsu.edu/islandora/object/fsu%3A175802.
[28] J. Qiu, C. Zhang, B. Wang, R. Liang, Carbon nanotube integrated multifunctional multiscale composites, Nanotechnology. 18 (2007) 275708–275719. doi:10.1088/0957-4484/18/27/275708.
[29] S.L. Mielke, D. Troya, S. Zhang, J.L. Li, S. Xiao, R. Car, et al., The role of vacancy defects and holes in the fracture of carbon nanotubes, Chem. Phys. Lett. 390 (2004) 413–420. doi:10.1016/j.cplett.2004.04.054.
[30] K.L. Lu, R.M. Lago, Y.K. Chen, M.L.H. Green, P.J.F. Harris, S.C. Tsang, Mechanical Damage of Carbon Nanotubes by Ultrasound, Carbon N. Y. 33 (1996) 814–6.
[31] F. Inam, T. Vo, J.P. Jones, X. Lee, Effect of carbon nanotube lengths on the mechanical properties of epoxy resin: An experimental study, J. Compos. Mater. 47 (2013) 2321–2330. doi:10.1177/0021998312457198.
[32] D. Qian, E.C. Dickey, R. Andrews, T. Rantell, Load transfer and deformation mechanisms in carbon nanotube-polystyrene composites, Appl. Phys. Lett. 76 (2000) 2868. doi:10.1063/1.126500.
[33] A. Hernández-Pérez, F. Avilés, A. May-Pat, A. Valadez-González, P.J. Herrera-Franco, P. Bartolo-Pérez, Effective properties of multiwalled carbon nanotube/epoxy composites

using two different tubes, Compos. Sci. Technol. 68 (2008) 1422–1431. doi:10.1016/j.compscitech.2007.11.001.
[34] S.Y. Fu, Z.K. Chen, S. Hong, C.C. Han, The reduction of carbon nanotube (CNT) length during the manufacture of CNT/polymer composites and a method to simultaneously determine the resulting CNT and interfacial strengths, Carbon N. Y. 47 (2009) 3192–3200. doi:10.1016/j.carbon.2009.07.028.
[35] F.M. Blighe, K. Young, J.J. Vilatela, A.H. Windle, I.A. Kinloch, L. Deng, et al., The Effect of Nanotube Content and Orientation on the Mechanical Properties of Polymer-Nanotube Composite Fibers: Separating Intrinsic Reinforcement from Orientational Effects, Adv. Funct. Mater. 21 (2011) 364–371. doi:10.1002/adfm.201000940.
[36] X. Zhao, L. Ye, Structure and properties of highly oriented polyoxymethylene/multi-walled carbon nanotube composites produced by hot stretching, Compos. Sci. Technol. 71 (2011) 1367–1372. doi:10.1016/j.compscitech.2011.05.011.
[37] J. Severino, J. Yang, L. Carlson, R. Hicks, Progression of alignment in stretched CNT sheets determined by wide angle X-ray scattering, Carbon N. Y. 100 (2016) 309–317. doi:10.1016/j.carbon.2016.01.005.
[38] A.A. Mamedov, N.A. Kotov, M. Prato, D.M. Guldi, J.P. Wicksted, A. Hirsch, Molecular design of strong single-wall carbon nanotube/polyelectrolyte multilayer composites., Nat. Mater. 1 (2002) 190–4. doi:10.1038/nmat747.
[39] B.S. Shim, Z. Tang, M.P. Morabito, A. Agarwal, H. Hong, N.A. Kotov, Integration of conductivity, transparency, and mechanical strength into highly homogeneous layer-by-layer composites of single-walled carbon nanotubes for optoelectronics, Chem. Mater. 19 (2007) 5467–74. doi:10.1021/cm070442a.
[40] M. Ichida, S. Mizuno, H. Kataura, Y. Achiba, A. Nakamura, Anisotropic optical properties of mechanically aligned single-walled carbon nanotubes in polymer, Appl. Phys. A Mater. Sci. Process. 78 (2004) 1117–1120. doi:10.1007/s00339-003-2462-4.
[41] L. Jin, C. Bower, O. Zhou, Alignment of carbon nanotubes in a polymer matrix by mechanical stretching, Appl. Phys. Lett. 73 (1998) 1197–1199. doi:10.1063/1.122125.
[42] A.G. Rozhin, Y. Sakakibara, H. Kataura, S. Matsuzaki, K. Ishida, Y. Achiba, et al., Anisotropic saturable absorption of single-wall carbon nanotubes aligned in polyvinyl alcohol, Chem. Phys. Lett. 405 (2005) 288–293. doi:10.1016/j.cplett.2005.02.049.
[43] J.A. Fagan, J.R. Simpson, B.J. Landi, L.J. Richter, I. Mandelbaum, V. Bajpai, et al., Dielectric Response of Aligned Semiconducting Single-Wall Nanotubes, Phys. Rev. Lett. 98 (2007) 147402. doi:10.1103/PhysRevLett.98.147402.
[44] R. Haggenmueller, H.H. Gommans, A.G. Rinzler, J.E. Fischer, Aligned single-wall carbon nanotubes in composites by melt processing methods, Chem. Phys. Lett. 330 (2000) 219–25.
[45] D. Fischer, P. Pötschke, H. Brünig, A. Janke, Investigation of the Orientation in Composite Fibers of Polycarbonate with Multiwalled Carbon Nanotubes by Raman Microscopy, Macromol. Symp. 230 (2005) 167–172. doi:10.1002/masy.200551156.
[46] P.M. Ajayan, O. Stephan, C. Colliex, D. Trauth, Aligned carbon nanotube arrays formed by cutting a polymer resin--nanotube composite., Science. 265 (1994) 1212–4. doi:10.1126/science.265.5176.1212.
[47] J.R. Wood, Q. Zhao, H.D. Wagner, Orientation of carbon nanotubes in polymers and its detection by Raman spectroscopy, Compos. Part A Appl. Sci. Manuf. 32 (2001) 391–399. doi:10.1016/S1359-835X(00)00105-6.

[48] S. Shoji, H. Suzuki, R. Zaccaria, Z. Sekkat, S. Kawata, Optical polarizer made of uniaxially aligned short single-wall carbon nanotubes embedded in a polymer film, Phys. Rev. B. 77 (2008) 153407. doi:10.1103/PhysRevB.77.153407.
[49] D.A. Walters, M.J. Casavant, X.C. Qin, C.B. Hu, P.J. Boul, L.M. Ericson, et al., In-plane-aligned membranes of carbon nanotubes, Chem. Phys. Lett. 338 (2001) 14–20.
[50] J.E. Fischer, W. Zhou, J. Vavro, M.C. Llaguno, C. Guthy, R. Haggenmueller, et al., Magnetically aligned single wall carbon nanotube films: Preferred orientation and anisotropic transport properties, J. Appl. Phys. 93 (2003) 2157–63. doi:10.1063/1.1536733.
[51] Y. Tian, J.G. Park, Q. Cheng, Z. Liang, C. Zhang, B. Wang, The fabrication of single-walled carbon nanotube/polyelectrolyte multilayer composites by layer-by-layer assembly and magnetic field assisted alignment, Nanotechnology. 20 (2009) 335601. doi:10.1088/0957-4484/20/33/335601.
[52] S. Kumar, H. Kaur, H. Kaur, I. Kaur, K. Dharamvir, L.M. Bharadwaj, Magnetic field-guided orientation of carbon nanotubes through their conjugation with magnetic nanoparticles, J. Mater. Sci. 47 (2011) 1489–1496. doi:10.1007/s10853-011-5934-5.
[53] M.A. Correa-Duarte, M. Grzelczak, V. Salgueiriño-Maceira, M. Giersig, L.M. Liz-Marzan, M. Farle, et al., Alignment of carbon nanotubes under low magnetic fields through attachment of magnetic nanoparticles., J. Phys. Chem. B. 109 (2005) 19060–3. doi:10.1021/jp0544890.
[54] K. Kordás, T. Mustonen, G. Tóth, J. Vähäkangas, A. Uusimäki, H. Jantunen, et al., Magnetic-Field Induced Efficient Alignment of Carbon Nanotubes in Aqueous Solutions, Chem. Mater. 19 (2007) 787–791.
[55] G. Korneva, H. Ye, Y. Gogotsi, D. Halverson, G. Friedman, J.-C. Bradley, et al., Carbon nanotubes loaded with magnetic particles, Nano Lett. 5 (2005) 879–84. doi:10.1021/nl0502928.
[56] C. Park, J. Wilkinson, S. Banda, Z. Ounaies, K.E. Wise, G. Sauti, et al., Aligned single-wall carbon nanotube polymer composites using an electric field, J. Polym. Sci. Part B Polym. Phys. 44 (2006) 1751–62. doi:10.1002/polb.20823.
[57] R.-P. Zhang, Y.-F. Zhu, C. Ma, J. Liang, Alignment of carbon nanotubes in poly(methyl methacrylate) composites induced by electric field, J. Nanosci. Nanotechnol. 9 (2009) 2887–93. http://www.ncbi.nlm.nih.gov/pubmed/19452945.
[58] K. Yamamoto, S. Akita, Y. Nakayama, Orientation and purification of carbon nanotubes using ac electrophoresis, J. Phys. D. Appl. Phys. 31 (1998) L34–L36. doi:10.1088/0022-3727/31/8/002.
[59] A.I. Oliva-Avilés, F. Avilés, V. Sosa, A.I. Oliva, F. Gamboa, Dynamics of carbon nanotube alignment by electric fields, Nanotechnology. 23 (2012) 465710. doi:10.1088/0957-4484/23/46/465710.
[60] M.S. Kumar, T.H. Kim, S.H. Lee, S.M. Song, J.W. Yang, K.S. Nahm, et al., Influence of electric field type on the assembly of single walled carbon nanotubes, Chem. Phys. Lett. 383 (2004) 235–9. doi:10.1016/j.cplett.2003.11.032.
[61] C.A. Martin, J.K.W. Sandler, A.H. Windle, M.-K.K. Schwarz, W. Bauhofer, K. Schulte, et al., Electric field-induced aligned multi-wall carbon nanotube networks in epoxy composites, Polymer (Guildf). 46 (2005) 877–86. doi:10.1016/j.polymer.2004.11.081.
[62] W.A. Chapkin, D.Q. McNerny, M.F. Aldridge, Y. He, W. Wang, J. Kieffer, et al., Real-time assessment of carbon nanotube alignment in a polymer matrix under an applied

electric field via polarized Raman spectroscopy, Polym. Test. 56 (2016) 29–35. doi:10.1016/j.polymertesting.2016.09.018.
[63] M. Kenny, M. Monti, M. Natali, L. Torre, J.M. Kenny, The alignment of single walled carbon nanotubes in an epoxy resin by applying a DC electric field, Carbon N. Y. 50 (2012) 2453–2464. doi:10.1016/j.carbon.2012.01.067.
[64] P. Stamenov, J.M.D. Coey, Magnetic susceptibility of carbon—Experiment and theory, J. Magn. Magn. Mater. 290–291 (2005) 279–285. doi:10.1016/j.jmmm.2004.11.209.
[65] M.F. Islam, D.E. Milkie, C.L. Kane, A.G. Yodh, J.M. Kikkawa, Direct Measurement of the Polarized Optical Absorption Cross Section of Single-Wall Carbon Nanotubes, Phys. Rev. Lett. 93 (2004) 37404. doi:10.1103/PhysRevLett.93.037404.
[66] Y.-F. Zhu, C. Ma, W. Zhang, R.-P. Zhang, N. Koratkar, J. Liang, Alignment of multiwalled carbon nanotubes in bulk epoxy composites via electric field, J. Appl. Phys. 105 (2009) 54319. doi:10.1063/1.3080243.
[67] A.I. Oliva-Avilés, F. Avilés, V. Sosa, G.D. Seidel, Dielectrophoretic modeling of the dynamic carbon nanotube network formation in viscous media under alternating current electric fields, Carbon N. Y. 69 (2014) 342–54. doi:10.1016/j.carbon.2013.12.035.
[68] C.T. O'Konski, K. Yoshioka, W.H. Orttung, Electric Properties of Macromolecules. IV. Determination of Electric and Optical Parameters from Saturation of Electric Birefringence in Solutions, J. Phys. Chem. 63 (1959) 1558–1565. doi:10.1021/j150580a004.
[69] B.H. Fishbine, Carbon Nanotube Alignment and Manipulation Using Electrostatic Fields, Fuller. Sci. Technol. 4 (1996) 87–100. doi:10.1080/10641229608001539.
[70] E. Joselevich, C.M. Lieber, Vectorial Growth of Metallic and Semiconducting Single-Wall Carbon Nanotubes, Nano Lett. 2 (2002) 1137–1141. doi:10.1021/nl025642u.
[71] A.A. Farajian, O. V Pupysheva, H.K. Schmidt, B.I. Yakobson, Polarization, energetics, and electrorheology in carbon nanotube suspensions under an applied electric field: An exact numerical approach, Phys. Rev. B. 77 (2008) 205432. doi:10.1103/PhysRevB.77.205432.
[72] M. Shao-Jie, G. Wan-Lin, Mechanism of Carbon Nanotubes Aligning along Applied Electric Field, Chinese Phys. Lett. 25 (2008) 270–273. doi:10.1088/0256-307X/25/1/073.
[73] J.M. Hilding, M.P.L. Hong, E.A. Grulke, Alignment of dispersed multiwalled carbon nanotubes in low strength AC electrical fields., J. Nanosci. Nanotechnol. 5 (2005) 742–6. doi:10.1166/jnn.2005.098.
[74] C.A. Martin, J.K.W. Sandler, M.S.P. Shaffer, M.-K. Schwarz, W. Bauhofer, K. Schulte, et al., Formation of percolating networks in multi-wall carbon-nanotube–epoxy composites, Compos. Sci. Technol. 37 (2004) 9048–9055. doi:10.1016/j.eurpolymj.2006.12.015.
[75] K.J. Donovan, K. Scott, Transient electric birefringence in suspensions of single-walled carbon nanotubes, Phys. Rev. B. 72 (2005) 195432. doi:10.1103/PhysRevB.72.195432.
[76] T.J. Robb-Smith, K.J. Donovan, K. Scott, M. Somerton, Induced electro-optic effects in single-walled carbon nanotubes. I. Polarizability of metallic nanotubes, Phys. Rev. B. 83 (2011) 155414. doi:10.1103/PhysRevB.83.155414.
[77] N. Ishigami, H. Ago, K. Imamoto, M. Tsuji, K. Iakoubovskii, N. Minami, Crystal plane dependent growth of aligned single-walled carbon nanotubes on sapphire, J. Am. Chem. Soc. 130 (2008) 9918–9924. doi:10.1021/ja8024752.
[78] Q. Wang, J. Dai, W. Li, Z. Wei, J. Jiang, The effects of CNT alignment on electrical conductivity and mechanical properties of SWNT/epoxy nanocomposites, Compos. Sci.

Technol. 68 (2008) 1644–1648. doi:10.1016/j.compscitech.2008.02.024.
[79] M.D. Lynch, D.L. Patrick, Organizing Carbon Nanotubes with Liquid Crystals, Nano Lett. 2 (2002) 1197–1201. doi:10.1021/nl025694j.
[80] M.J. Cadena, R. Misiego, K.C. Smith, A. Avila, B. Pipes, R. Reifenberger, et al., Sub-surface imaging of carbon nanotube – polymer composites using dynamic AFM methods, Nanotechnology. 24 (2013) 135706. doi:10.1088/0957-4484/24/13/135706.
[81] B.W. Smith, D.E. Luzzi, Electron irradiation effects in single wall carbon nanotubes, J. Appl. Phys. 90 (2001) 3509–3515. doi:10.1063/1.1383020.
[82] F. Banhart, Irradiation effects in carbon nanostructures, Reports Prog. Phys. 62 (1999) 1181–1221. doi:10.1088/0034-4885/62/8/201.
[83] C. Mikó, M. Milas, J.W. Seo, E. Couteau, N. Barišić, R. Gaál, et al., Effect of electron irradiation on the electrical properties of fibers of aligned single-walled carbon nanotubes, Appl. Phys. Lett. 83 (2003) 4622. doi:10.1063/1.1631060.
[84] B. Peng, M. Locascio, P. Zapol, S. Li, S.L. Mielke, G.C. Schatz, et al., Measurements of near-ultimate strength for multiwalled carbon nanotubes and irradiation-induced crosslinking improvements., Nat. Nanotechnol. 3 (2008) 626–31. doi:10.1038/nnano.2008.211.
[85] A. Kis, G. Csányi, J.-P. Salvetat, T.-N. Lee, E. Couteau, A.J. Kulik, et al., Reinforcement of single-walled carbon nanotube bundles by intertube bridging., Nat. Mater. 3 (2004) 153–7. doi:10.1038/nmat1076.
[86] P.M.F.J. Costa, P.J. Ferreira, Advanced Transmission Electron Microscopy: Applications to Nanomaterials, Springer International Publishing Switzerland, Cham, 2015. doi:10.1007/978-3-319-15177-9.
[87] A.Y. Feldman, B. Larin, N. Berestetsky, G. Marom, A. Weinberg, Microbeam WAXD Study of Orientated Crystalline Arrays in Carbon Fiber/CNT - Nylon 66 Extruded/drawn Composites, J. Macromol. Sci. Part B Phys. 46 (2007) 111–117. doi:10.1080/00222340601044243.
[88] X. Wang, S.Y. Park, K.H. Yoon, W.S. Lyoo, B.G. Min, The Effect of Multi-walled Carbon Nanotubes on the Molecular Orientation of Poly(vinyl alcohol) in Drawn Composite Films, Fibers Polym. 7 (2006) 323–327.
[89] Y. Miyata, K. Yanagi, Y. Maniwa, T. Tanaka, H. Kataura, Diameter Analysis of Rebundled Single-Wall Carbon Nanotubes Using X-ray Diffraction: Verification of Chirality Assignment Based on Optical Spectra, J. Phys. Chem. C. 112 (2008) 15997–16001.
[90] J. Lefebvre, P. Finnie, Polarized photoluminescence excitation spectroscopy of single-walled carbon nanotubes, Phys. Rev. Lett. 98 (2007) 167406. doi:10.1103/PhysRevLett.98.167406.
[91] M.J. O'Connell, S.M. Bachilo, C.B. Huffman, V.C. Moore, M.S. Strano, E.H. Haroz, et al., Band gap fluorescence from individual single-walled carbon nanotubes., Science. 297 (2002) 593–6. doi:10.1126/science.1072631.
[92] P. Tan, A. Rozhin, T. Hasan, P. Hu, V. Scardaci, W. Milne, et al., Photoluminescence Spectroscopy of Carbon Nanotube Bundles: Evidence for Exciton Energy Transfer, Phys. Rev. Lett. 99 (2007) 137402. doi:10.1103/PhysRevLett.99.137402.
[93] T. Hasan, Z. Sun, F. Wang, F. Bonaccorso, P.H. Tan, A.G. Rozhin, et al., Nanotube–Polymer Composites for Ultrafast Photonics, Adv. Mater. 21 (2009) 3874–3899. doi:10.1002/adma.200901122.

[94] S.M. Bachilo, M.S. Strano, C. Kittrell, R.H. Hauge, R.E. Smalley, R.B. Weisman, Structure-assigned optical spectra of single-walled carbon nanotubes., Science. 298 (2002) 2361–6. doi:10.1126/science.1078727.
[95] S. Lebedkin, F. Hennrich, T. Skipa, M.M. Kappes, Near-Infrared Photoluminescence of Single-Walled Carbon Nanotubes Prepared by the Laser Vaporization Method, J. Phys. Chem. B. 107 (2003) 1949–1956.
[96] G. Dukovic, B.E. White, Z. Zhou, F. Wang, S. Jockusch, M.L. Steigerwald, et al., Reversible surface oxidation and efficient luminescence quenching in semiconductor single-wall carbon nanotubes, J. Am. Chem. Soc. 126 (2004) 15269–15276. doi:10.1021/ja046526r.
[97] M.S. Dresselhaus, G. Dresselhaus, P.C. Eklund, Science of Fullerenes and Carbon Nanotubes, Academic Press, Inc., New York, 1996.
[98] J.A. Fagan, V. Bajpai, B.J. Bauer, E.K. Hobbie, Anisotropic polarizability of isolated semiconducting single-wall carbon nanotubes in alternating electric fields, Appl. Phys. Lett. 91 (2007) 213105. doi:10.1063/1.2807850.
[99] R. Pérez, S. Banda, Z. Ounaies, Determination of the orientation distribution function in aligned single wall nanotube polymer nanocomposites by polarized Raman spectroscopy, J. Appl. Phys. 103 (2008) 74302. doi:10.1063/1.2885347.
[100] M.S. Dresselhaus, G. Dresselhaus, A. Jorio, A.G.S. Filho, R. Saito, Raman spectroscopy on isolated single wall carbon nanotubes, Carbon N. Y. 40 (2002) 2043–61.
[101] C.L. Pint, Y.-Q. Xu, S. Moghazy, T. Cherukuri, N.T. Alvarez, E.H. Haroz, et al., Dry Contact Transfer Printing of Aligned Carbon Nanotube Patterns and, ACS Nano. 4 (2010) 1131–1145.
[102] A. Mashal, D. Wieboldt, K. Jinkins, M.S. Arnold, Polarized Raman Spectroscopy of Aligned Semiconducting Single-Walled Carbon Nanotubes, Spectroscopy. 31 (2016) 36–44.
[103] H.G.G. Chae, M.L. Minus, S. Kumar, Oriented and exfoliated single wall carbon nanotubes in polyacrylonitrile, Polymer (Guildf). 47 (2006) 3494–3504. doi:10.1016/j.polymer.2006.03.050.
[104] A. Swan, Measurement Issues in Single Wall Carbon Nanotubes, 2008. doi:682901795.
[105] W.A. Chapkin, A.I. Taub, Determining the controlling mechanism of electrostatically induced carbon nanotube rotation using in situ, real-time polarized Raman spectroscopy, in: Proc Amer Soc Comp 31st Tech Conf, 2016: pp. 1–11.
[106] T.J. Robb-Smith, K.J. Donovan, K. Scott, M. Somerton, Induced electro-optic effects in single-walled carbon nanotubes. II. Hydrodynamics of nanotubes in viscous media, Phys. Rev. B. 83 (2011) 155415. doi:10.1103/PhysRevB.83.155415.
[107] E.C. Sengezer, G.D. Seidel, Phenomenological Characterization of the Fabrication of Aligned Carbon Nanotube Nanocomposites via Dielectrophoresis Under AC Electric Field, in: AIAA/ASMC/ASCE/AIIS/ASC Struct. Struct. Dyn. Mater. Conf., 2013: pp. 1–12.
[108] M.F. Aldridge, In Situ Light Scattering Analysis of the Curing Behavior and the Mechanical Properties of Thermoset Polymers, University of Michigan, 2014. https://deepblue.lib.umich.edu/handle/2027.42/108929.
[109] J.P.F. Lagerwall, G. Scalia, M. Haluska, U. Dettlaff-weglikowska, F. Giesselmann, S. Roth, Simultaneous alignment and dispersion of carbon nanotubes with lyotropic liquid crystals, Phys. Status Solidi. 243 (2006) 3046–3049. doi:10.1002/pssb.200669146.

[110] B.W. Steinert, D.R. Dean, Magnetic field alignment and electrical properties of solution cast PET – carbon nanotube composite films, Polymer (Guildf). 50 (2009) 898–904. doi:10.1016/j.polymer.2008.11.053.
[111] A. Jorio, G. Dresselhaus, M.S. Dresselhaus, Polarized Raman Study of Single-Wall Semiconducting Carbon Nanotubes, Phys. Rev. Lett. 85 (2000) 2617–2620.
[112] H.H. Gommans, J.W. Alldredge, H. Tashiro, J. Park, J. Magnuson, A.G. Rinzler, Fibers of aligned single-walled carbon nanotubes: Polarized Raman spectroscopy, J. Appl. Phys. 88 (2000) 2509–2514. doi:10.1063/1.1287128.
[113] A.N.G. Parra-Vasquez, Solubility, Length Characterization, and Cryo-TEM of Pristine and Functionalized Single-Walled Carbon Nanotubes in Surfactant and Superacid Systems, With Application to Spinning SWNT Fibers, Rice University, 2009. https://scholarship.rice.edu/handle/1911/62052.
[114] W. Zhou, J. Vavro, C. Guthy, K.I. Winey, J.E. Fischer, L.M. Ericson, et al., Single wall carbon nanotube fibers extruded from super-acid suspensions: Preferred orientation, electrical, and thermal transport, J. Appl. Phys. 95 (2004) 649–655. doi:10.1063/1.1627457.
[115] L.M. Ericson, Macroscopic Neat Single-Wall Carbon Nanotube Fibers, Rice University, 2003. https://scholarship.rice.edu/handle/1911/18626.
[116] G. Duesberg, I. Loa, M. Burghard, K. Syassen, S. Roth, Polarized Raman Spectroscopy on Isolated Single-Wall Carbon Nanotubes, Phys. Rev. Lett. 85 (2000) 5436–5439. doi:10.1103/PhysRevLett.85.5436.
[117] X. Li, L. Zhang, X. Wang, I. Shimoyama, X. Sun, W.K. Seo, et al., Langmuir-Blodgett assembly of densely aligned single-walled carbon nanotubes from bulk materials, J. Am. Chem. Soc. 129 (2007) 4890–4891. doi:10.1021/ja071114e.
[118] Q. Cao, S. Han, G.S. Tulevski, Y. Zhu, D.D. Lu, W. Haensch, Arrays of single-walled carbon nanotubes with full surface coverage for high-performance electronics., Nat. Nanotechnol. 8 (2013) 180–6. doi:10.1038/nnano.2012.257.
[119] Y. Joo, G.J. Brady, M.S. Arnold, P. Gopalan, Dose-controlled, floating evaporative self-Assembly and alignment of semiconducting carbon nanotubes from organic solvents, Langmuir. 30 (2014) 3460–3466. doi:10.1021/la500162x.
[120] J. Hwang, H.H. Gommans, A. Ugawa, H. Tashiro, R. Haggenmueller, K.I. Winey, et al., Polarized spectroscopy of aligned single-walled carbon nanotubes, Phys. Rev. B. 62 (2000) R13310–R13313.
[121] T. Liu, S. Kumar, Quantitative characterization of SWNT orientation by polarized Raman spectroscopy, Chem. Phys. Lett. 378 (2003) 257–262. doi:10.1016/S0009-2614(03)01287-9.
[122] T. V. Sreekumar, T. Liu, B.G. Min, H. Guo, S. Kumar, R.H. Hauge, et al., Polyacrylonitrile Single-Walled Carbon Nanotube Composite Fibers, Adv. Mater. 16 (2004) 58–61. doi:10.1002/adma.200305456.
[123] T. Liu, S. Kumar, Effect of Orientation on the Modulus of SWNT Films and Fibers, Nano Lett. 3 (2003) 647–650. doi:10.1021/nl034071i.
[124] A.N.G. Parra-Vasquez, I. Stepanek, V.A. Davis, V.C. Moore, E.H. Haroz, J. Shaver, et al., Simple length determination of single-walled carbon nanotubes by viscosity measurements in dilute suspensions, Macromolecules. 40 (2007) 4043–4047. doi:10.1021/ma062003n.
[125] A.N.G. Parra-Vasquez, J.G. Duque, M.J. Green, M. Pasquali, Assessment of Length and

Bundle Distribution of Dilute Single-Walled Carbon Nanotubes by Viscosity Measurements, AIChE J. 60 (2014) 1499–1508. doi:10.1002/aic.
[126] P.G. de Gennes, Motions of one stiff molecule in an entangled polymer melt, J. Phys. 42 (1981) 473–477. doi:10.1051/jphys:01981004203047300.
[127] F. Brochard Wyart, P.G. de Gennes, Viscosity at small scales in polymer melts, Eur. Phys. J. E. 1 (2000) 93–7.
[128] A. Tuteja, M.E. Mackay, S. Narayanan, S. Asokan, M.S. Wong, Breakdown of the continuum Stokes-Einstein relation for nanoparticle diffusion, Nano Lett. 7 (2007) 1276–81. doi:10.1021/nl070192x.
[129] C.A. Grabowski, A. Mukhopadhyay, Size Effect of Nanoparticle Diffusion in a Polymer Melt, Macromolecules. 47 (2014) 7238–42.
[130] C.A. Grabowski, B. Adhikary, A. Mukhopadhyay, Dynamics of gold nanoparticles in a polymer melt, Appl. Phys. Lett. 94 (2009) 21903. doi:10.1063/1.3070533.
[131] U. Yamamoto, K.S. Schweizer, Microscopic Theory of the Long-Time Diffusivity and Intermediate-Time Anomalous Transport of a Nanoparticle in Polymer Melts, Macromolecules. 48 (2015) 152–163. doi:10.1021/ma501150q.
[132] J.T. Kalathi, U. Yamamoto, K.S. Schweizer, G.S. Grest, S.K. Kumar, Nanoparticle Diffusion in Polymer Nanocomposites, Phys. Rev. Lett. 112 (2014) 108301. doi:10.1103/PhysRevLett.112.108301.
[133] U. Yamamoto, K.S. Schweizer, Spatially dependent relative diffusion of nanoparticles in polymer melts, J. Chem. Phys. 139 (2013) 64907. doi:10.1063/1.4817593.
[134] J. Choi, M. Cargnello, C.B. Murray, N. Clarke, K.I. Winey, R.J. Composto, Fast Nanorod Diffusion through Entangled Polymer Melts, ACS Macro Lett. 4 (2015) 952–6. doi:10.1021/acsmacrolett.5b00348.
[135] U. Yamamoto, K.S. Schweizer, Theory of nanoparticle diffusion in unentangled and entangled polymer melts, J. Chem. Phys. 135 (2011) 0–16. doi:10.1063/1.3664863.
[136] R.A. Omari, A.M. Aneese, C.A. Grabowski, A. Mukhopadhyay, Diffusion of nanoparticles in semidilute and entangled polymer solutions, J. Phys. Chem. B. 113 (2009) 8449–52. doi:10.1021/jp9035088.
[137] N. Fakhri, D.A. Tsyboulski, L. Cognet, R.B. Weisman, M. Pasquali, Diameter-dependent bending dynamics of single-walled carbon nanotubes in liquids, in: Proc Natl Acad Sci USA, 2009: pp. 14219–14223.
[138] J.M. Tsay, S. Doose, S. Weiss, Rotational and Translational Diffusion of Peptide-coated CdSe/CdS/ZnS Nanorods Studied by Fluorescence Correlation Spectroscopy, Laser Phys. 128 (2006) 1639–47. doi:10.1021/ja056162i.Rotational.
[139] R. Cush, D. Dorman, P.S. Russo, Rotational and Translational Diffusion of Tobacco Mosaic Virus in Extended and Globular Polymer Solutions, Macromolecules. 37 (2004) 9577–84. doi:10.1021/ma0490294.
[140] Hexion, EPON™ Resin 828 Technical Data Bulletin, 2005.
[141] G.S. Fulcher, Analysis of recent measurements of the viscosity of glasses, J. Am. Ceram. Soc. 8 (1925) 789–794. doi:10.1111/j.1151-2916.1925.tb16731.x.
[142] S. Broersma, Rotational Diffusion Constant of a Cylindrical Particle, J. Chem. Phys. 32 (1960) 1626–1631. doi:10.1063/1.1730994.
[143] E. Wachenfeld-Eisele, W. Burchard, Biological and Synthetic Polymer Networks, Elsevier Applied Science, New York, 1988.
[144] S. Alam, A. Mukhopadhyay, Translational and Rotational Diffusions of Nanorods within

Semidilute and Entangled Polymer Solutions, Macromolecules. 47 (2014) 6919–6924. doi:10.1021/ma5014995.
[145] S.U. Khan, J.R. Pothnis, J. Kim, Effects of carbon nanotube alignment on electrical and mechanical properties of epoxy nanocomposites, Compos. Part A. 49 (2013) 26–34.
[146] C. Ma, H.-Y. Liu, X. Du, L. Mach, F. Xu, Y.-W. Mai, Fracture resistance, thermal and electrical properties of epoxy composites containing aligned carbon nanotubes by low magnetic field, Compos. Sci. Technol. 114 (2015) 126–135. doi:10.1016/j.compscitech.2015.04.007.
[147] M. Mandel, The electric polarization of rod-like, charged macromolecules, Mol. Phys. 4 (1961) 489–496. doi:10.1080/00268976100100651.
[148] J.A. Altig, G.E. Wesenberg, W.E. Vaughan, Dielectric behavior of polyelectrolytes IV. Electric polarizability of rigid biopolymers in electric fields, Biophys. Chem. 24 (1986) 221–234.
[149] Y. Zhang, A. Chang, J. Cao, Q. Wang, W. Kim, Y. Li, et al., Electric-field-directed growth of aligned single-walled carbon nanotubes, Appl. Phys. Lett. 79 (2001) 3155. doi:10.1063/1.1415412.
[150] A.I. Oliva-Avilés, F. Avilés, V. Sosa, Electrical and piezoresistive properties of multi-walled carbon nanotube/polymer composite films aligned by an electric field, Carbon N. Y. 49 (2011) 2989–2997. doi:10.1016/j.carbon.2011.03.017.
[151] F. Hennrich, R. Krupke, K. Arnold, J.A.R. Stütz, S. Lebedkin, T. Koch, et al., The mechanism of cavitation-induced scission of single-walled carbon nanotubes, J. Phys. Chem. B. 111 (2007) 1932–1937. doi:10.1021/jp065262n.
[152] A. Lucas, M. Maugey, M. Pasquali, P. Van Der Schoot, P. Poulin, Kinetics of Nanotube and Microfiber Scission under Sonication, J. Phys. Chem. C. 113 (2009) 20599–20605.
[153] J.P. Casey, S.M. Bachilo, C.H. Moran, R.B. Weisman, S.C.N. Samples, J.P. Casey, et al., Chirality-Resolved Length Analysis of Single-Walled Carbon Nanotube Samples through Shear-Aligned Photoluminescence Anisotropy, ACS Nano. 2 (2008) 1738–1746.
[154] G. Pagani, M.J. Green, P. Poulin, M. Pasquali, Competing mechanisms and scaling laws for carbon nanotube scission by ultrasonication, in: Proc. Natl. Acad. Sci. U. S. A., 2012: pp. 11599–11604. doi:10.1073/pnas.
[155] B. Koh, W.E.I. Cheng, The Impact of Sonication on the Surface Quality of Single-Walled, Pharm. Nanotechnol. 104 (2015) 2594–2599. doi:10.1002/jps.24483.
[156] T.J. Simmons, J. Bult, D.P. Hashim, R.J. Linhardt, P.M. Ajayan, Noncovalent Functionalization as an Alternative to Oxidative Acid Treatment of Single Wall Carbon Nanotubes with Applications for Polymer Composites, ACS Nano. 3 (2009) 865–870.
[157] M.S. Brown, J.W. Shan, C. Lin, F.M. Zimmermann, Electrical polarizability of carbon nanotubes in liquid suspension, Appl. Phys. Lett. 90 (2007) 203108. doi:10.1063/1.2740186.
[158] M.F.L. De Volder, S.H. Tawfick, R.H. Baughman, A.J. Hart, M.F.L. De Volder, S.H. Tawfick, et al., Carbon nanotubes: present and future commercial applications., Science. 339 (2013) 535–9. doi:10.1126/science.1222453.
[159] Q. Zhang, J.Q. Huang, W.Z. Qian, Y.Y. Zhang, F. Wei, The road for nanomaterials industry: A review of carbon nanotube production, post-treatment, and bulk applications for composites and energy storage, Small. 9 (2013) 1237–1265. doi:10.1002/smll.201203252.
[160] N. De Greef, L. Gorbatikh, A. Godara, L. Mezzo, S. V. Lomov, I. Verpoest, The effect of

carbon nanotubes on the damage development in carbon fiber/epoxy composites, Carbon N. Y. 49 (2011) 4650–4664. doi:10.1016/j.carbon.2011.06.047.
[161] H.W. Zhou, L. Mishnaevsky, H.Y. Yi, Y.Q. Liu, X. Hu, A. Warrier, et al., Carbon fiber/carbon nanotube reinforced hierarchical composites: Effect of CNT distribution on shearing strength, Compos. Part B Eng. 88 (2016) 201–211. doi:10.1016/j.compositesb.2015.10.035.
[162] A. Godara, L. Mezzo, F. Luizi, A. Warrier, S. V. Lomov, A.W. van Vuure, et al., Influence of carbon nanotube reinforcement on the processing and the mechanical behaviour of carbon fiber/epoxy composites, Carbon N. Y. 47 (2009) 2914–2923. doi:10.1016/j.carbon.2009.06.039.
[163] E. Bekyarova, E.T. Thostenson, A. Yu, H. Kim, J. Gao, J. Tang, et al., Multiscale carbon nanotube-carbon fiber reinforcement for advanced epoxy composites., Langmuir. 23 (2007) 3970–4. doi:10.1021/la062743p.
[164] D.C. Davis, J.W. Wilkerson, J. Zhu, D.O.O.O. Ayewah, Improvements in mechanical properties of a carbon fiber epoxy composite using nanotube science and technology, Compos. Struct. 92 (2010) 2653–2662. doi:10.1016/j.compstruct.2010.03.019.
[165] J. Zhu, A. Imam, R. Crane, K. Lozano, V.N. Khabashesku, E. V. Barrera, Processing a glass fiber reinforced vinyl ester composite with nanotube enhancement of interlaminar shear strength, Compos. Sci. Technol. 67 (2007) 1509–1517. doi:10.1016/j.compscitech.2006.07.018.
[166] Z. Fan, M.H. Santare, S.G. Advani, Interlaminar shear strength of glass fiber reinforced epoxy composites enhanced with multi-walled carbon nanotubes, Compos. Part A Appl. Sci. Manuf. 39 (2008) 540–554. doi:10.1016/j.compositesa.2007.11.013.
[167] L. Musinski, Investigation of a micro-and nano-particle in-space electrostatic propulsion concept, University of Michigan, 2009. https://deepblue.lib.umich.edu/handle/2027.42/62433u/bitstream/handle/2.
[168] W.A. Chapkin, J.K. Wenderott, A.I. Taub, Electrostatically induced alignment of discrete carbon nanotube populations based on nanotube length, (2017) Manuscript in Preparation.
[169] F.T. Ulaby, Fundamentals of Applied Electromagnetics, 5th ed., Pearson Education, Inc., Upper Saddle River, NJ, 2007.
[170] J.-E. Kim, C.-S. Han, Use of dielectrophoresis in the fabrication of an atomic force microscope tip with a carbon nanotube: a numerical analysis, Nanotechnology. 16 (2005) 2245–50. doi:10.1088/0957-4484/16/10/046.
[171] D. Padmaraj, W. Zagozdzon-Wosik, L.-M. Xie, V.G. Hadjiev, P. Cherukuri, J. Wosik, Parallel and orthogonal E-field alignment of single-walled carbon nanotubes by AC dielectrophoresis, Nanotechnology. 20 (2009) 35201. doi:10.1088/0957-4484/20/3/035201.
[172] S. Wu, R.B. Ladani, J. Zhang, E. Bafekrpour, K. Ghorbani, A.P. Mouritz, et al., Aligning multilayer graphene flakes with an external electric field to improve multifunctional properties of epoxy nanocomposites, Carbon N. Y. 94 (2015) 607–618. doi:10.1016/j.carbon.2015.07.026.
[173] E.J. Garcia, B.L. Wardle, A. John Hart, N. Yamamoto, Fabrication and multifunctional properties of a hybrid laminate with aligned carbon nanotubes grown In Situ, Compos. Sci. Technol. 68 (2008) 2034–2041. doi:10.1016/j.compscitech.2008.02.028.
[174] S.S. Wicks, R.G. de Villoria, B.L. Wardle, Interlaminar and intralaminar reinforcement of composite laminates with aligned carbon nanotubes, Compos. Sci. Technol. 70 (2010) 20–

28. doi:10.1016/j.compscitech.2009.09.001.
[175] I. Balberg, C.H. Anderson, S. Alexander, N. Wagner, Excluded volume and its realtion to the onset of percolation, Phsical Rev. B. 30 (1984) 3933–3943. doi:10.1103/PhysRevB.30.3933.
[176] W. Bauhofer, J.Z. Kovacs, T. Swan, T. Swan, T. Swan, A review and analysis of electrical percolation in carbon nanotube polymer composites, Compos. Sci. Technol. 69 (2009) 1486–1498. doi:10.1016/j.compscitech.2008.06.018.
[177] C.A. Martin, J.K.W. Sandler, M.S.P. Shaffer, M.K. Schwarz, W. Bauhofer, K. Schulte, et al., Formation of percolating networks in multi-wall carbon-nanotube-epoxy composites, Compos. Sci. Technol. 64 (2004) 2309–2316. doi:10.1016/j.compscitech.2004.01.025.
[178] L.S. Schadler, S.C. Giannaris, P.M. Ajayan, Load transfer in carbon nanotube epoxy composites, Appl. Phys. Lett. 73 (1998) 3842–3844.
[179] M.D. Frogley, Q. Zhao, H.D. Wagner, Polarized resonance Raman spectroscopy of single-wall carbon nanotubes within a polymer under strain, Phys. Rev. B. 65 (2002) 113413. doi:10.1103/PhysRevB.65.113413.
[180] S. Cui, I.A. Kinloch, R.J. Young, L. Noé, M. Monthioux, The Effect of Stress Transfer Within Double-Walled Carbon Nanotubes Upon Their Ability to Reinforce Composites, Adv. Mater. 21 (2009) 3591–3595. doi:10.1002/adma.200803683.
[181] P. Ma, Q. Zheng, E. Mäder, J. Kim, Behavior of load transfer in functionalized carbon nanotube / epoxy nanocomposites, Polymer (Guildf). 53 (2012) 6081–6088. doi:10.1016/j.polymer.2012.10.053.
[182] R.J. Young, L. Deng, T.Z. Wafy, I.A. Kinloch, Interfacial and internal stress transfer in carbon nanotube based nanocomposites, J. Mater. Sci. 51 (2016) 344–352. doi:10.1007/s10853-015-9347-8.
[183] S. Alam, A. Mukhopadhyay, Translational Anisotropy and Rotational Diffusion of Gold Nanorods in Colloidal Sphere Solutions, Langmuir. 31 (2015) 8780–8785. doi:10.1021/acs.langmuir.5b01682.
[184] E. Richter, K. Subbaswamy, Theory of Size-Dependent Resonance Raman Scattering from Carbon Nanotubes, Phys. Rev. Lett. 79 (1997) 2738–2741. doi:10.1103/PhysRevLett.79.2738.
[185] H. Kataura, Y. Kumazawa, Y. Maniwa, I. Umezu, S. Suzuki, Y. Ohtsuka, et al., Optical Properties of Single-Wall Carbon Nanotubes, Synth. Met. 103 (1999) 2555–2558.
[186] A.M. Rao, E. Richter, S. Bandow, B. Chase, P.C. Eklund, K.A. Williams, et al., Diameter-Selective Raman Scattering from Vibrational Modes in Carbon Nanotubes, Science (80-.). 275 (1997) 187–191.
[187] M.A. Pimenta, A. Marucci, S.D.M. Brown, M.J. Matthews, A.M. Rao, P.C. Eklund, et al., Resonant Raman effect in single-wall carbon nanotubes, J. Mater. Res. 13 (1998) 2405–2411. doi:10.1557/JMR.1998.0333.
[188] R. Graupner, Raman spectroscopy of covalently functionalized single-wall carbon nanotubes, J. Raman Spectrosc. 38 (2007) 673–683. doi:10.1002/jrs.
[189] M.S. Dresselhaus, G. Dresselhaus, R. Saito, A. Jorio, Raman spectroscopy of carbon nanotubes, Phys. Rep. 409 (2005) 47–99. doi:10.1016/j.physrep.2004.10.006.
[190] S. Blatt, F. Hennrich, H.V. Löhneysen, M.M. Kappes, A. Vijayaraghavan, R. Krupke, Influence of structural and dielectric anisotropy on the dielectrophoresis of single-walled carbon nanotubes, Nano Lett. 7 (2007) 1–11. doi:10.1021/nl0706751.
[191] NanoIntegris Technical Data Sheet, 2013.

[192] S. Brown, A. Jorio, P. Corio, M.S. Dresselhaus, G. Dresselhaus, R. Saito, et al., Origin of the Breit-Wigner-Fano lineshape of the tangential G-band feature of metallic carbon nanotubes, Phys. Rev. B. 63 (2001) 1–8. doi:10.1103/PhysRevB.63.155414.
[193] H. Liao, H. Zheng, Liquid Cell Transmission Electron Microscopy Study of Platinum Iron, J. Am. Chem. Soc. 135 (2013) 5038–5043. doi:10.1021/ja310612p.
[194] H. Zheng, S.A. Claridge, A.M. Minor, A.P. Alivisatos, U. Dahmen, Nanocrystal diffusion in a liquid thin film observed by in situ transmission electron microscopy, Nano Lett. 9 (2009) 2460–2465. doi:10.1021/nl9012369.
[195] J.M. Grogan, L. Rotkina, H.H. Bau, In situ liquid-cell electron microscopy of colloid aggregation and growth dynamics, Phys. Rev. E - Stat. Nonlinear, Soft Matter Phys. 83 (2011) 1–5. doi:10.1103/PhysRevE.83.061405.
[196] Y. Liu, X.M. Lin, Y. Sun, T. Rajh, In situ visualization of self-assembly of charged gold nanoparticles, J. Am. Chem. Soc. 135 (2013) 3764–3767. doi:10.1021/ja312620e.
[197] M.J. Williamson, R.M. Tromp, P.M. Vereecken, R. Hull, F.M. Ross, Dynamic microscopy of nanoscale cluster growth at the solid-liquid interface., Nat. Mater. 2 (2003) 532–6. doi:10.1038/nmat944.
[198] D.L. Fan, F.Q. Zhu, R.C. Cammarata, C.L. Chien, Controllable high-speed rotation of nanowires, Phys. Rev. Lett. 94 (2005) 247208. doi:10.1103/PhysRevLett.94.247208.
[199] D.L. Fan, R.C. Cammarata, C.L. Chien, Precision transport and assembling of nanowires in suspension by electric fields, Appl. Phys. Lett. 92 (2008) 93115. doi:10.1063/1.2891091.
[200] J.J. Arcenegui, P. García-Sánchez, H. Morgan, A. Ramos, Electric-field-induced rotation of Brownian metal nanowires, Phys. Rev. E. 88 (2013) 33025. doi:10.1103/PhysRevE.88.033025.
[201] K. Chen, N. Xiang, Y. Quan, X. Zhu, D. Sun, H. Yi, et al., Directed transport and location-designated rotation of nanowires using ac electric fields, Microfluid. Nanofluidics. 16 (2014) 237–246. doi:10.1007/s10404-013-1203-z.
[202] N. de Jonge, N. Poirier-Demers, H. Demers, D.B. Peckys, D. Drouin, Nanometer-resolution electron microscopy through micrometers-thick water layers, Ultramicroscopy. 110 (2010) 1114–1119. doi:10.1016/j.ultramic.2010.04.001.
[203] J.M. Grogan, N.M. Schneider, F.M. Ross, H.H. Bau, Bubble and pattern formation in liquid induced by an electron beam, Nano Lett. 14 (2014) 359–364. doi:10.1021/nl404169a.
[204] W. Zhou, M.F. Islam, H. Wang, D.L. Ho, A.G. Yodh, K.I. Winey, et al., Small angle neutron scattering from single-wall carbon nanotube suspensions: Evidence for isolated rigid rods and rod networks, Chem. Phys. Lett. 384 (2004) 185–189. doi:10.1016/j.cplett.2003.11.106.
[205] J.A. Fagan, B.J. Landi, I. Mandelbaum, J.R. Simpson, V. Bajpai, B.J. Bauer, et al., Comparative measures of single-wall carbon nanotube dispersion, J. Phys. Chem. B. 110 (2006) 23801–23805. doi:10.1021/jp0647434.
[206] Y. Huang, S. Ahir, E. Terentjev, Dispersion rheology of carbon nanotubes in a polymer matrix, Phys. Rev. B. 73 (2006) 125422. doi:10.1103/PhysRevB.73.125422.
[207] S.K. Doorn, M.S. Strano, M.J. O'Connell, E.H. Haroz, K.L. Rialon, R.H. Hauge, et al., Capillary Electrophoresis Separations of Bundled and Individual Carbon Nanotubes, J. Phys. Chem. B. 107 (2003) 6063–6069.
[208] D.A. Heller, P.W. Barone, J.P. Swanson, R.M. Mayrhofer, M.S. Strano, Using Raman

Spectroscopy to Elucidate the Aggregation State of Single-Walled Carbon Nanotubes, J. Phys. Chem. B. 108 (2004) 6905–6909. doi:10.1021/jp037690o.
[209] M.J. O'Connell, S. Sivaram, S.K. Doorn, Near-infrared resonance Raman excitation profile studies of single-walled carbon nanotube intertube interactions : A direct comparison of bundled and individually dispersed HiPco nanotubes, Phys. Rev. B. (2004) 235415. doi:10.1103/PhysRevB.69.235415.
[210] S. Badaire, P. Poulin, M. Maugey, C. Zakri, In situ measurements of nanotube dimensions in suspensions by depolarized dynamic light scattering, Langmuir. 20 (2004) 10367–10370. doi:10.1021/la049096r.
[211] A.M. Shetty, G.M.H. Wilkins, J. Nanda, M.J. Solomon, Multiangle Depolarized Dynamic Light Scattering of Short Functionalized Single-Walled Carbon Nanotubes, J. Phys. Chem. C. 113 (2009) 7129–7133. doi:10.1021/jp900731q.